A Planar Hopping Robot with One Actuator:

Design, Simulation, and Experimental Results

Akihiro Sato

Department of Mechanical Engineering,
McGill University, Montreal, Canada

February 2005

A thesis submitted to the Faculty of Graduate Studies and Research
in partial fulfillment of the requirements of the degree of Master of Engineering

Your file Votre référence
ISBN: 0-494-12645-0
Our file Notre référence
ISBN: 0-494-12645-0

Abstract

The complex musculoskeletal system of a running animal on horizontal surfaces act essentially like a simple pogo stick, and can be modeled as a hopping spring-mass model known as the Spring-loaded Inverted Pendulum (SLIP) model. The SLIP model has been extensively used as a reduced-order model in analysis and control of running legged robots. By contrast, the SLIP model itself has never been implemented in a robot and validated experimentally. This thesis addresses the development and validation of a robotic SLIP, a planar one-legged hopping robot with only one actuator. A feasibility study was performed using numerical simulation. The experimental platform was designed and built based on SLIP-model features. A hopping controller that conceptually reproduced the self-stability property of the SLIP model was implemented. Running was achieved at 6.7 leg lengths per second, which is, to date, the fastest dimension-less speed for a single-legged robot. Simulation and experimental data demonstrated periodic and robust stability. The SLIP model was qualitatively validated for a particular gait in simulation and experimentation.

Résumé

Le système musculo-squelettique des animaux pouvant courir sur des surfaces horizontales est comparable à un simple « bâton pogo » et par le fait même peut être modélisé en utilisant un modèle connu sous le nom de « Spring-loaded Inverted Pendulums » (SLIP). Le modèle SLIP est très répandu comme modèle d'ordre réduit pour l'analyse et le contrôle des robots coureurs à pattes. Cependant, le modèle SLIP n'a jamais été implémenté sur un robot ni validé expérimentalement. La problématique couverte par cette thèse concerne le développement d'un SLIP robotique ou plus précisément, d'un robot planaire à une jambe possédant et un seul moteur. Une étude de faisabilité à été effectué en utilisant une simulation numérique. Le design et la construction de la plate-forme expérimentale ont été directement inspirés des caractéristiques du modèle SLIP. Un contrôleur reproduisant conceptuellement la propriété de stabilité intrinsèque au modèle SLIP a été implémentée. Une course d'une vitesse de 6.7 longueur de jambe par seconde a été produite, ce qui est, à ce jour, la plus grande vitesse non-dimensionelle atteinte par un robot à une jambe. La stabilité périodique et robuste du système à été démontrée en simulation et par les données expérimentales Finalement, le modèle SLIP a été validé de façon qualitative pour une marche spécifique en utilisant une simulation et aussi par une démarche expérimentale.

Acknowledgments

I am delighted that I have researched in the Ambulatory Robotics Laboratory, studied at McGill University, and lived in Montreal, which is a combination of the most desirable places. First of all, I thank the people who gave me the opportunity:

- My family: I thank for their understanding and support.
- Prof. Ken Tomiyama, previous supervisor: encouraged my plan to study abroad. His engineering courses using English were not only excellent lectures themselves but also suitable preparation for courses in English at McGill. His recommendation letter for my application was strong.
- Prof. Martin Buehler, supervisor: decided to take me only after I went to his office twice. He gave me a big chance. I thank him for his generous personality. I hope I worked hard enough and returned the favor.

I thank the following people for leading and assisting my research:

- Prof. Martin Buehler: I have been impressed not only by his research capabilities but also by his passion to continue doing research. This stimulated my work. His knowledge and experience in legged robots also gave me a lot. I am really lucky that I have had his supervision and I might be his first and last Japanese student.
- Prof. Meyer Nahon: kindly offered detailed instructions. His acute criticism accelerated the vast improvement in writing quality.
- Ioannis Poulakakis: is another "supervisor" of mine. He mainly helped with the theoretical aspects of dynamical analysis in my research. I thank him for his guidance throughout my studies. He is the guy who can study if there is no exam.
- Neil Neville: proofread Chapters 1 and 5. He is a profound thinker and pointed out flaws in my thoughts, so that I was able to expand my conception in

appropriate directions. His advice helped with the empirical tuning of PD gains and filters.

- James A. Smith: proofread Chapters 2, 4 and 5 critically and carefully and the final version of the IROS 2004 paper. Thanks for the cakes with the nice care to everybody in the lab. He helped with the circuit for an IR sensor.
- Don Campbell: His sense of mechanical dynamics gave me hints for my robot simulation. Impressive that he is an electrical engineer. He designed a level shifter between a D/A interface card and a motor amplifier on my first experimental setup.
- Dave McMordie: provided the info and parts of the end-less potentiometers used on my experimental setup. He is one of the two "MacGyver" persons I know.
- John Sheldon: proofread Chapters 1 and 3 and the first version of the IROS 2004 paper. I was honored to talk about Japan.
- Evgeni Kiriy: proofread Chapters 1 and 3. He is the only perfectionist I ever met.
- Chris Prahacs: proofread Chapter 6. He amazingly keeps up with tight schedules.
- François Deschênes: translated a version of abstract into French. He is my French teacher for bars. He was my partner on the red-flag team.
- Christine Georgiades: Her thrust measuring setup was an informative reference for my setup. She is not afraid to study new fields.
- Francis: got three Acco binders for me. Thanks for his two comments in and after my final presentation.
- Carl Steeves: My servo system is based on his lecture and notes on a motor drive system. I learned that one could become skillful by asking appropriate questions to other people.
- Rene Sutton Pronovost & Chris Owen: developed several prototype platforms with me, which led to the platform presented in this thesis. Discussions with them propelled my work progress.

- Shane Saunderson: edited one of the two videos I used in my final presentation. He proofread Chapter 4. I agree with his opinion about Vegetarian tofu, but I should have served real, raw tofu.
- Seigo Harashima: His help with the driver code for an AD/DA card was a key to complete my experimental platform.
- Yunig Zhang: helped my understanding of mechanical dynamics, especially in impact, friction, and system identification.
- Danny Chouinard & Jan Binder: Thanks for the great computer network administration. I sometimes came across their holiday work.
- Philippe Coulombe-Pontbriand: translated the abstract into French with a clear understanding of contexts.
- Vanessa Cadrin: proofread Chapter 2 and helped editing the style of this thesis.
- Enrico Sabeli: joined the lab at the same time as I did at my first experience of the RHex field run. Youngest in the lab and one of the most skillful.
- Ned Moore: cheered me up a lot with my course work in my first year.
- Matt Smith: helped with my mechanical work in my earlier time when I was on the RHex team.
- Gen Vinois: managed the expense for the project. She gave a merry lab atmosphere.
- Mike Tolley: answered to my English questions on slight nuances so that my writing skill became one more stage higher.
- Julien Marcil: taught me "pronunciation."
- Aaron Saunders: is a popular specimen. His future life is to be observed.
- Cynthia Davidson & Marlene Gray: administrated the CIM.
- Ms. Anna Cianci & Ms. Joyce Nault: handled my program with care.

- Mr. Colin Dean Barnes: kindly continued responding to my repetitive inquiries on the graduation procedure.

It would have taken me decades to achieve my work if none of the below had existed:

- MathWorks, Inc.: Their work provided easy and powerful computation.
- Apple, IBM, and Microsoft: developed "the computer," which provided supreme flexibility in editing, compared to the typewriter, and allowed my "organized" way of writing.
- LONGMAN and Merriam-Webster: Their free online services compensated for my lack of vocabulary.

Table of Contents

List of Figures

List of Tables

Nomenclature

α_{roll}	:	roll angle of the planarizer boom
α_{yaw}	:	yaw angle of the planarizer boom about the rotation axis
b	:	damping coefficient of the prismatic leg joint
D	:	dissipated energy
δ^{Bottom}	:	spring deflection at the bottom
δ_{pre}	:	pre-deflection of the spring
E_{total}	:	total mechanical energy of the SLIP model/robot
F , F_i	:	sum of the applied external forces/torques in the coordinate
$F_1(s)$, $F_2(s)$	:	lowpass filters used on the potentiometer output γ^{pot} to obtain the first and second filtered angles γ^{LP1} and γ^{LP2}, respectively
f_n	:	natural frequency of the spring-mass vibration in the vertical stance dynamics model of the robot or animals
g	:	gravitational acceleration
γ	:	leg angle at the hip with respect to the downward vertical, counterclockwise in simulation, clockwise in experimentation
γ_{com}	:	commanded leg angle
γ_{com}^{Fl}	:	commanded leg angle throughout the flight phase
γ_{com}^{St}	:	commanded leg angle throughout the stance phase
γ^{LO}	:	lift-off leg angle
γ_{des}^{LO}	:	desired lift-off leg angle
γ^{LP1} , γ^{LP2}	:	lowpass-filtered leg angles
γ_{pot}	:	leg angle from potentiometer output
γ^{TD}	:	touchdown leg angle
γ_{des}^{TD}	:	desired touchdown leg angle

$\dot{\gamma}$	:	leg angular speed; measured hip speed obtained by differentiating the measured potentiometer angle γ^{pot}
$\dot{\gamma}_{com}$	:	commanded leg angular speed
$\dot{\gamma}_{com}^{Fl}$, $\dot{\gamma}_{com}^{St}$	:	commanded leg angular speeds during the flight or stance phase
i_{actual}	:	actual current provided to the motor from the motor amplifier
i_{des}	:	desired motor current generated from the PD controller
i_{limit}	:	maximum motor current available, limited by a current limiter
J_{leg}	:	moment of inertia of the leg about the hip joint
k	:	spring stiffness of the leg
KE	:	kinetic energy of the body; equal to T
K_P, K_D	:	PD gains for proportional term and derivative term
K_τ	:	motor torque constant
L	:	effective length of the planarizer boom
L	:	Lagrangian
m	:	body mass
$\omega_{estimated}$	:	estimated motor speed
ω_n	:	natural angular frequency
P	:	Poincaré map
$P^{Apex \to Apex}$	:	Poincaré map from one apex to the next
$P^{Apex \to TD}$	:	piecewise Poincaré map from apex to touchdown
$P^{TD \to LO}$	:	piecewise Poincaré map from touchdown to lift-off
$P^{LO \to Apex}$	:	piecewise Poincaré map from lift-off to apex
PE	:	potential energy of the SLIP model / robot; equal to U
PE_{elas}	:	elastic potential energy of the leg spring
PE_{grav}	:	gravitational potential energy of the body
ϕ_{mid}	:	sweep mid-angle; mid-angle of touchdown and lift-off angles
ϕ_{sweep}	:	sweep angle

q , q_i	:	general coordinate
r	:	effective leg length; distance between the hip joint and the toe tip
r_0	:	effective leg length at rest
$\dot{r}$	:	time derivative of the leg length r
$\overline{\dot{r}^{LO}}$	:	average of the time derivative of leg length at lift-off
$\overline{\dot{r}^{TD}}$	:	average of the time derivative of leg length at touchdown
$\overline{\dot{r}_{\min}}$	:	average of the minimum time derivative of leg length
$\overline{\dot{r}_{\max}}$	:	average of the maximum time derivative of leg length
R	:	total gear ratio of four gear stages
Σ	:	Poincaré section, cross-section of the Poincaré map
T	:	kinetic energy in the Lagrangian; equal to KE
T	:	total torque transmission ratio of four gear stages
T_f	:	flight duration
T_s	:	stance duration
τ^{Hip}	:	hip torque
τ^{Hip}_{com}	:	commanded hip torque
τ^{Hip}_{des}	:	desired hip torque generated by the hopping controller
τ^{Hip}_{max}	:	maximum hip torque available
τ^{Motor}_{des}	:	desired motor torque
$\tau^{Motor}_{estimated}$	:	estimated motor torque
U	:	potential energy in the Lagrangian; equal to PE
x	:	horizontal position measured with respect to the initial condition
$\dot{x}$	:	forward speed
$\dot{x}_{des}$	:	desired average forward speed
$\dot{x}^{Apex}_{des}$	:	desired forward speed at apex

$\dot{x}_n^{Apex}$	:	forward speed at apex in the n-th hopping cycle
$\underline{x}_n$	:	discrete state vector in the n-th hopping cycle
$\underline{x}_n^{Apex} = (z_n^{Apex}, \dot{x}_n^{Apex})$	:	discrete state vector at apex in the n-the hopping cycle
z	:	vertical position of the COM from the ground level
z_{des}	:	desired height of the COM
z^{Apex}	:	height of the COM at the apex
z_{des}^{Apex}	:	desired apex height; target hopping height
z^{Bottom}	:	height of the COM at the bottom
z^{Clear}	:	toe clearance when the leg is vertical, i.e. the COM is at apex
z_{des}^{LO}	:	desired lift-off height
z_{des}^{TD}	:	desired touchdown height
$\dot{z}$	:	vertical speed
$\dot{z}_n^{Apex}$	:	vertical speed at apex in the n-th hopping cycle

Chapter 1. Introduction

1-1. Motivation

Practical mobility of machines using legs is desirable for environmental surveillance and rescue activities [1], [2]. The main reason is that wheeled vehicles often cannot negotiate rough terrain in environments such as mountain ranges and collapsed urban city structures [3], [4]. Hence, robotic legged locomotion has been studied for many years [5], [6], [7], [4], but the field is still developing. As a basic investigation of fast terrestrial mobility, the work detailed in this thesis deals specifically with robotic running of a single-leg robot inspired by biomechnical findings.

Looking to nature, animals run on rough terrain with impressive performance. For instance, cheetahs can gallop at 31 *m/s* and red kangaroos can leap at 16 *m/s* [8]. Hence, it is a reasonable and attractive idea to draw insight from animal locomotion. For three decades, researchers in fields related to biomechanics have been trying to understand the running motion of animals by simplifying models of animal musculoskeletal structures, because animals are redundant in kinematics, actuation, and control [10], [11], [9]. The model that has been most accepted is the Spring-loaded Inverted Pendulum (SLIP) model [12], [13], [14], [9]. The SLIP model motivated the design of the robot presented in this thesis.

1-2. Related Work

1-2-1. SLIP Model

The SLIP model consists of a point mass on a linearly springy leg. It represents the dynamics of the center of mass (COM) of a running animal's body and the *virtual* springy leg, as in Figure 1.1. This leg is not a physical leg but a conceptual leg whose mass is zero and whose length is equal to the distance between the COM location of the body and the location of the foot.

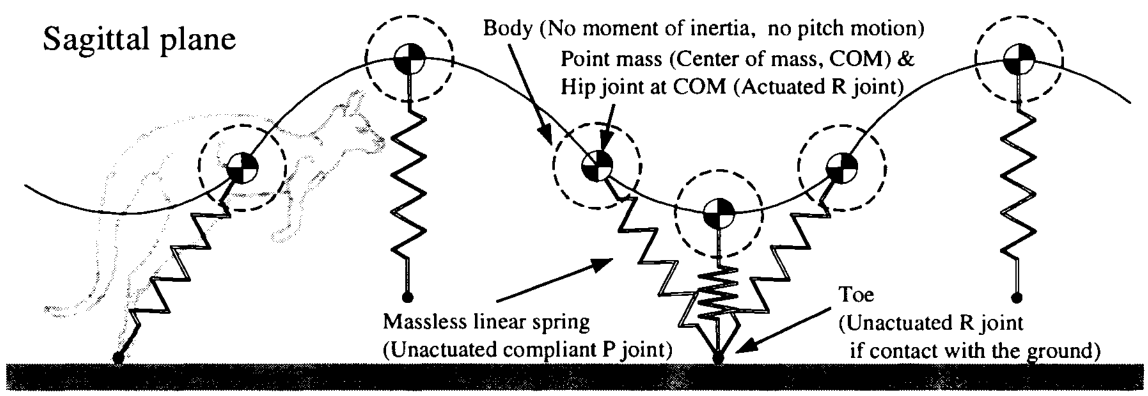

Figure 1.1 Running kangaroo and the Spring-loaded Inverted Pendulum (SLIP) model

The SLIP is the minimum model for running [9]. The body has two degrees of freedom (DOF) of translation in the sagittal plane and the leg has one DOF of rotation and one extensional DOF as in Figure 1.1. (The sagittal plane lies in the median plane dividing an animal into right and left halves and is perpendicular to the lateral and horizontal planes.) Since the body is represented by a point mass at the COM, its rotational inertia and pitch angle are not considered. The SLIP has only one actuated rotational joint at the hip, which is coincident with its COM. The compliant leg can be regarded as a prismatic joint with a spring while the leg is in contact with the ground, but it is unactuated.

The SLIP dynamics can be naturally stable without active balancing control provided that the leg can be oriented at an appropriate desired angle with some angular speed at touchdown [9], [22], [23], [24]. Due to this *self-stability* property, the control of a robot based on the SLIP model can be simplified. Note that this self-stability property was only recently discovered in the SLIP, though McGeer simulated the same idea on a bipedal robot model fifteen years ago [25].

Accordingly, a SLIP model-based design permits simple kinematics and control.

1-2-2. SLIP Model in Robotics

The SLIP model has been used for 20 years among robotics researchers [16], [17], [18], [19], [74]. Raibert and his co-workers at Carnegie Mellon University (CMU) and Massachusetts Institute of Technology (MIT) established the first milestone by using the SLIP as a dynamics model of their hopping robots [16]. Since then, most hopping and running robots have used Raibert's three-part locomotion controller based on SLIP models. This controller regulates the speed by preparing a stance sweep angle of the leg in flight, the pitch posture by using a leg sweep torque in stance, and the hopping height by thrusting the extensible leg in stance. In order to allow the use of this controller, their planar hopping robots had two actuators per leg: one to rotate the leg and one to thrust the leg. By contrast, the SLIP model has a spring to bounce without thrust. Consequently, Raibert's hoppers required more complexity in mechanism and actuation than the SLIP model did.

One clear example of the use of a SLIP model is a simulation of the bipedal running control of a full-sized and human-shaped robot, HRP1 [20]. Though the robot has two arms and two legs with 28 DOF, they are controlled in such a way that the COM and the virtual leg from the COM to the foot contact point with the ground can be treated using a SLIP model. As a result, the robot with complex mechanisms and dynamics is controlled using a two-DOF model when it is on the ground and a three-DOF model when it is in the air. This leads to successful running with a simple controller although it cannot be implemented due to motor torque limitations of existing technologies.

There has been extensive use of the SLIP model in the modeling and control of legged robots. On the other hand, the SLIP mechanism itself has never been developed and validated experimentally. In other words, many researchers have applied the SLIP model to their robots with complex mechanisms, but no robot with the kinematics of the

SLIP model has been constructed and evaluated experimentally. To date, the Bow Leg hopper [17] at CMU is one of the closest in design to the SLIP model. It has a passive compliant leg though it is a nonlinear curved fiberglass sheet spring, instead of the linear spring used in the SLIP model. The compliant leg is preloaded in flight using an actuator, and the total number of actuators is two while the number for the SLIP model is only one. Moreover, its COM is located below the hip to allow the body to be self-righting while the SLIP model has its COM located at the hip joint. Therefore, this robot cannot really be regarded as a realization of the SLIP model.

1-2-3. Past ARL Work in Robotics

The robot presented in the thesis is highly inspired by the robots built in the Ambulatory Robotics Laboratory (ARL) at McGill University. The SLIP model has been successfully used in modeling and control of all the following robots:

- MONOPOD II: demonstrated that two electrical motors are sufficient for a running one-legged robot [26].
- Scout II: demonstrated that one electrical motor per leg allows for maneuverability in quadruped bounding [27]
- RHex: demonstrated that one electrical motor per leg and PD control for leg angle is sufficient for six-legged locomotion [28], [29].

These achievements of past ARL researchers have inspired the demonstration in the thesis that the SLIP model can also be utilized as the basis for a hopping robot, in its own right.

1-3. Objectives

The SLIP model was adopted as a basis of the robot design presented here. The objectives of this thesis are as follows:

- To study the feasibility of a SLIP-model realization
- To design and construct a SLIP robot with one actuator
- To implement a simple controller on the SLIP robot
- To demonstrate fast running of the SLIP robot
- To validate the SLIP model experimentally
- To investigate stability (periodicity at steady state and robustness) of the SLIP robot.

The SLIP robot is designed based on the features and advantages studied in the past research work. Construction will be inexpensive, and control will be relatively simple. The simple SLIP architecture with a single actuator should be sufficient for the running motion on level surfaces only [9]. To the author's knowledge, the SLIP robot is the first robot of its kind in terms of kinematics and the number of actuators as shown in Table 1.1.

Table 1.1 Comparison to previous work

Robot University	Monopod [16] MIT	Bow Leg Hopper [17] CMU	Kenken [74] TITECH	SLIP robot McGill
Kinematics	More complex than SLIP			SLIP
Models for analysis and control	SLIP			SLIP
# of actuator(s)	2			1

1-4. Thesis Organization

The structure of this thesis is as follows. In Chapter 2, the conceptual design of the mechanical parameters and controller of the SLIP robot is described. In Chapter 3, the numerical simulation of the SLIP robot with the mechanical parameters and controller from the previous chapter is described. In Chapter 4, the detailed design and experimental setup of the SLIP robot is described. In Chapter 5, the experimental results are presented and discussed. This thesis ends with conclusions and suggested future work in Chapter 6.

Chapter 2. Conceptual Design

2-1. Chapter Introduction

This Chapter begins with the determination of the three main mechanical parameters for a one-legged hopping robot model: mass, leg stiffness, and rest leg length. The robot model is presented as part of a feasibility study model for the Spring-loaded Inverted Pendulum (SLIP). Detailed mechanical designs are considered in Chapter 4. A simple hopping controller is prepared after the determination of the three parameters. Both in the mechanical parameter and controller designs, the SLIP model and the related biomechanics findings are exploited. This exploitation is necessary to obtain reasonable design values, for no SLIP design has been presented in the literature and a rigorous mathematical analysis of nonlinear and intermittent SLIP dynamics would be overly involved and beyond the scope of a Master of Engineering (M.Eng.) thesis. In fact, the differential equations for the stance-phase dynamics are analytically non-integrable [83], and the solution remains an open problem [80].

Following the virtual leg of the SLIP model, the prismatic joint of the robot presented here is not actuated. This feature is beneficial in terms of implementation but is not ideal in all respects. Since the hip actuation couples the dynamics in the forward direction and vertical direction, there is no possibility of direct or independent thrust input in order to regulate hopping height or vertical speed. This is a challenging constraint when designing a hopping controller to maintain a constant hopping height while simultaneously achieving a desired forward speed. This issue is partially solved by explicitly designing the mechanical system for which the desired motion is natural response to reasonable initial conditions. To be precise, a desired toe clearance height is taken into account when a leg length is determined, and the leg length is considered when a target forward speed is determined. Such a design is based on the hypothesis that the self-stability property is embedded in the SLIP mechanism [9].

2-2. Choice of Mechanical Parameters

This section describes the procedure to select the mechanical parameters. First of all, the SLIP model consists of a point mass with a springy leg. There are three mechanical parameters to be determined in order to simulate a SLIP robot: body mass m, spring stiffness k, and rest leg length r_0. Those mechanical parameters and state variables used are shown in Figure 2.1.

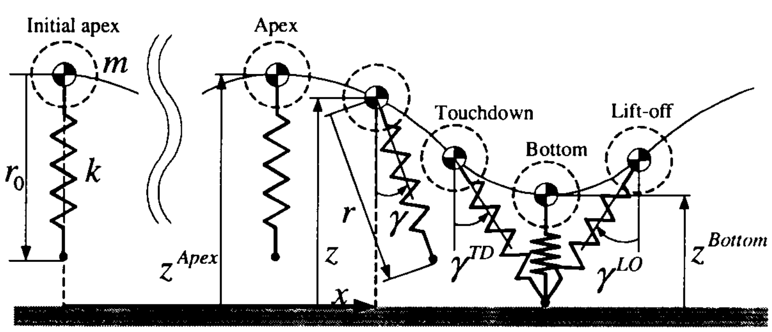

Figure 2.1 Mechanical parameters, state variables, and coordinates

2-2-1. Body Mass

A hip actuator, a leg, and structural parts are essential robot components for the experimental platform presented later. The total mass for these components, shown in Table 2.1, is 0.320 *kg*.

Table 2.1 Part masses for robot body components

Part name	Manufacturer	Mass (kg)
R/C Servo (hip actuator)	Hitec	0.146
Leg shaft	SDP/SI	0.055
Leg bushing	SDP/SI	0.66
Leg spring	Associated Spring-Raymond	0.015
Mechanical structure components	-	0.038

The robot in this thesis is regarded as a research prototype whereas the future goal is a highly mobile autonomous robot for practical applications. Therefore, it is not crucial for this prototype robot to contain an embedded computer, a motor amplifier, batteries and others onboard. Considering the case of an autonomous platform, however, the masses for those components would need be taken into account. Table 2.2 provides an estimate of those additional masses:

Table 2.2 Part masses for future implementation components

Part name	Manufacturer	Mass (kg)
PC104 embedded computer	VersaLogic	0.185
Motor amplifier	iXs Research Corp.	0.035
I/O board	VersaLogic	0.090
Power supply board	VersaLogic	0.300
Flash car board	VersaLogic	0.175
R/C car 6-cell battery pack	Panasonic	0.360

An aluminum block will be attached on the robot to represent the masses for the future implementation of a motor amplifier and an embedded computer. It weighs 0.220 *kg*. Other parts are not taken into account for the time being. Thus, the total mass of the body m is 0.540 *kg*.

2-2-2. Leg Spring Stiffness

The selection of the leg spring stiffness will determine the natural frequency of the spring-mass vibration in the robot's vertical stance dynamics model [16]. The natural frequency f_n and the natural angular frequency ω_n can be expressed in terms of the spring stiffness k and the mass m:

$$f_n = \frac{1}{2\pi}\omega_n = \frac{1}{2\pi}\sqrt{\frac{k}{m}} \tag{2.1}$$

or

$$k = (2\pi f_n)^2 m\,. \tag{2.2}$$

As in Eq. (2.2), the natural frequency and mass of the robot's vertical dynamics model can determine the spring stiffness. Since a mass value is already selected previously, once a natural frequency value is found, it can be used to obtain a spring stiffness value.

To arrive at an appropriate natural frequency, findings in physiology are used as guidance. The model commonly used to explain the animal motion is called the Spring-loaded Inverted Pendulum (SLIP) model. The concept of a virtual spring to model the animal leg occurs often in physiology and biomechanics papers [10], [11], [12], [13], [14], [9]. Researchers analyzed data from running animals and concluded that the COM motion of running animals can each be explained using a linear spring. In these experiments, the equivalent spring constants are obtained converting the maximum ground force and the distance between the COM position and the support foot when the virtual line joining these two points is vertical. Furthermore, these spring constants are substituted into Eq. (2.1) to obtain natural frequencies for animals. These sets of data and equations, especially the ones related to the natural frequency of running animals, are used here.

Two equations are obtained which relate the natural frequency during a complete stride to the size (mass or length) of animals, by plotting Farley's *et al* experimental data [14] in Figure 2.2. The corresponding data are listed in Table 2.3. Using a best fit power law, the relation to the body mass and to the leg length are obtained:

$$f_n = 3.0m^{-0.19}, \tag{2.3}$$

$$f_n = 1.0r_0^{-0.58}. \tag{2.4}$$

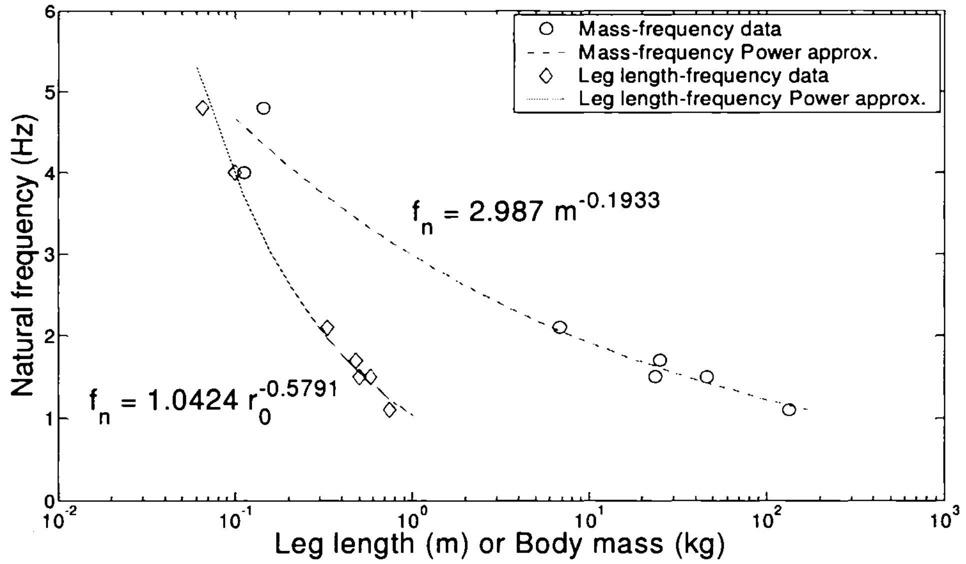

Figure 2.2 Natural frequency during a complete stride vs. body mass and vs. leg length of animal SLIPs

Table 2.3 Animal data reproduced from [14] with dimension-less speeds

Animal	**Body mass** m [kg]	**Leg length** r_0 [m]	**Speed** $\dot{x}$ [m/s]	**Dimension-less speed** $\dot{x}/r_0$ [1/s]
Kangaroo rat	0.112	0.099	1.8	18.2
White rat	0.144	0.065	1.1	16.9
Tammar wallaby	6.86	0.33	3.0	9.1
Dog	23.6	0.50	2.8	5.6
Goat	25.1	0.48	2.8	5.8
Red kangaroo	46.1	0.58	3.8	6.6
Horse	135	0.75	2.9	3.9

Since the leg length is not selected yet, the equation relating natural frequency to mass is more useful. Accordingly, a spring stiffness value is selected using Eq. (2.3).

The rule of thumb used in the ARL is 2.0 *Hz* for the natural frequency for a hopping locomotion [30]. This rule is the result of many years of experience working with compliant legs. However, the mass values of all the past robots are much heavier. For instance, RHex approximately weighs 8.0 *kg*. If a natural frequency is calculated using Eq. (2.3) with 8.0 *kg* of mass, the frequency of a similar size of animals is 2.0 *Hz*, which is the same value as the rule of thumb. Therefore, it might be safe to say that the desired natural frequency is well predicted by Eq. (2.3).

From Eq. (2.3), it is found that for a body mass of 0.5 *kg*, the natural frequency would be 3.4 *Hz*, while for a body mass of 1.0 *kg*, it would be 3.0 *Hz*. In the case of our robot, too high a frequency is not desirable since an actuator must swing the leg forwards and sweep backwards in a hopping cycle, and the actuator performance is bounded. Also, too high a frequency reduces the stance time, which reduces the capacity to inject energy into the spring potential energy and the duration to propel the robot by a hip torque. Consequently, it would be reasonable to use 3.0 *Hz* as a start.

Using Eq. (2.2) with a natural frequency of 3.0 *Hz* and a mass of 0.540 *kg* leads to a spring stiffness for the robot leg of 192 *N/m*. The closest value among off-shelf springs is 193 *N/m* from Associated Spring Raymond, and this is the value selected.

The leg spring stiffness also determines the robot's stance duration, because the stance duration can be approximated by half the resonant period of the spring-mass vibration in the robot's vertical stance dynamics model [16]. The stance duration T_s estimated from half the resonant period of such a spring-mass vibration is

$$\begin{aligned} T_s &= \frac{1}{2} \cdot 2\pi \frac{1}{f_n} \\ &= \pi \sqrt{\frac{m}{k}}. \end{aligned} \tag{2.5}$$

Substituting the selected spring stiffness of 193 *N/m* into Eq. (2.5), an estimated stance duration of 0.166 *s* is obtained.

2-2-3. Leg Length

The effective leg length of the robot at rest, r_0, is the maximum distance between the tip of the toe and the joint axis of the hip. In the flight phase, the leg length is kept at its rest value r_0, and in the stance phase, the leg is shortened as the spring deflects.

The leg length design has the following requirements:

1. The leg length must be short enough that the leg will not stub on the ground when the leg passes the vertical at the *apex* (highest position in flight). That is, the toe clearance must be sufficient so that the leg clears the ground at the apex;
2. The joint travel must be long enough that the body will not hit the travel limit of leg compression even at the *bottom* (lowest position in stance);
3. The leg length must be short enough that the actuator can propel the robot with a torque lower than its stall torque;
4. The leg length must be long enough that the desired forward speed can be achieved at an actuator speed slower than its no load speed.

The first two requirements will be used to obtain an initial value of the leg length, and the other two requirements will be checked later by simulation and experiment.

If the desired toe clearance z^{Clear} is set to 0.050 m based on the first requirement, then the desired apex height z^{Apex} becomes

$$\begin{aligned} z^{Apex} &= r_0 + z^{Clear} \\ &= r_0 + 0.050. \end{aligned} \tag{2.6}$$

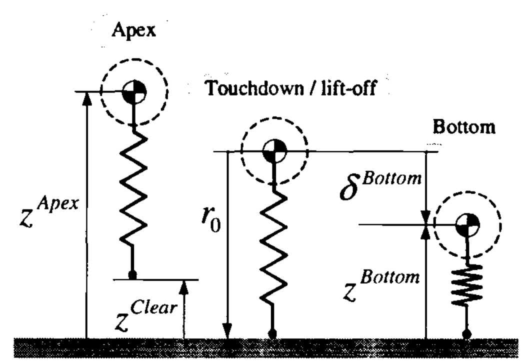

Figure 2.3 Variables and coordinates of vertical hopping

The necessary travel in the second requirement is calculated using the energy conservation law for vertical hopping. Although the hopping considered here is not purely vertical, this approximation is reasonable according to Raibert [16]. At the apex, the vertical speed is zero and the spring deflection is also zero. At the bottom, the vertical speed is zero. Therefore, conservation of energy yields

$$mgz^{Apex} = mgz^{Bottom} + \frac{1}{2}k(\delta^{Bottom})^2, \tag{2.7}$$

where z^{Apex} is the height of the COM at the apex, z^{Bottom} is the height of the COM at the bottom, and δ^{Bottom} is the spring deflection when the body is at the bottom, shown in Figure 2.3. To avoid hitting the servo casing (the main mechanical structure of the robot body) on the ground during the stance phase, the height at bottom z^{Bottom} must be higher than $0.025\,m$. Including a small margin of $0.010\,m$, the desired height at bottom z^{Bottom} is set to be $z^{Bottom} = 0.035\,m$, which yields the spring deflection at bottom δ^{Bottom}:

$$\begin{aligned} \delta^{Bottom} &= r_0 - z^{Bottom} \\ &= r_0 - 0.035. \end{aligned} \tag{2.8}$$

Solving Eq. (2.7) with Eqs. (2.6), and (2.8) for r_0 yields $r_0 = 0.121\,m$. Thus, the designed leg length at rest is set to $r_0 = 0.120\,m$, and it leads to

$$\begin{aligned} z^{Apex} &= 0.170\,m, \\ z^{Bottom} &= 0.035\,m, \\ \delta^{Bottom} &= 0.085\,m. \end{aligned} \tag{2.9}$$

This leg length value agrees to some extent with the value obtained from one of Farley's *et al* equations based on biomechanical experimentation [14]. In that paper, the relation between mass and leg length in animal is

$$r_0 = 0.16m^{0.33}. \tag{2.10}$$

The animal leg length corresponding to a mass of 0.54 *kg* would be 0.131 *m*.

In summary, the rest length of the leg, r_0, is set at 0.120 *m* so that the leg is short enough for the toe clearance and has the necessary prismatic joint travel for the spring deflection. The sufficiency of the hip torque and speed of the leg will be confirmed later.

2-3. Hopping Controller

In this section, the concept of a hopping controller for the SLIP robot is described. It consists of a finite state machine and two controllers based on the states found in the state machine. The controllers are realized using proportional-derivative (PD) control to regulate leg motion, which leads to stabilization of the entire system.

2-3-1. State Machine and Switching Control

Phases and Events of SLIP Dynamics

In general, legged robots are event-driven intermittent dynamical systems. They change their dynamical characteristics depending on their leg conditions, i.e. whether or not their legs are on the ground. For instance, legged robots are often modeled as a manipulator when only one leg is on the ground, a closed-chain mechanism when more than one leg are on the ground, and a floating mechanism when no leg is on the ground.

Those conditions are called *phases* in the field of legged locomotion [16]. In the case of a one-legged hopping robot, there are only two possible phases: flight phase and stance phase. A *flight phase* is a phase in which the leg is not on the ground and the whole robot is in the air. A *stance phase* is a phase in which the leg is on the ground and the leg supports and propels the body.

The phase switches are driven by *events*. In a one-legged hopping robot, there are two events: *touchdown* and *lift-off*. Touchdown is an event taking the system from flight into stance while lift-off takes the system from stance into flight. The robot repeats the cycle of alternating phases as long as it is stable, as shown in Figure 2.4.

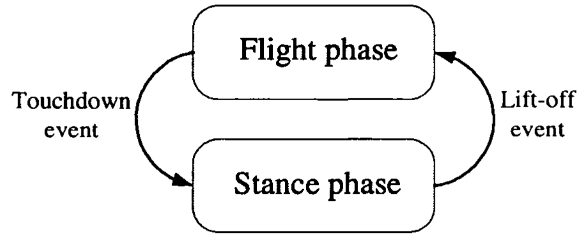

Figure 2.4 Dynamics cycle of a one-legged hopping robot with two phases and two events, which is adopted as states and state transitions in the state machine for the SLIP robot.

States and State Transitions for Control

A *state machine* is a framework consisting of a set of *states* that a system exists in and a set of *state transitions* that are conditions / actions taking the system from one state to a next [78]. Note that the term "state" here is different from the concept of a state variable such as x, $\dot{x}$, z, and $\dot{z}$. A state machine can represent the state flow of the closed locomotion cycle for the hopping controller used.

Two states are defined for the SLIP robot: flight phase and stance phase, as shown in Figure 2.4. The start state is presumed to be the flight phase since the simulation and experiment start from an apex. The end state is omitted since the running cycle is expected to repeat indefinitely. There are two state transitions: touchdown event and lift-off event. These state transitions are used for the state-dependent switching [51] of controllers.

As many states can be used in a state machine as desired, and therefore, a hopping controller can possibly possess more states than the number of phases, which invites complexity. In such a state machine, a state transition does not necessarily require a change in the robot's dynamical characteristics. For instance, Raibert's robots had five states as shown in Figure 2.5 [32]. In the stance phase, his robots had to detect state transitions for four states in order to control the prismatic actuator. Accordingly, each detection of state transition required fine accuracy, and each controller required a short convergence time, owing to a short stance duration.

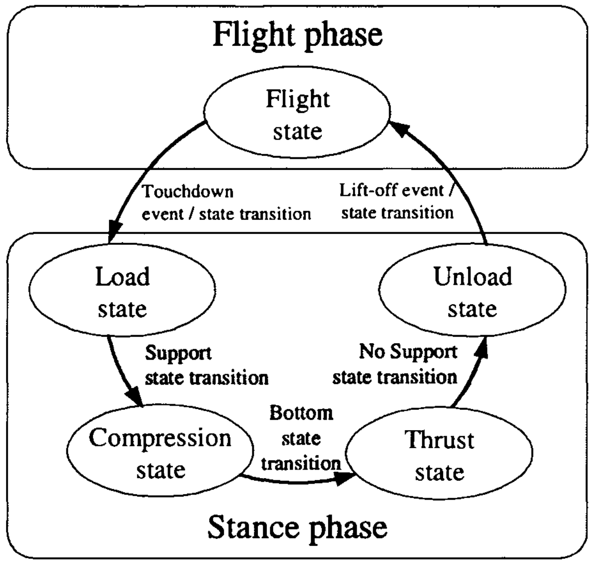

Figure 2.5 State machine for Raibert's planar one-legged hopping robot. The five states are shown along with the state transitions. Based on [32].

The SLIP robot might need only one controller for each phase since the control of the SLIP model is inherently simple [9]. Moreover, switching control adds more complexity in analysis and controller design owing to its hybrid dynamics / control issues [51], [52], [53]. Therefore, it is desirable to restrict the number of states defined. Unlike Raibert's state machine, thus, the stance and flight phases are adopted as the only states and the touchdown and lift-off events as the only state transitions, as in Figure 2.4. This is presumably the simplest state machine possible for the SLIP mechanism and is used as a basis for the hopping control scheme.

2-3-2. Self-stability

Two properties of the SLIP model, self-stability and symmetry, are addressed here. These properties are natural response to given initial conditions, which reduces the control efforts required.

The ideal SLIP model has a self-stability property discussed in [9], [22], [23], and [24], and relevant work on dynamics models is presented in [25] and [46]. Self-stability means that, given an appropriate initial condition, the SLIP model runs steadily without adaptive control because naturally stable dynamics is inherent to the mechanical system. The first requirement for the self-stability is an appropriate leg angle at touchdown. The second requirement is a leg angular speed for leg drawdown before touchdown. The last requirement is that the hip torque used to swing the leg in the flight phase does not input any energy to the system. The SLIP model without any energy input and dissipation can be considered energy-conservative. If these conditions are satisfied, then the leg in the stance phase is naturally swept to its appropriate lift-off angle, and the unforced response yields a repetitive locomotion cycle. The hopping controller for the robot here focuses on attaining or conceptually reproducing these conditions.

In the idealized SLIP model, as well, the stance path of the COM is symmetric with respect to the vertical line drawn from the stance toe. The stance toe is fixed to a touchdown point throughout the phase. Accordingly, the absolute values of the touchdown and lift-off leg angles are the same, and the motion is the same if it is followed in a time-reversing manner. This *symmetry property* is discussed in [16], [47], [48], [49], and [45], and the general symmetry of dynamics on which some of those papers are based is discussed in [50].

Periodic locomotion is strongly attributed to the symmetry of dynamics above. The symmetry is desirable according to the cited literature. In the robot here, however, symmetric angles are not employed for touchdown and lift-off to achieve a desired apex height, discussed later. Even though the symmetry in leg angle is not maintained, it is expected that some other symmetries, such as in vertical motion, will still exist and periodic locomotion will be generated. This periodicity will be examined in simulation and experimentation.

2-3-3. Forward Speed and Sweep Angle

The desired sweep angle of the leg in the stance phase is derived here from the speed of the same animal size (virtual leg length) as the SLIP robot. This approach is taken due to its simplicity of analysis. This sweep angle is a basis for the later selection of the absolute leg angles at touchdown and lift-off, γ^{TD} and γ^{LO}, respectively, as shown in Figure 2.1.

From animal data in [14], 34 *deg* is an average value of the touchdown leg angle at a physiologically equivalent speed. It seems that the touchdown leg angle of animals is not dependent on their size (mass or dimension) but on their forward speed. It is intuitively reasonable that the stride is longer if animals want to run faster, i.e. the longer the running stride is, the faster an animal runs, and vice versa [43]. An average forward speed can be calculated using an equation in [14] and [16], which includes the touchdown leg angle:

$$\dot{x} = \frac{2r_0 \sin \gamma^{TD}}{T_s}, \tag{2.11}$$

where $\dot{x}$ is the forward speed, r_0 is the rest length of the leg, γ^{TD} is the leg angle at touchdown, and T_s is the stance duration. To derive this equation, the COM trajectory in stance is approximated by the horizontal line drawn between the touchdown and lift-off positions, shown in Figure 2.6. As well, it is assumed that the lift-off angle is equal in magnitude to the touchdown angle, which is the symmetry property discussed earlier.

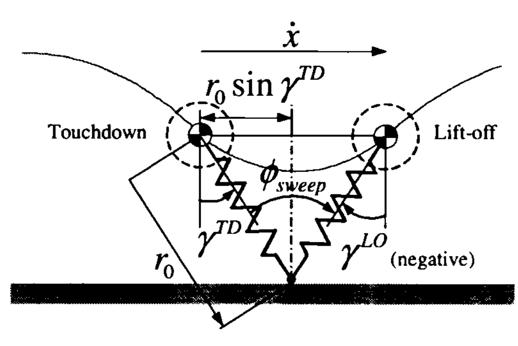

Figure 2.6 SLIP model in the stance phase. Based on [16].

Solving Eq. (2.11) for the touchdown angle,

$$\gamma^{TD} = \sin^{-1}\left(\frac{\dot{x}T_s}{2r_0}\right). \tag{2.12}$$

Thus, the touchdown angle is dependent on the forward speed, stance duration, and rest leg length. Forward speed is taken to be variable, but the other two are considered fixed because those values are determined from mechanical characteristics as discussed earlier in this chapter. The stance duration T_s is estimated using Eq.(2.5). Thus, Eq. (2.12) indicates that the touchdown leg angle is exclusively dependent on the desired forward speed. Based on Eq. (2.12), a plot of touchdown leg angle versus desired forward speed is shown in Figure 2.7. Though it is a function of arcsine, in the region of interest, it is almost linear and therefore, the correspondence between the two is clear.

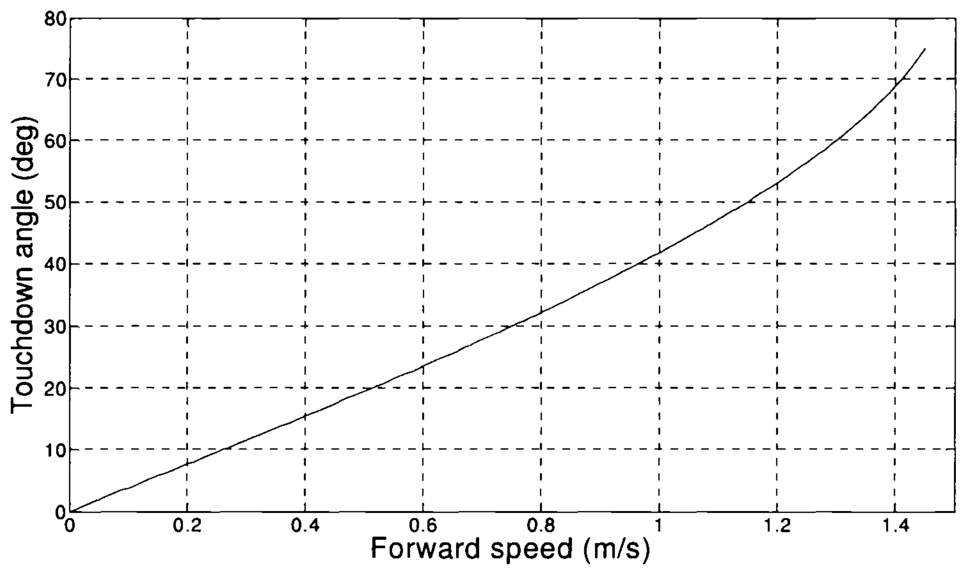

Figure 2.7 Touchdown leg angle vs. forward speed for m = 0.54 kg, k = 193 N/m, and r_0 = 0.120 m

The chosen value for the desired forward speed is 0.80 m/s because the touchdown angle corresponding to 0.80 m/s in Figure 2.7 is 32.3 deg, which is close to the average animal value of 34 deg. Note that this target forward speed of 0.80 m/s yields the fastest dimension-less speed of 6.7 leg lengths per second compared to other one-legged robots, as shown in Appendix A. The lift-off angle γ^{LO}, which is measured positive counterclockwise from the downward vertical, should be approximately $-32.3 deg$ due to the symmetry property discussed earlier. Consequently, the sweep angle ϕ_{sweep} is twice as wide as the touchdown angle γ^{TD}, or approximately 65 deg.

Though the derived sweep angle of 65 *deg* is used for the hopping controller here, the symmetry with respect to the vertical between touchdown and liftoff is not. The mid-angle of the touchdown and lift-off angles (or the *sweep mid-angle* ϕ_{mid}) is shifted from the vertical line to a certain positive angle. The shift amount of 7.5 *deg* is obtained by trial and error, based on the desire to repeat the target hopping height z_{des}^{Apex}. The need for this asymmetry is described subsequently.

2-3-4. Apex Height and Asymmetric Gait

The *apex* is the highest point in the flight phase, and the *apex height* is also commonly called the *hopping height*. The desired apex height z_{des}^{Apex} for every hopping cycle is set to 0.170 *m*. This desired apex height is achieved basically by selecting an appropriate rest leg length r_0 for the predetermined body mass m and leg stiffness k, considering energy conservation with respect to vertical hopping motion. However, since the assumption of conservation is not completely correct for a system with dissipation, if the desired height is achieved at one apex, the next apex height will be lower. This height loss can be compensated using an asymmetric forced sweep. The sweep mid-angle ϕ_{mid} is offset since the desired sweep angle ϕ_{sweep} of 65 *deg*, derived from the fixed target forward speed $\dot{x}_{des}$, cannot be modified provided that the coupling between the sweep offset and forward speed is not significant. Asymmetric touchdown and lift-off angles result in the difference between the touchdown and lift-off heights of the body COM. This adds an extra height to the apex height. The shift amount of the mid-angle is obtained empirically, based on the desire to repeat the target apex height z_{des}^{Apex}. The desired touchdown angle γ_{des}^{TD} is shifted to 40 *deg* in the case of the SLIP robot. As a result, the desired lift-off angle γ_{des}^{LO} is $-25\,deg$, and the offset of the sweep mid-angle from the vertical line is $\phi_{mid} = 7.5\,deg$.

This touchdown leg angle of 40 *deg* will be validated to be appropriate for the self-stability property, as well, by observing steady running without adaptive stabilization control in simulation and experimentation. Simple evaluations for the achievement of the desired apex height will be conducted in simulation and experimentation. The ability to achieve variable heights is left for future work.

2-3-5. Realization Using PD Control

The overall dynamics of the SLIP is a combination of the dynamics of the two distinct phases. The hopping controller for the SLIP robot is a combination of two controllers, based on the state machine discussed earlier. The two controllers are switched by reflex, following the previous work on state-dependent switching control applied to robotic legged locomotion [16], [44], [54], [55], [56].

The following single form of proportional-derivative (PD) controller is used both for the two phases:

$$\tau^{Hip} = K_P(\gamma_{com} - \gamma) + K_D(\dot{\gamma}_{com} - \dot{\gamma}), \tag{2.13}$$

where τ^{Hip} is the desired hip torque (the torque applied between the body and the leg by the single actuator of the robot), K_P and K_D are PD gains, and γ_{com} and $\dot{\gamma}_{com}$ are the commanded leg angle and leg angular speed. While the form of the two PD controllers for the two phases is same, the commanded angles and gains are different. They are switched depending on the phase, so that the generated torques are appropriate for the two distinct phases, as shown in Figure 2.8. This hopping controller requires only minimal sensing of leg angle and angular speed for the PD control, and detection of ground contact for phase switching. No information of the COM position is needed for control.

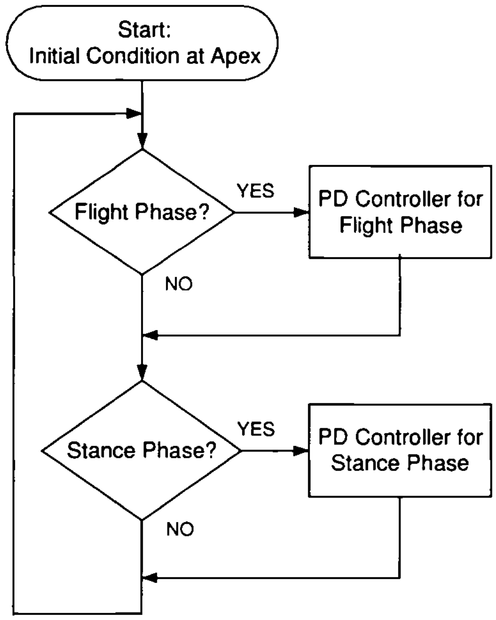

Figure 2.8 Flowchart of the hopping control scheme

When a touchdown sensor detects ground contact, the stance-phase PD controller becomes active by reflex. A step change to the lift-off angle is commanded to the PD controller, and a desired torque is generated and updated in real-time. Similarly, the flight-phase controller is turned on as soon as the ground contact ends. In simulation, the leg toe height is used for ground contact detection, and in experimentation, an infrared distance sensor attached near the leg toe is used.

The commanded leg angle throughout the flight phase, γ_{com}^{Fl}, is constant and equal to the desired touchdown angle γ_{des}^{TD}, i.e. $\gamma_{com}^{Fl} = \gamma_{des}^{TD} = 40\ deg$. The commanded leg angle throughout the stance phase, γ_{com}^{St}, is equal to the desired lift-off angle γ_{des}^{LO}, i.e. $\gamma_{com}^{St} = \gamma_{des}^{LO} = -25\ deg$. The commanded leg angular speed is set to $\dot{\gamma}_{com} = 0\ deg/s$ throughout the cycle. These values allow the hip torque to produce the protraction, drawdown, retraction, and follow-through motion, shown in Figure 2.9, by using the only one form of PD controller with two sets of commanded angles and gains.

The leg motion obtained from these PD controllers is as follows. When the leg is far from the commanded angle γ_{com}, a large torque towards the commanded angle is generated because of the first term of the controller that consists of the angle error in the leg angle $(\gamma_{com} - \gamma)$ multiplied by a gain K_P. When the leg rotates rapidly in either direction, a decelerating torque in the opposite direction to the leg rotation is generated. This is because the second term consists of the leg angular speed error $(\dot{\gamma}_{com} - \dot{\gamma})$ multiplied by a gain K_D. As a result, the motor action at the start of each phase is dominated by the proportional term and tends to drive the leg towards the value required at the end of the phase. At the end of each phase, the motor action is dominated by the derivative term and tends to decelerate the leg rotation, as shown in Figure 2.9. The use of the decelerating torque is inspired by the successful running controller for the Scout II robot [19].

The running performance created by this hopping controller is evaluated in Chapters 3 and 5.

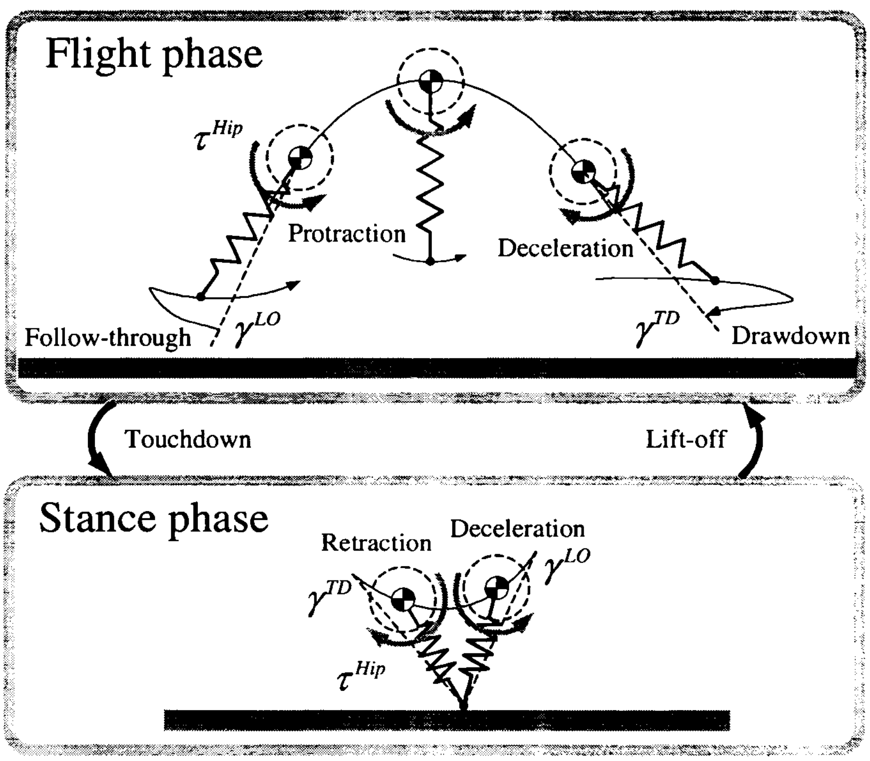

Figure 2.9 Leg motion regulated by the two PD controllers, one for each phase

2-3-6. Energy Distribution and Transfer

As well as the input-loss balance of energy, the internal distribution of energy is one of the key points for periodic and steady hopping. The total mechanical energy of a SLIP robot consists of gravitational potential energy PE_{grav}, elastic potential energy PE_{elas}, and kinetic energy KE:

$$\begin{aligned} E_{total} &= PE_{grav} + PE_{elas} + KE \\ &= mgz + \frac{1}{2}k\delta^2 + \frac{1}{2}m(\dot{x}^2 + \dot{z}^2). \end{aligned} \tag{2.14}$$

Kinetic energy comes only from the forward speed $\dot{x}$ and the vertical speed $\dot{z}$ since there is no rotational motion in the body. No translational and rotational motion in the leg is considered since the mass of the leg is included in the body mass.

As long as vertical hopping is concerned, the kinetic energy at lift-off is equal to the kinetic energy at touchdown, and the potential energy at lift-off is also equal to that at touchdown, assuming that the system is conservative. However, in the case of planar hopping, kinetic energy can be transferred to potential energy, and vice versa. The energy distribution of KE and PE can collapse easily when an asymmetric gait directly affect the distribution. From this point of view, four issues relating the asymmetric gait and the energy distribution can be examined as follows:

1. The kinetic energy at lift-off is smaller than that at touchdown;
2. The gravitational potential energy at lift-off is larger than that at touchdown;
3. Part of the forward speed at touchdown is transferred to vertical speed at lift-off;
4. The sum of the kinetic energy and the gravitational potential energy is same at touchdown and lift-off, when the energy input and loss throughout each stance phase are well balanced at steady state.

The first two statements relate to the transfer from kinetic energy to gravitational potential energy, caused by the offset of the sweep mid-angle ϕ_{mid}. The touchdown angle is larger in magnitude than the lift-off angle. A large touchdown angle means that the touchdown height is low, and a smaller lift-off angle means that the lift-off height is high. This allows the gravitational potential energy to increase from touchdown to the following lift-off. Simultaneously, in order for hopping motion to be periodic, the total mechanical energy should be maintained at a desired level with an appropriate distribution. To achieve this, the kinetic energy should decrease from touchdown to lift-off by the difference in gravitational potential energy at touchdown and lift-off. In this case, the sum of the kinetic energy and the gravitational potential energy is the same at touchdown and at lift-off.

The third statement is about the distribution of forward and vertical speeds. Because of the smaller lift-off angle in magnitude, the spring's decompressing motion contributes to the restoration of the vertical component in velocity rather than to that of the forward component. Therefore, some forward speed at touchdown is transferred to vertical speed at lift-off, via the energy temporarily stored in the spring.

The fourth statement will be validated by simulation and experimental results. The successful cyclic motion indicates that the total mechanical energy is well maintained at a certain level in the dynamical system. It is presumed that energy input and loss only take place during the stance phase.

These energy distribution issues presented here will be discussed again in later chapters dealing with the simulation and experimentation.

2-4. Chapter Summary

In this chapter, the mechanical parameters for the simulation model of a SLIP robot were determined based on the SLIP model and its dynamics, as well as findings in biomechanics. Then, a hopping controller that considers the two phases of the hopping cycle was described. These parameters and controller are used in Chapter 3 to study the feasibility in simulation. They are then used to construct a robot in Chapter 4.

Chapter 3. Simulation

3-1. Chapter Introduction

Single-legged planar hopping robots are nonlinear and event-driven intermittent dynamical systems, and due to this complexity, it is difficult to obtain analytical solutions to the dynamics equations. The underactuated mechanism of the Spring-loaded Inverted Pendulum (SLIP) and the actuator saturation make analytical solutions even more difficult. To date, the analytical solution to the equations of motion for the COM of the SLIP model remains open [80] even after extensive research in biomechanics [80], robotics [16], [81], and applied mathematics [45], [82], because the stance-phase dynamics is non-integrable [83]. Only approximate solutions under assumptions, such as the neglect of the gravity during the stance phase, are found in the literature [80], [81]. Numerical simulation is therefore preferred to predict and investigate the behavior of a SLIP and its hopping stability.

This chapter presents the dynamics model of a SLIP, the implementation of the SLIP in numerical simulation, and the simulation results. The main objective is to study the feasibility of the SLIP robot with the parameters and controller from Chapter 2. The equations of motion are implemented in simulation using the Matlab and Simulink software packages [57]. The stability of the resulting hopping motion in the simulation is analyzed. The mechanical parameter values determined in Chapter 2 are evaluated in the simulation as well.

3-2. Dynamics Model

Equations of motion are used in simulation as the dynamics model of the SLIP robot. The essential characteristics of the SLIP model, a ballistic flight for the flight phase and a planar harmonic stance for the stance phase, are preserved, shown in Figure 3.1.

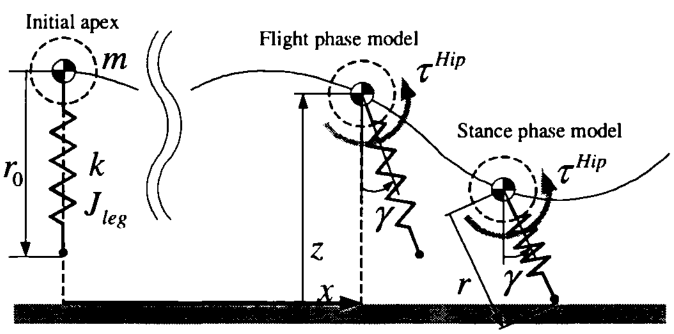

Figure 3.1 Dynamics model for the two phases with mechanical parameters and state variables

In the flight phase, it is assumed that the center of mass (COM) follows a ballistic trajectory since the COM is a point mass and the mass of the leg is included in the mass of the body. However, the inertia of the leg is still taken into account in order to calculate the effect of the hip torque on leg motion. The motion of the COM and that of the leg are assumed to be decoupled.

For the flight phase, the following equations of motion are derived:

$$\begin{aligned} \ddot{x} &= 0, \\ \ddot{z} &= -g, \\ \ddot{\gamma} &= \frac{\tau^{Hip}}{J_{leg}}, \end{aligned} \tag{3.1}$$

where x is the horizontal position measured with respect to the initial condition, z is the vertical position from the ground level, γ is the leg angle at the hip with respect to the vertical, τ^{Hip} is the hip torque, J_{leg} is the moment of inertia of the leg, and g is the gravitational acceleration. The derivation of these equations is presented in Appendix B.

In the stance phase, the SLIP is represented as a harmonic system in the sagittal plane. The inertia of the leg is neglected. Contact between the toe and the ground is modeled as a pin joint so that the toe does not slip on the ground surface. Friction of this contact is neglected. The effects of impact at touchdown and lift-off are neglected as well though there is impact between the toe and the ground and there is impact between the prismatic joint slider and the mechanical stop of the prismatic joint on the actual robot. Due to the leg spring, the energy loss during the touchdown impact is effectively negligible [25] although, if the vertical speed at the impact is too high, the loss can be significant to analysis and control [33], [34]. A pre-deflection δ_{pre} of the spring is set to eliminate spring chattering in the flight phase in order to avoid the energy loss associated with this vibration.

For the stance phase, the following equations of motion are derived:

$$
\begin{aligned}
\ddot{r} &= r\dot{\gamma}^2 - g\cos\gamma + \frac{k(r_0 + \delta_{pre} - r)}{m} - \frac{b\dot{r}}{m}, \\
\ddot{\gamma} &= -\frac{2\dot{r}\dot{\gamma}}{r} + \frac{g\sin\gamma}{r} + \frac{\tau^{Hip}}{mr^2},
\end{aligned}
\tag{3.2}
$$

where r is the leg length, γ is the leg angle, k is the spring coefficient, r_0 is the rest leg length, δ_{pre} is the pre-deflection of the spring, m is the body mass, b is the damping coefficient of the prismatic leg joint, τ^{Hip} is the hip torque, and g is the gravitational acceleration. The derivation of these equations is presented in Appendix B. The parameter values used in the simulation are as in Table 3.1.

Table 3.1 Parameters for dynamics models

Parameters	Symbols	Values	Units
Body mass	m	0.540	kg
Spring constant	k	193	N/m
Rest leg length	r_0	0.120	m
Pre-deflection	δ_{pre}	0.024	m
Leg damping constant	b	0.35	$N\ s/m$
Leg inertia	J_{leg}	2.0×10^{-4}	$kg\ m^2$
Gravitational acceleration	g	9.805	m/s^2

3-3. Controller

Figure 3.2 shows the simulation loop diagram, and the shaded part is the hopping controller used in the simulation. The symbol γ denotes the leg angle and the symbol τ^{Hip} denotes the hip torque. The hip torque is input to the equations of motion, which represent the robot dynamics and are numerically integrated. The output from the integration is used to generate the desired torque for the next time step. The appropriate commanded angle γ_{com} for the state of the robot is chosen depending on the phase. The commanded leg angular speed $\dot{\gamma}_{com}$ is set to be zero throughout the cycle. The desired hip torque τ_{des}^{Hip} is generated from

$$\tau_{des}^{Hip} = K_P(\gamma_{com} - \gamma) + K_D(\dot{\gamma}_{com} - \dot{\gamma}), \tag{3.3}$$

where K_P and K_D are PD gains. The PD gains used in the simulation are in Table 3.2. The maximum hip torque available is limited in the simulation because the maximum motor current i_{limit} is set to $5A$, assuming that the hip actuator is to be a geared DC motor on the actual platform. The maximum hip torque τ_{max}^{Hip} is estimated at:

$$\tau_{max}^{Hip} = K_\tau i_{limit} RT$$
$$= 4.14 \times 10^{-3} \cdot 5.0 \cdot 173 \cdot (0.90)^4 \quad (3.4)$$
$$= 2.3\ Nm,$$

where K_τ is the motor torque constant, R is the total gear ratio of four gear stages, and T is the torque transmission ratio. The values for K_τ and R are from [79], and that for T is estimated. This maximum hip torque τ_{max}^{Hip} is used as the commanded torque τ_{com}^{Hip} when the desired hip torque τ_{des}^{Hip} is greater than this value and is truncated:

$$\tau_{com}^{Hip} = tran[\tau_{des}^{Hip}]. \quad (3.5)$$

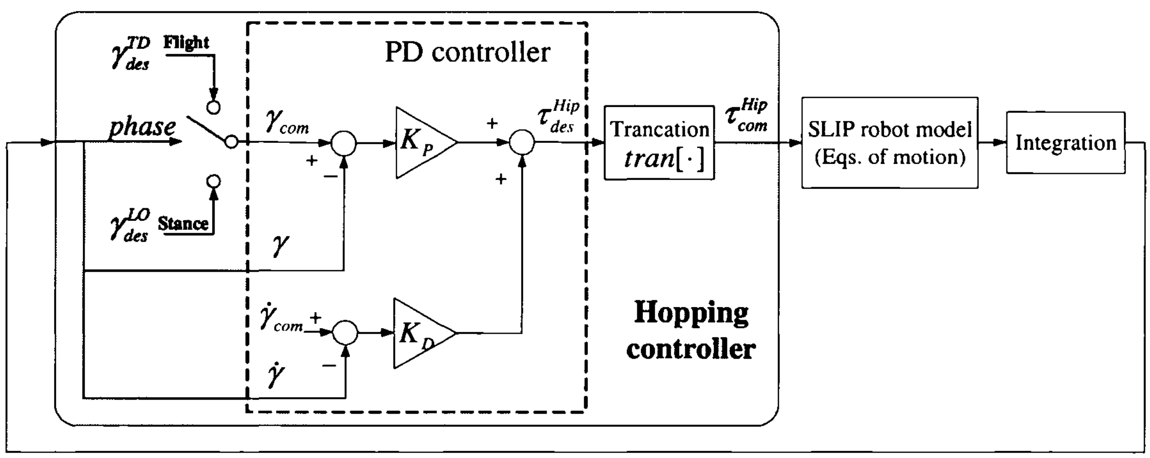

Figure 3.2 Diagram of the hopping controller in the entire simulation loop

The PD gains are initially set using Ziegler-Nichols Tuning [75] and then adjusted to achieve the desired touchdown and lift-off angles.

Table 3.2 PD gains in simulation

Phase	Gain	Symbol	Value	Unit
Stance	P	K_P	1.40×10^{-3}	Nm/deg
	D	K_D	2.20×10^{-5}	Nms/deg
Flight	P	K_P	1.20×10^{-3}	Nm/deg
	D	K_D	3.00×10^{-5}	Nms/deg

The control update and sensor sampling are done at each integration step. A 4^{th}-order variable time step Dormand-Prince integrator is used. The maximum step size and the tolerance are both 1×10^{-3}.

3-4. Stability Analysis

It is essential to clarify metrics to evaluate the running performance of the SLIP robot. Simulation and experimental results are to be assessed using stability criteria.

Since no universal definition of legged-locomotion stability has been established, researchers use various stability criteria of legged running including phase plots by Michalska *et al* [61], [26], and regions of attraction by Schwind *et al* [62]. Phase plots and regions of attraction plots do not contain all the information needed to understand the entire system dynamics. Nonetheless, these methods are recommended in [67], [68], and [69] because they are useful to determine stability even when analytical methods are overly involved or impossible to apply.

These criteria are employed in this thesis because they are compatible with numerical data from both simulation and experimentation. To simplify the stability analysis of experimental data with inaccuracies, *stability* is fundamentally defined as follows:

- Ability or condition for a system to converge to a steady state inside the neighborhood of the desired sate and to maintain the motion.

This leads to the stability definition used for the SLIP robot's locomotion:

- Ability or condition for the robot to converge towards the desired state of an apex height and an average forward speed and to run continuously.

Based on this definition, the criteria above are discussed next, and stability analysis is performed using these criteria in the next section and in Chapter 5.

Phase Plots and Limit Cycles

A *phase plot* is a plot of a state variable vs. the time derivative of the state variable. In general, a phase plot of dynamical motion with repetitive cycles, such as in a robot's running, results in a closed orbit [64], [32], [61], [65]. If this closed orbit repeats tracing the same pattern periodically, it is called a *limit cycle* [66], [67], shown in Figure 3.3. The limit cycle means that the dynamics of the state variable on concern is *periodic* at steady sate.

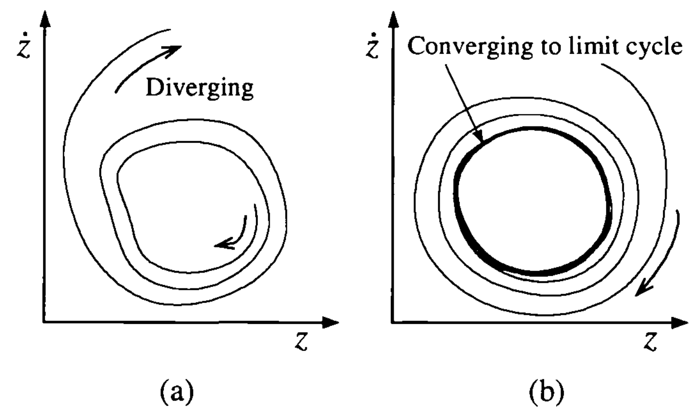

Figure 3.3 Phase plots: (a) a diverging curve and (b) a curve converging to a limit cycle

In the case of the locomotion dynamics of the SLIP robot, during the flight phase, the COM follows a simple ballistic curve under the influence of gravity, and during the stance phase, it follows a harmonic curve. If the combination of the two curves forms a closed periodic orbit in the phase plot, it is a limit cycle. In a limit cycle, the dynamical condition of the state variable at any point (e.g. at the apex point) in one hopping cycle returns to the same condition at the same point in the next hopping cycle.

Transition Plots and Regions of Attraction

The generation and trace of a limit cycle means that the system's motion is periodic at steady state, but it may easily diverge with a small disturbance like at the unstable equilibrium point of an inverted pendulum. Therefore, in order to declare the SLIP robot is "stable" according to the stability definition for locomotion earlier, the ability to attract arbitrary neighborhood states to the desired state is required. This ability is defined as *robustness* in the thesis. The robustness of locomotion can be examined using the concept of the *Poincaré map* [63], [70], [71], [72], which is a mathematical tool to analyze periodicity of dynamical systems. This map is also called the *stride function* [25] or *return map* [73], [45], [62]. It is often used in legged locomotion analysis owing to the inherent characteristics of periodic locomotion cycles.

The Poincaré map is a discrete map between two consecutive states which are at the same reference point in the periodic cycle, e.g. a map from an apex sate to the next apex state. To define a Poincaré map, a reference point of the periodic cycle is specified, and a continuous-time system is discretized at this point and is represented by a discrete-time system. Then, the robustness problem is replaced by the convergence problem of arbitrary discrete states at the reference point of the cycle. For details of the Poincaré map, see Appendix C.

By applying this concept to the SLIP robot, the apex in the hopping cycle is selected as the reference point in the periodic motion, and the state vector $\underline{x}_n^{Apex} = (z_n^{Apex}, \dot{x}_n^{Apex})$ is chosen as the discrete state to be analyzed. Note that no analytical mapping equation is required here since apex states are available from numerical simulation or experimentation.

The apex states are plotted as open circle markers ($\circ$), and the traces of these states are drawn to show convergence transitions. Let this plot be referred to as a *transition plot*. By obtaining the sequence of apex states for enough cycles, the convergence per cycle and the steady-state error for a particular IC can be viewed, shown in Figure 3.4(a). The robot is regarded robust to the given IC if the state vector in the plot converges towards the desired state of $(z_{des}, \dot{x}_{des}) = (0.170, 0.80)$.

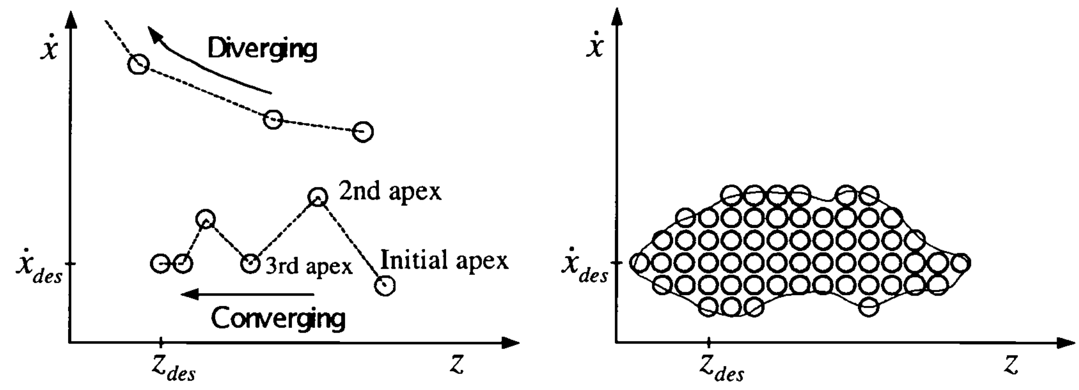

(a) (b)

Figure 3.4 (a) Converging and diverging transition plots in z - $\dot{x}$ plane; (b) Collection of congerged IC's and its inferred region of attraction in z - $\dot{x}$ plane

A large set of IC's should be examined in order to determine the range of IC's that are led or "attracted" to the desired state. Shown in Figure 3.4(b), the domain created by these IC points is called the *region of attraction* for the robot [62]. For the region of attraction plot, the traces of convergence transitions are not included. In the thesis, only the IC's possible are tested given the mechanical structure of the experimental robot.

In terms of robustness, the larger the region is, the more robust to disturbances the robot is considered. This is because each IC point can be regarded as the state with an error after being disturbed at a steady state.

To summarize the section, two measurement standards for stability are addressed: limit cycles in phase plots and regions of attraction created from transition plots. Limit cycles confirm periodicity at steady sate. The size of regions of attraction indicates the degree of robustness.

In the next section, a phase plot of the vertical position is examined for the simulation results. Furthermore, phase plots based on the experimental data of the leg angle and leg length in addition to that of the vertical position are discussed in Chapter 5. Transition plots for the apex state vector, $\underline{x}_n^{Apex} = (z_n^{Apex}, \dot{x}_n^{Apex})$, and regions of attraction are obtained and discussed for the simulation results next and the experimental results of Chapter 5.

3-5. Simulation Results

In all simulations in this thesis, the desired state of the center of mass (COM) is fixed at an average forward speed of 0.80 *m/s* and an apex vertical position of 0.170 *m* since these desired values were determined earlier, associated with the mechanical parameters.

Motion in Sagittal Plane

If the initial condition (IC), or the first apex condition, is the same as the desired state of a forward speed of 0.80 *m/s*, a vertical position of 0.170 *m* and a vertical speed of 0 *m/s*, then the robot model smoothly proceeds to a repetitive hopping cycle. The state at the 14^{th} apex (in about 5 *s*) is a forward speed of 0.63 *m/s* and a vertical position of 0.171 *m*. The forward speed is approximately 0.8 *m/s* when averaging of the whole cycle. This is due to the forward speed in the stance phase being faster than 0.80 *m/s*. This result first indicates that a SLIP robot using only one actuator is feasible. Second, the available torque, although limited by the motor performance, is sufficient for this motion. Lastly, a combination of two simple PD controllers is sufficient to sustain steady running motion for at least 5 *s*.

The next IC, a forward speed of $-0.60\,m/s$, a vertical position of 0.260 *m* and a vertical speed of 0 *m/s*, is a condition different from the desired state. In spite of the large initial error, the robot recovers its forward speed and adjusts its height. The apex state converges towards the desired state of the average forward speed of 0.80 *m/s* and the apex height of 0.170 *m*. The plot of the COM position in the sagittal plane is shown in Figure 3.5.

The approximate apex height of 0.170 *m* in the figure shows that the toe clearance is 0.050 *m* as desired, since the leg length in the flight phase is 0.120 *m*. The average bottom height (lowest height in stance) of 0.061 *m* is higher than the expected value of 0.035 *m*. The simulation value is more desirable since it can be considered that there is a larger safety margin in travel. In fact, if the first bottom was lower than 0.035 *m*, the determined margin might be too short for this IC since the height of the first bottom in the figure is already as low as the predicted value. Thus, the design procedure in Chapter 2 will not be iterated here for a lower bottom height as long as other critically desired values are achieved.

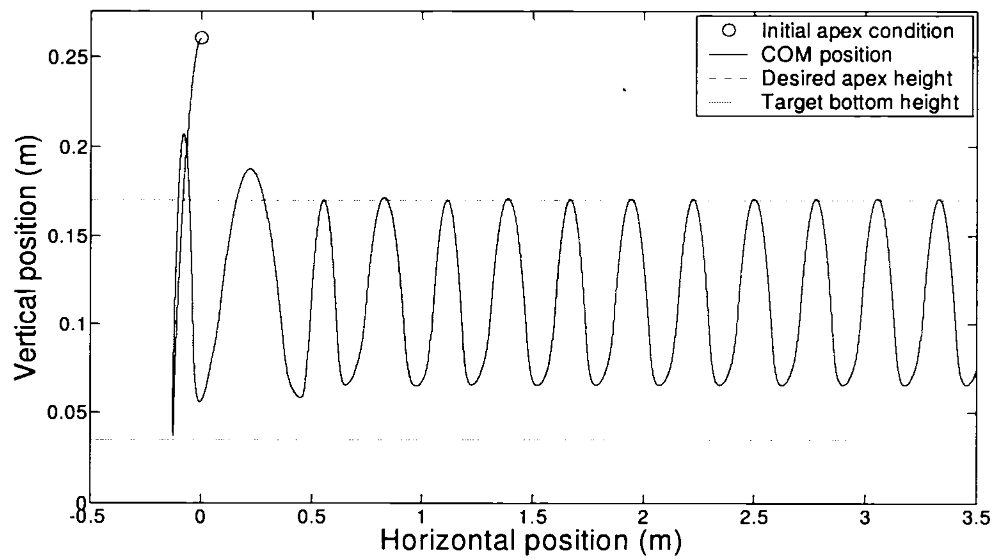

Figure 3.5 Simulation Data: Locus of the COM position in the sagittal plane

Phase Plot

The phase plot of the vertical position of the center of mass (COM), i.e. vertical speed versus vertical position, is shown in Figure 3.6. The IC is a forward speed of $-0.60 m/s$, a vertical position of 0.260 *m*, and a vertical speed of 0 *m/s*. The plot turns out to eventually trace a closed orbit, i.e. it converges to a limit cycle. One cycle represents one hopping cycle, and therefore, height converges quickly and becomes periodic at steady state. The apex and bottom heights can also be reviewed.

In Appendix D, a plot of the vertical speed versus vertical position evolving with time is shown using the same data set. The convergence with respect to time is seen in the plot.

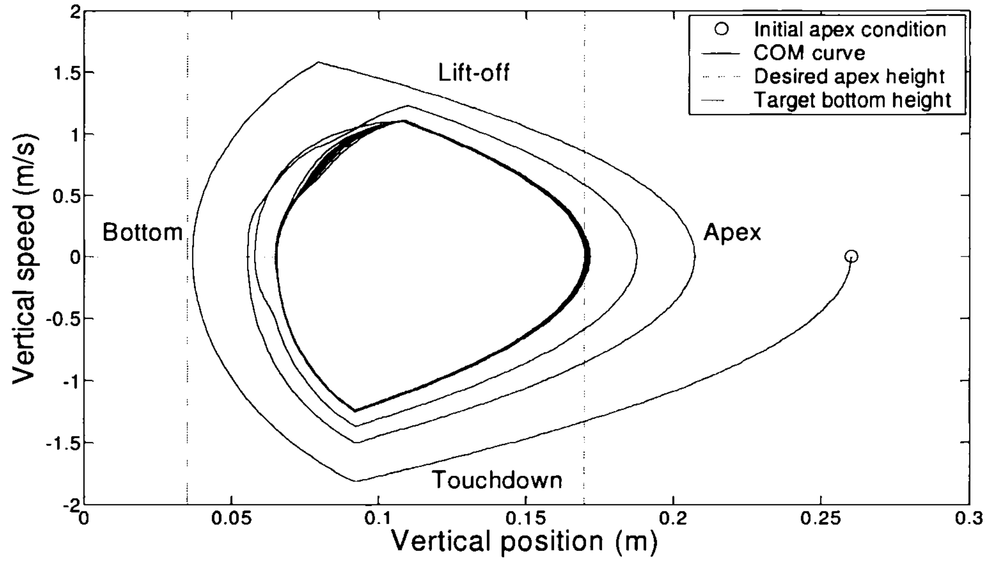

Figure 3.6 Simulation Data: Phase plot of the vertical position of the COM

Transition Plot and Region of Attraction

Using the same data set, the transition plot is plotted in Figure 3.7. The plot shows how it converges to a stable state. The state at every apex is plotted so that the convergence transition can be seen.

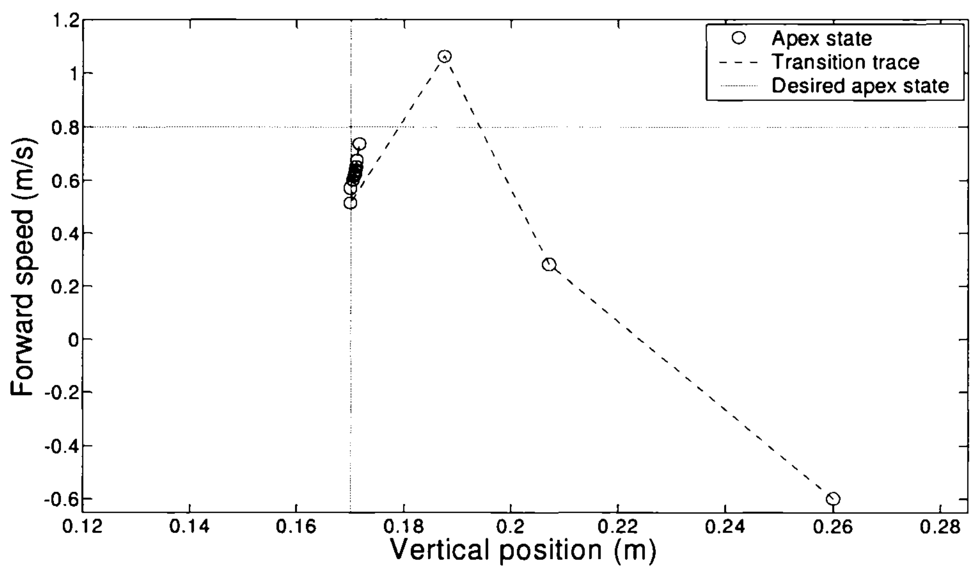

Figure 3.7 Simulation Data: Transition plot of the apex state for the IC of $\dot{x} = -0.60$ *m/s*, $z = 0.260$ *m* and $\dot{z} = 0$ *m/s*, considered as the state with a large error to the desired state

A region of attraction, shown in Figure 3.8, is constructed, testing 2115 points as IC's. The plot does not exhibit traces of transitions since only the IC's, i.e. the first apex states, are plotted. Two lines are drawn at 0.170 *m* and 0.80 *m/s*. An open circle marker (○) means that the IC point converges to the area inside the desired apex height range from 0.169 *m* to 0.173 *m* and the desired apex forward speed range from 0.61 *m/s* to 0.65 *m/s*. This apex height range covers the desired value, but this apex forward speed range is lower than desired so that the average forward speed becomes approximately 0.8 *m/s*. A plus marker (+) means that the leg length is shorter than 0.030 *m* at some point in the trajectory, though the leg length does not become 0 *m* and the point converges to the desired area. This value of 0.030 *m* comes from the physical limit of the actual robot structure. A cross marker (×) means that the IC does not converge to the desired area.

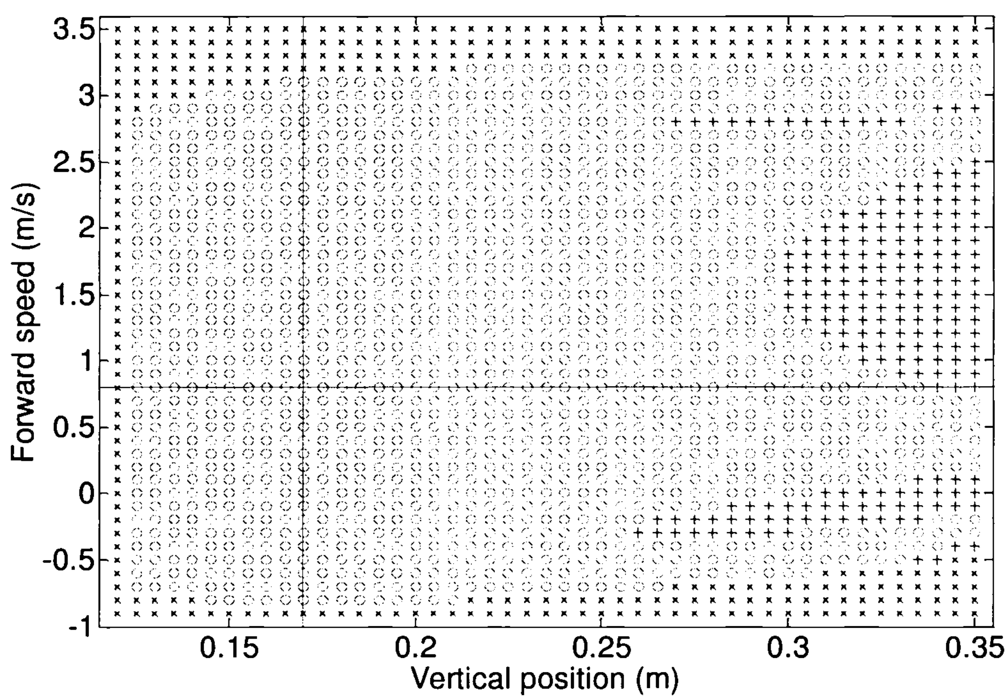

Figure 3.8 Simulation Data: Region of attraction. 2115 IC's are tested.

It is seen that the IC's in a large domain, even with such a large error as a negative forward speed of –0.5 *m/s*, converge to periodic hopping. This indicates that the gait produced by the SLIP mechanism and the controller is robust. Thus, it can be expected that a small disturbance from the actual environment will not prevent periodic hopping motion.

This robustness contributes the simplicity of the commanded leg angle γ_{com}. Commanding the same constant angle throughout each phase, rather than calculating new angles adaptively at each hop, has been found decent.

The simulation results obtained thus far indicate that the periodic and robust hopping motion of the SLIP can be realized using the chosen mechanical parameters and controller. The feasibility of other values for the mechanical parameters is discussed next.

Evaluation of Mechanical Parameters

Various values are tested in simulation to justify the selected set of mechanical parameter values. Since the body mass value of 0.540 *kg* is determined from the physical considerations, the other two parameters, leg spring stiffness and rest leg length, are evaluated here. When one parameter is evaluated, the rest of parameters are fixed to the selected values. The same IC as earlier, a forward speed of –0.60 *m/s*, a vertical position of $0.260m$ and a vertical speed of 0 *m/s*, is used because an IC with a large error to the desired sate highlights the resultant differences and assists the evaluation.

Figure 3.9 shows the COM trajectories for four different leg spring stiffness values. It shows that the leg stiffness of 193 *N/m* is the most appropriate among the tested values. The apex height is as desired only if the determined value is used. If the stiffness value is too small (e.g. $k = 130$ *N/m*), the robot cannot obtain a high apex height, probably because the hip torque is absorbed and the spring cannot provide a high vertical force. The hopping stride is narrow and cannot generate a high forward speed. As the spring stiffness becomes higher, the apex height at the steady state becomes higher. However, a value of 250 *N/m* yields relatively unstable motion since the robot model with this value takes two cycles to recover its gait and to hop forwards, and moreover, it takes an approximately twice longer horizontal travel to converge than the robot models with the two smaller values. If the leg is too rigid (e.g. $k = 310$ *N/m*), the leg cannot negotiate the disturbance and the COM of the body falls over backwards. This result is consistent with Full's *et al* hypothesis that the compliant leg mechanisms of animals generate robustness as well as reflex and high-level feedback control [9].

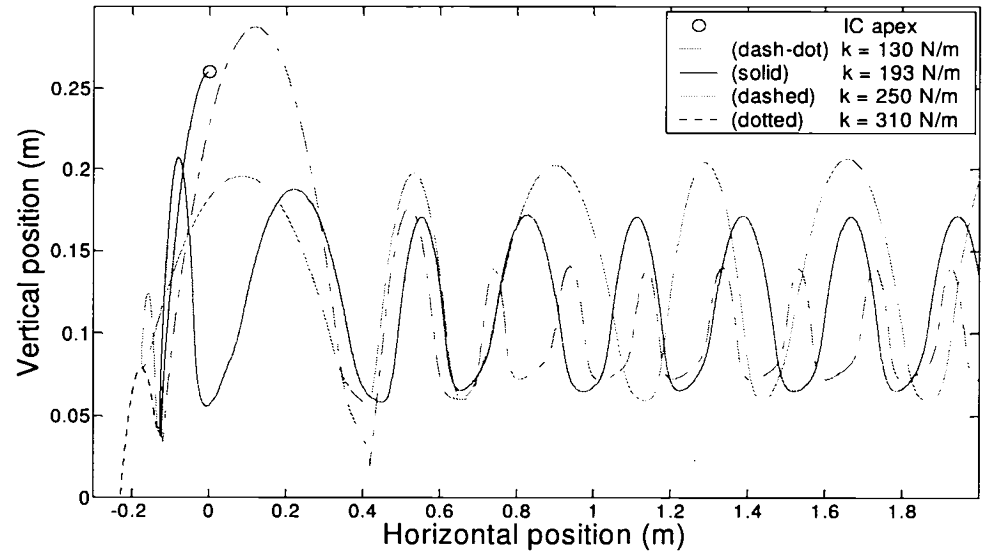

Figure 3.9 Simulation Data: COM trajectories for four different leg spring stiffness values with $m = 0.540kg$ and $r_0 = 0.120m$

Figure 3.10 shows the COM trajectories for four different leg length values. Interestingly, this figure is similar to the previous one. The determined leg length of 0.120 *m* is considered to be the most appropriate. One noteworthy observation is that with a leg length of 0.130 *m*, the COM starts periodic motion of two cycles with one narrow stride and one wide stride. This is a bifurcation to a period-2 limit cycle, which is an indication of collapse of the period-1 limit cycle motion. If this bifurcation proceeds, the motion will diverge. Thus, this value or greater is not desirable. In fact, a leg length of 0.140 *m* does not even produce one cycle of hopping and the COM of the body falls over backwards.

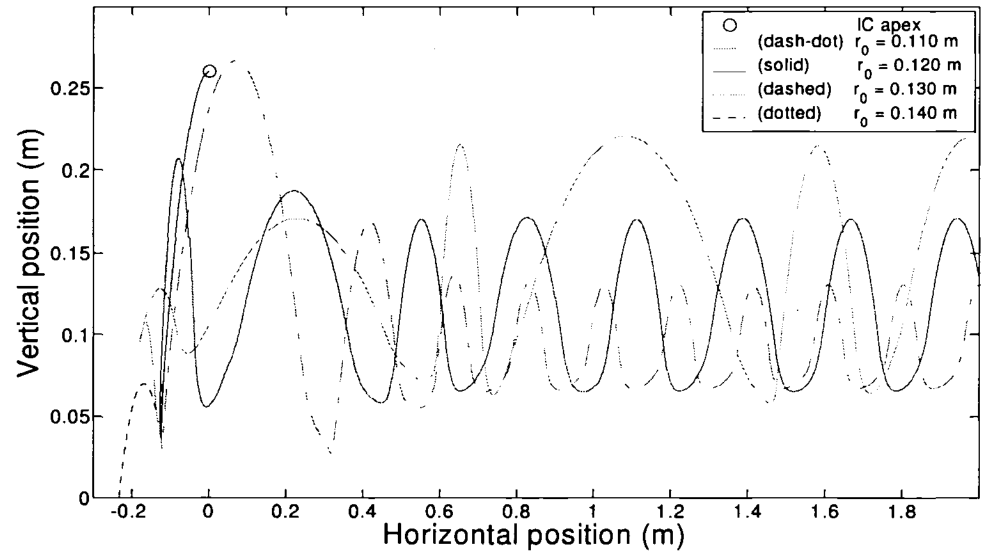

Figure 3.10 Simulation Data: COM trajectories for four different rest leg length values with $m = 0.540 kg$ and $k = 193 N/m$

To summarize, the selected set of mechanical parameters is found to be the only appropriate set since alternate sets of values lead to locomotion failures or undesirable motions.

Summary of Simulation Results

The simulation results lead to the following conclusions:

- Only one actuated DOF is sufficient to stabilize the SLIP robot in forward speed, apex height, and energy compensation;
- Available torque from a DC motor is effective to stabilize the SLIP robot;
- A combination of two simple PD controllers is sufficient to stabilize the SLIP robot;
- Employed set of mechanical parameters is adequate for desired motion;
- Alternate sets of mechanical parameters do not achieve desired motion.

The feasibility of the SLIP is therefore confirmed by the simulation.

3-6. Chapter Summary

This chapter presented a feasibility study using a numerical simulation of the SLIP robot with the mechanical parameters and controller determined in Chapter 2. First, the dynamics models of the two phases were described. Then, stability metrics were introduced. The simulation results were presented and the feasibility was confirmed. Lastly, the selected mechanical parameters were evaluated and validated, by comparing to the results obtained from alternate values. The resulting parameters and controller will constitute the foundation of an experimental platform in Chapter 4. The simulation results will also be discussed with the experimental results shown in Chapter 5.

Chapter 4. Experimental Platform

4-1. Chapter Introduction

A Spring-loaded Inverted Pendulum (SLIP) robot is designed and constructed, based on the features of the theoretical SLIP model. The body of the model possesses 2 DOF (degrees of freedom) of translation, (x, z), in the sagittal plane. The leg with respect to the body possesses 1 DOF of prismatic translation and 1 DOF of rotation, (r, γ). These features need be implemented on an experimental platform.

As for control, the SLIP robot has only one actuator at the hip joint, both for propelling the robot forwards and for adjusting the vertical hopping height. Unlike previous robots, the SLIP robot does not rely on a second actuator to thrust along the leg in order to stabilize its hopping height. This omission of a second actuator simplifies the mechanical design. On the other hand, the control law that can stabilize both the forward speed and the hopping height is more complicated than simple rotation of the leg. It requires the consideration of torque directions, as described in Chapter 2.

This chapter first describes the mechanical implementation details of the SLIP mechanism and planar motion. The leg mechanisms are implemented in the robot, but the body's planar motion feature is realized using an external mechanical structure referred to as the planarizer.

In order to determine the dimensions of the mechanical parts of the SLIP robot, the three values in Chapter 2, a body mass of 0.540 *kg*, a leg spring stiffness of 193 *N/m* and a rest leg length of 0.120 *m*, are used as a basis.

Next, the computer and electronic system to control the only actuated DOF is described. The actuator employed is a DC motor. The computer and electronic system is set up for a hopping controller program to regulate the current of the DC motor. The concept of the controller is the same as that in the simulation in Chapter 3. The program also includes the acquisition of the measured motion of the robot. Logged data from experiments are shown in Chapter 5, and the motion, servo performance, and stability of the SLIP robot are discussed there.

4-2. Mechanical Platform

This section describes the SLIP robot, a mechanical structure to constrain the robot motion, and the locations of the sensors to measure the robot state.

Robot Mechanisms and Components

The hopping robot is made up of a body and a leg. The body consists of a servo system casing, a sagittal-plane plate, and an aluminum block, shown in Figure 4.1. The servo system casing contains a direct current (DC) motor, a four-stage-gear mechanism, and a potentiometer. The leg consists of an upper leg bushing, a lower leg shaft, and an extension spring, shown in Figure 4.2. The bushing contains two linear bearings inside. Figure 4.3(a) shows a close-up sagittal view of the actual assembled SLIP robot at rest.

The three mechanical parameters, m, k and r_0, determined in Chapter 2 and justified in Chapter 3 are used to design and construct the SLIP robot. The total mass of the body component and the leg component here is equal to the chosen body mass m. The stiffness of the extension spring here is equal to the chosen leg spring stiffness k. The effective leg length here is designed such that the distance between the hip joint axis and the toe tip considered in the sagittal plane is equal to the chosen rest leg length r_0 if the robot is at rest.

The SLIP model possesses 2 DOF in its mechanisms. One actuated rotational DOF at the hip is realized using the servo system with the DC motor installed inside. Its geared output axis, shown in Figure 4.1, rotates the upper leg bushing component with respect to the body component.

The other DOF, one unactuated prismatic DOF of the springy leg, is realized between the upper leg bushing and the lower leg shaft. The lower leg shaft slides along in the upper leg bushing, inside of which there are linear bearings. An extension spring, rather than the compression spring of the theoretical SLIP model, is utilized to avoid buckling. Consequently, the springy leg is realized as a compliant, passive prismatic joint. A shortened and rotated configuration of the leg is shown in Figure 4.3(b).

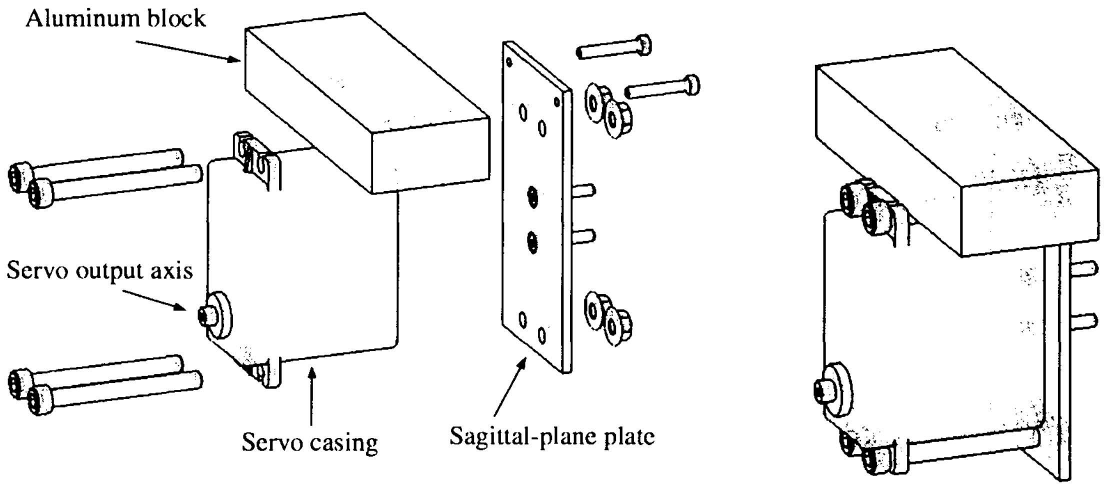

Figure 4.1 Exploded and assembled body components

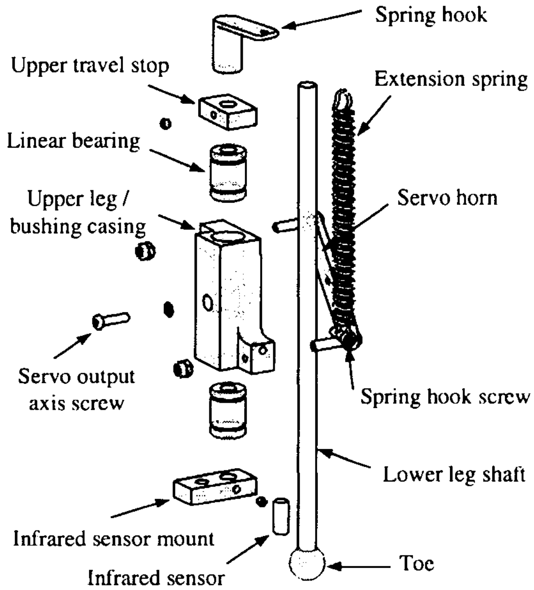

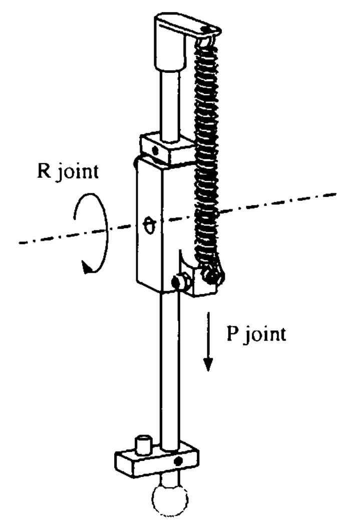

Figure 4.2 Exploded and assembled leg components

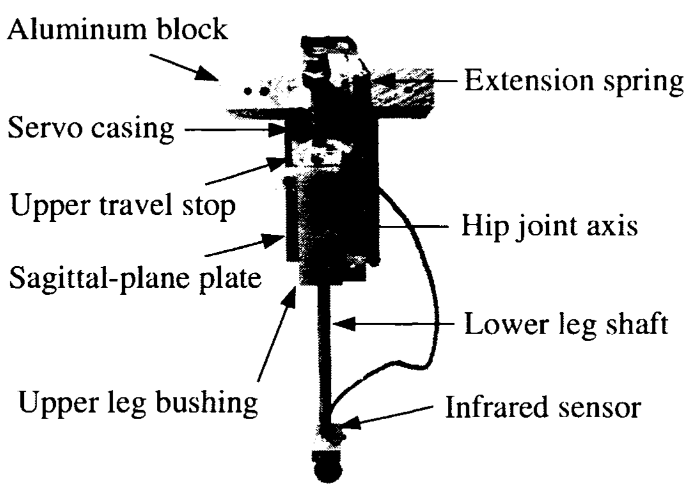

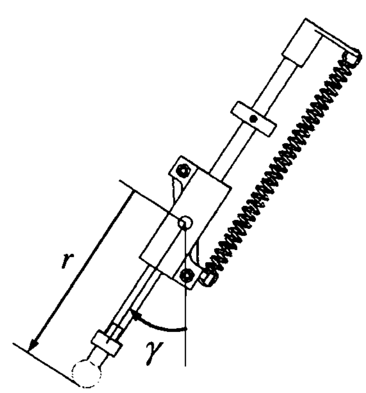

(a) (b)

Figure 4.3 (a) Sagittal (side) view of the actual robot at rest; (b) Shortened and rotated configuration of the leg with state variable coordinates for the effective leg length r and the leg angle γ. Note that γ has the opposite direction to the theoretical and simulation models

Planarizer Structure

The SLIP model is a planar model in the sagittal plane. In order to construct a hopping robot to mimic the SLIP model, the robot must only move in a plane. To realize this, the robot body needs be constrained in a plane approximating the sagittal plane. As well, rotational pitch motion of the body must be restricted. These are accomplished using an additional mechanical structure, referred to the planarizer. Figure 4.4 show the kinematic arrangement of the planarizer and the robot.

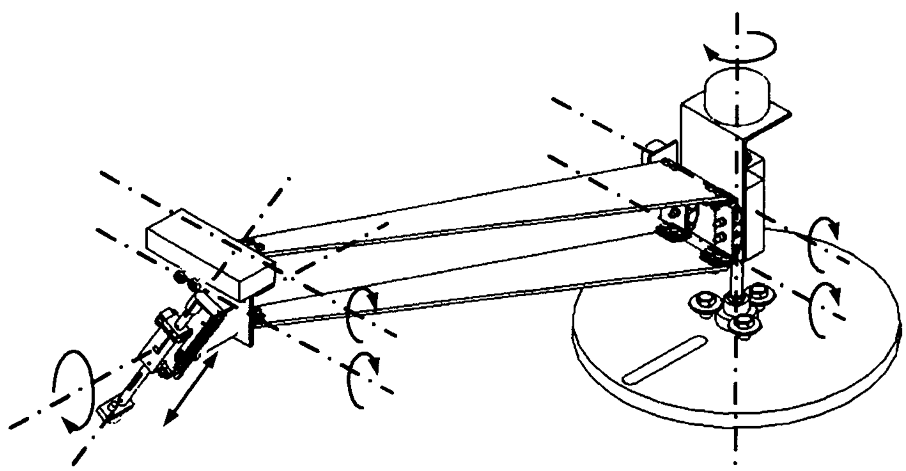

Figure 4.4 Kinematic arrangement of the robot and planarizer

The planarizer is basically a pivoted boom that allows the robot body to move only in the desired directions. This is a frequently adopted type of plane-constraint mechanism in legged locomotion [16], [17], [74]. As long as the arm of the planarizer is sufficiently long and its rotational motion around the vertical axis is slow, the robot's motion along the surface of a cylinder reasonably approximates planar motion. The advantage of this type is that the robot can travel in circles for a long distance. The boom here is constructed using a parallelogram mechanism. Figure 4.5 shows the mechanical CAD design of the SLIP robot and a planarizer. Figure 4.6 shows the actual setup of the robot and the planarizer.

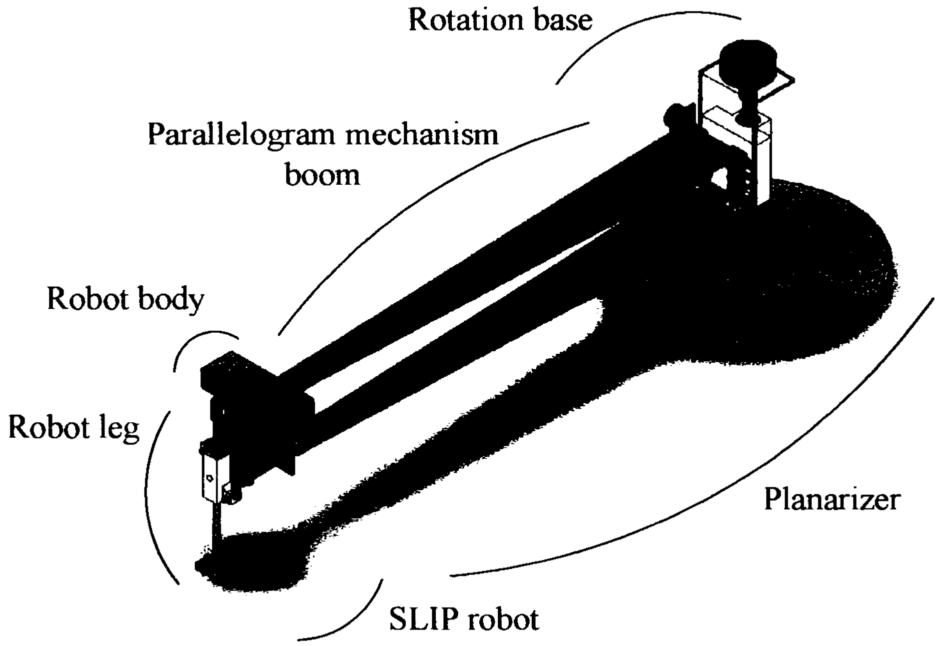

Figure 4.5 Isometric view of the CAD design of the robot and planarizer

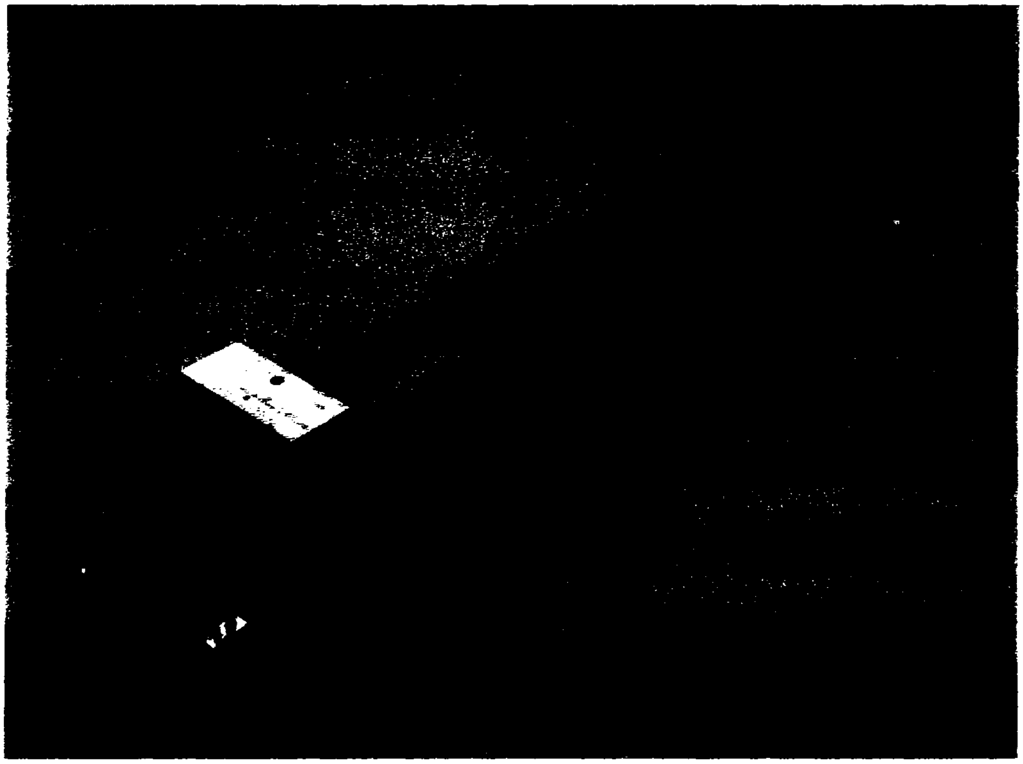

Figure 4.6 Photograph of the actual robot and planarizer

The planarizer consists of a parallelogram mechanism boom that allows vertical translation of z and a rotation base to permit horizontal translation of x. The two beams and four hinges form the parallelogram mechanism. The SLIP robot body is attached to the two beams via hinge joints. The rotating part of the base is connected to the other ends of the two beams via hinge joints, and rotates about the vertical rotation axis rod. The rotation axis rod is vertically fixed to the horizontal-plane base, which is fixed to the level ground.

The surface traced by the boom end on the robot side approximates the sagittal plane, which allows translational motion. On the other hand, the pitch motion of the body is restricted, which allows the assumption that the conceptual COM coincides with the hip joint axis. Note that the actual center of mass (COM) location for the robot body is not located at the hip joint. Nonetheless, since the body cannot rotate in the sagittal plane, it is acceptable to regard the hip joint point as the COM location of the robot body.

The radius of the circular boom motion should be adequately large to regard the constraint to be a plane constraint. The effective boom length L, i.e. the distance between the rotation axis and the leg position, is 0.660 *m* at rest. The distance the robot can travel in one revolution of the boom is $2\pi \times 0.660 = 4.15\,m$, and it takes the robot approximately 5 *s* to travel that distance at a speed of 0.80 *m/s*. The robot hops approximately 14 times in one revolution.

Sensor Mount Positions and Measurements

Four sensors are mounted on the robot and the planarizer. To measure the horizontal position of the robot body, one potentiometer is placed on the rotation axis of the rotation base, shown in Figure 4.7(a). The horizontal position x with respect to the initial condition is calculated from the yaw angle α_{yaw} of the planarizer boom about the rotation axis and the effective boom length L:

$$x = 2\pi L \cdot \frac{\alpha_{yaw}}{360} = \frac{\pi}{180} \cdot L\alpha_{yaw}. \tag{4.1}$$

To measure the vertical position of the robot body, one potentiometer is placed at a hinge joint between the top beam and the rotating part of the rotation base, shown in Figure 4.7(b). The vertical position z from the ground is calculated from the rest leg length r_0, the roll angle α_{roll} of the boom, and the effective boom length L:

$$z = r_0 + L \sin \alpha_{roll}. \tag{4.2}$$

To measure the leg angle γ at the hip joint, one potentiometer is placed on the output axis of the servo, coincident with the hip joint axis.

Finally, to detect ground contact and determine the phase condition, an infrared sensor is mounted on the leg near the toe.

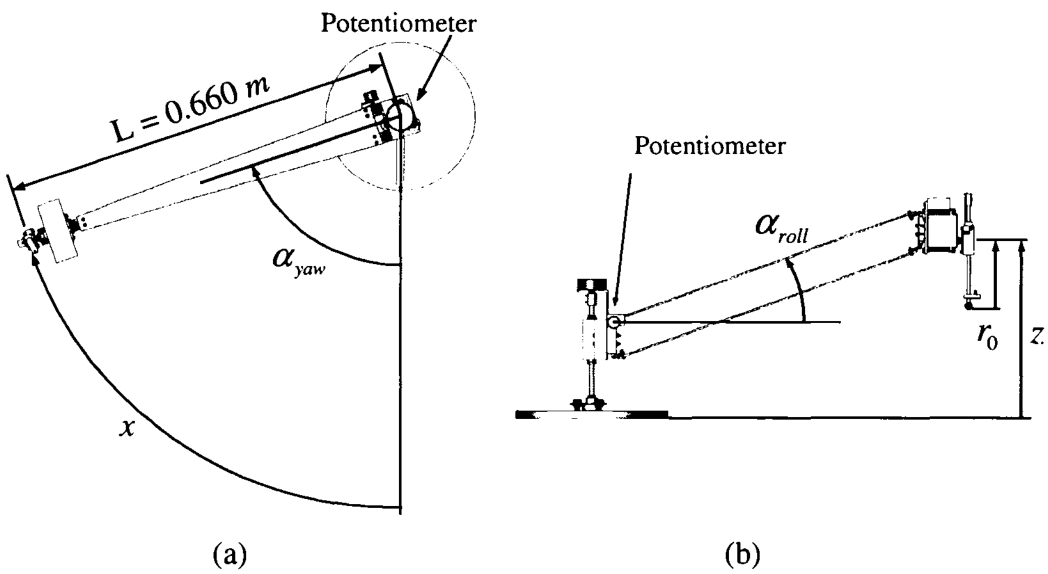

Figure 4.7 (a) Horizontal (top) view and (b) lateral (frontal) view of the robot and planarizer. Yaw and roll angles of the boom are measured to calculate the robot body position in the sagittal plane.

4-3. Computer and Electronic System

This section first describes the structure of the computer system that controls the robot. Then, each of the computer and electronic components for the SLIP robot platform is described.

System Structure

The structure of the computer and electronic system is illustrated in Figure 4.8. Most importantly, two computers are used. One is used as a host machine in order to write code for the control program for the robot. The other is used as a target machine in order to run the compiled code that is uploaded from the host machine and to control the robot in real-time. Microsoft Windows is used for the host computer, while On Time RTOS-32 is used for the target computer. RTOS-32 is a real-time operating system that allows control of the platform in real-time. The robot is tethered to the target computer via an interface card, which operates both D/A and A/D conversions. A control signal is sent from D/A to a motor amplifier, and sensor signals are acquired from A/D.

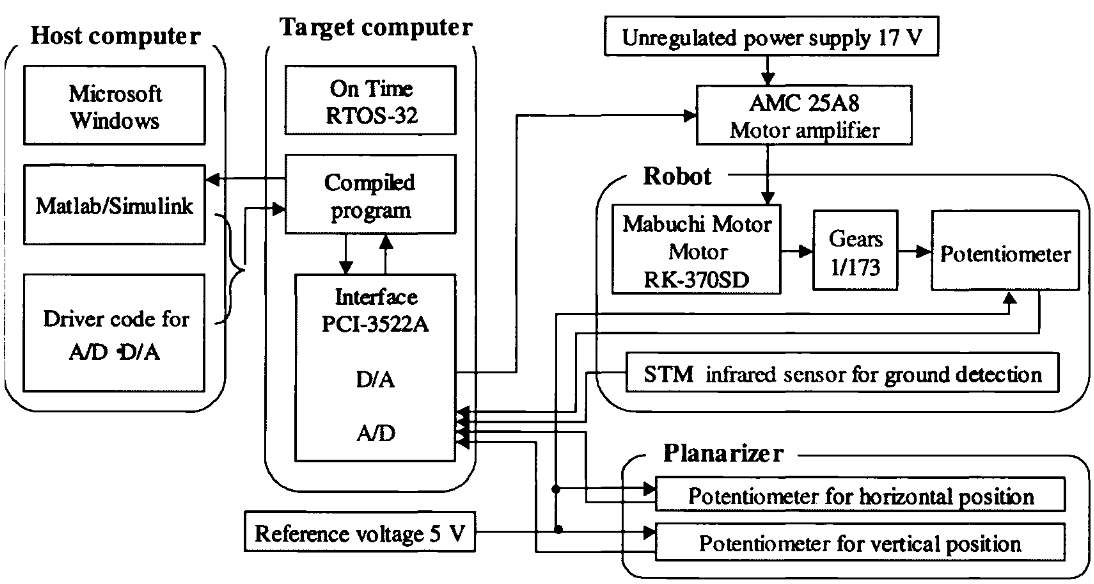

Figure 4.8 Computer and electronic system structure

Interface Card

An interface card is installed in the target computer to output command signals to the motor amplifier as well as to acquire measurement signals. The card used here is a PCI-3523A from Interface Corporation. The board has four D/A terminals for voltage output and eight A/D terminals for voltage data acquisition. The voltage range is ± 10 V, and both D/A and A/D are of 12-bit precision.

The A/D sampling is accomplished through multiplexing, and each of the 8 channels takes $60\,\mu s$ to sample. As a result, an update rate of the entire real-time system cannot be faster than 0.480 ms. Note that the code itself is small in file size, and the control part of the code does not need as much time to execute since the applied control scheme is simple.

Actuator

The use of a DC motor would be most appropriate since it retains the simplicity of the SLIP model and it is compatible with the controller in Chapter 2. An R/C servo set, HS-5735MC from Hitec RCD USA, Inc. shown in Figure 4.9, is used as a hip actuator. The set consists of a DC motor from Mabuchi Motor and four stages of gears with a total gear ratio of 173. The stall torque of the motor is 0.0363 Nm using 8.77 A at 7.2 V. It has a compact dimension of $59 \times 29 \times 52\,mm$, and weighs 146 g.

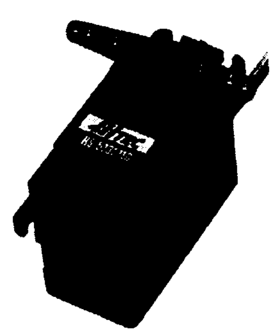

Figure 4.9 Servo set HS-5735MC from Hitec RCD USA, Inc.

Motor Amplifier

A 25A8 brush-type PWM servo amplifier from Advanced Motion Controls, shown in Figure 4.10, is used to supply power to the DC motor. It features a current control mode for control of the motor torque. This amplifier also allows measurement of output current. Available current is $\pm 10\,A$ continuously and 20 A for 2 s. A potentiometer is installed to adjust the current limit for continuous current, which was set to $\pm 5\,A$. For added safety, a limit is also set in the control code that generates the desired current for the motor.

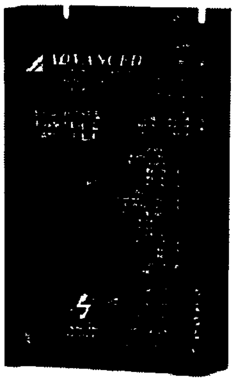

Figure 4.10 Servo amplifier 25A8 from Advanced Motion Controls

Distance Sensor

An infrared distance sensor RL50 from STM, shown in Figure 4.11, is selected as a ground detection sensor. It allows the identification of touchdown / lift-off instants. The sample frequency is 500 *Hz* (i.e. 2 *ms* per sample). The sensor has a diameter of 5 *mm* and a height of 13 *mm*. This small size enables it to be positioned just beside the toe of the robot.

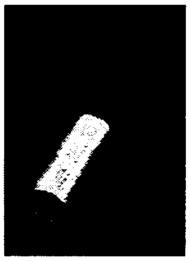

Figure 4.11 RL50 infrared sensor from STM

Rotational Position Sensors

There are a total of three angle sensors on the robot and the planarizer. Potentiometers are used to measure the leg angle, and the roll and yaw angles of the boom. Potentiometers are a suitable choice to avoid complexity of implementation.

A mechanically endless potentiometer N-15 from Piher, shown in Figure 4.12(a), is attached inside the servo casing in order to measure the leg angle at the hip joint axis. Because it is a through-hole mount type potentiometer, a shaft in the hip axis is put through the sensor. It can rotate mechanically a full 360 *deg* and has a measurement range of 340 *deg*. The dimensions of $16\times16\times6$ *mm* allows it to physically fit in the servo casing.

A conductive plastic potentiometer CP-2FK from Midori America Corporation, shown in Figure 4.12(b), is attached on one parallelogram joint of the base-side boom end of the planarizer. The potentiometer rotates with little friction, so that the planarizer does not produce undesirable friction. It can rotate mechanically 360 *deg* and has a measurement range of 340 *deg* similarly to the N-15 from Piher.

A similar conductive plastic potentiometer, WPM 65-20-101 from Waters, is used on top of the rotation axis of the planarizer base. It does not cause much friction either, and it can also rotate mechanically 360 *deg* and has a measurement range of 340 *deg*.

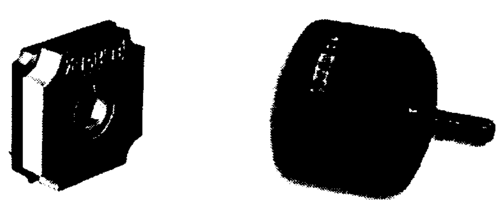

(a) (b)

Figure 4.12 (a) Endless potentiometer N-15 from Piher, (b) Conductive Plastic potentiometer CP-2FK from Midori America Corporation

4-4. Controller Code

This section discusses the controller code used to control the robot, written in Matlab and Simulink [57]. The code includes not only leg motion control but also motor current control and data acquisition. The implementation is done as shown in Figure 4.13, where the shaded area is the hopping controller software. The controller uses the feedback information from the potentiometer for leg angle and the infrared sensor for ground sensing. The information from the two potentiometers on the planarizer is not used in control but logged to analyze the robot's motion off-line. The control update / sensor sampling rate is 1 *ms*. This time has been chosen because the sensor sampling itself takes half a millisecond to run and twice that amount is reasonable for safety.

In Figure 4.13, the symbol γ denotes the leg angle and the symbol i denotes the current. The appropriate desired angle γ_{des} for the state of the robot is chosen. The desired leg angular speed $\dot{\gamma}_{des}$ is set to zero throughout the cycle. The desired motor current i_{des} is generated from the PD controller:

$$\begin{aligned} i_{des} &= \tau_{des}^{Motor} / K_\tau \\ &= (\tau_{des}^{Hip} / RT) / K_\tau \\ &= [K_P(\gamma_{des} - \gamma^{LP1}) + K_D(\dot{\gamma}_{des} - \dot{\gamma})]/(RTK_\tau), \end{aligned} \tag{4.3}$$

where K_τ is the motor torque constant, R is the total gear ratio of four gear stages, and T is the torque transmission ratio. τ_{des}^{Motor} and τ_{des}^{Hip} are the desired motor and hip torques, K_P and K_D are PD gains, and γ^{LP1} is a filtered leg angle. Any desired current over 5 *A* is truncated by a current limiter for the safety of the motor and for smoother leg motion:

$$i_{com} = tran[i_{des}]. \tag{4.4}$$

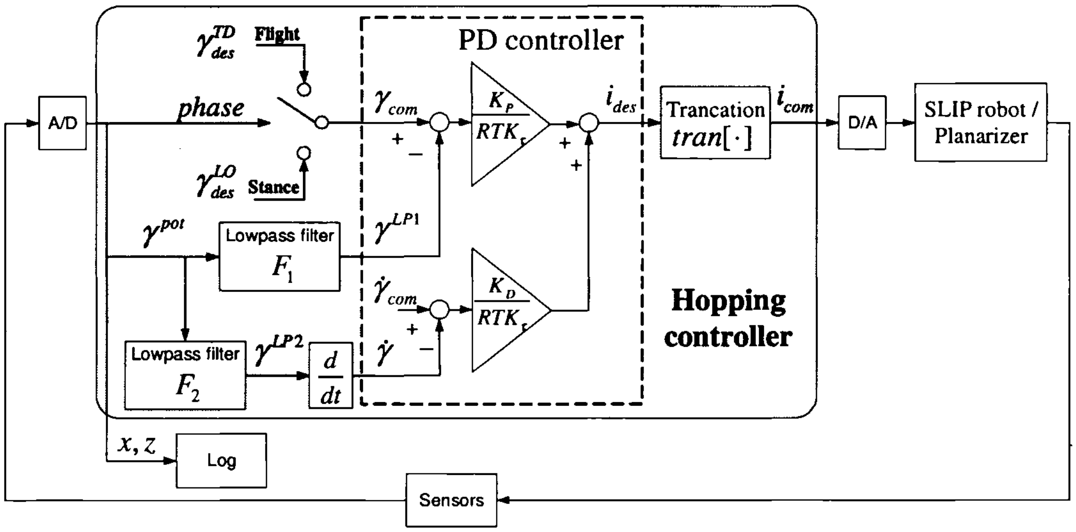

Figure 4.13 Diagram of the controller in the entire system loop

The following 2nd- and 3rd-order lowpass filters are used to remove noise in the potentiometer output γ^{pot}:

$$F_1(s) = \frac{\gamma^{LP1}(s)}{\gamma^{pot}(s)} = \frac{500}{s+500} \cdot \frac{100}{s+100}, \tag{4.5}$$

$$F_2(s) = \frac{\gamma^{LP2}(s)}{\gamma^{pot}(s)} = \frac{250}{s+250} \cdot \left(\frac{60}{s+60}\right)^2. \tag{4.6}$$

The first filter $F_1(s)$ is used on the potentiometer output γ^{pot} to obtain the first filtered angle γ^{LP1}, as shown in Figure 4.13. The second filter $F_2(s)$ is used on the potentiometer output γ^{pot} to obtain the second filtered angle γ^{LP2}. Both filters are intended to smooth the measured potentiometer signal. The second filter $F_2(s)$ is more restrictive, i.e. it has lower break frequencies and a higher order, because its output is later differentiated and therefore must be smoother.

After the PD gains are initially set using Ziegler-Nichols Tuning [75], they are adjusted to create the follow-through / drawdown motion of the leg. The gains used in experimentation are shown in Table 4.1. The P gains here are approximately 20 % lower than those used in the simulation, so that the motor torque τ^{Motor} is restrained. The D gains here are approximately three times higher than those used in the simulation, so that the leg angular speed $\dot{\gamma}$ is moderated. In experimentation, these considerations are necessary so as to avoid divergence of the leg oscillation, which can be caused by potentiometer output noise.

Table 4.1 PD gains in experimentation

Phase	Gain	Symbol	Value	Unit
Stance	P	K_P	28.96	*Nm/deg*
	D	K_D	2.896	*Nms/deg*
Flight	P	K_P	33.78	*Nm/deg*
	D	K_D	2.123	*Nms/deg*

4-5. Chapter Summary

In this chapter, the experimental platform of the SLIP robot was described. First, the mechanical structure of the robot and the boom planarizer system were described. Then, the hardware and software systems were described in detail. This setup is used to obtain the experimental results presented in the next chapter.

Chapter 5. Experimental Results

5-1. Chapter Introduction

This chapter reviews the experimental results obtained when the SLIP robot described in Chapter 4 hops in a plane defined by the planarizer. The first section demonstrates that the running motion is repetitive as desired. The second section validates the leg control and motor performance. The third section analyzes the stability in periodicity at steady state and robustness to changes in initial condition.

In experimentation, the robot successfully produces periodic hopping at steady state and robust hopping, which is consistent with the simulation results in Chapter 3. The results are shown by means of data plots and images obtained from high frame-rate video. Most of the data presented in this chapter is from a single experiment. Results from other experiments are also presented in order to demonstrate robustness.

5-2. Motion in Sagittal Plane

In this section, the running motion in an experiment is shown and compared to the desired motion. The apex height and average forward speed are frequently chosen as indexes of hopping motion. In all the experiments in this thesis, an apex height of

0.170 *m* and an average forward speed of 0.80 *m/s* are the targeted values. Other desired values, such as leg length and bottom height, are also considered, and the resultant hopping motion is discussed from an energy point of view, as well.

High Frame-rate Video

Figure 5.1 shows sequential snapshots from high frame-rate video taken at 250 *frames/s*. The time interval between the snapshots is approximately 30 *ms* and the robot moves towards the left in the pictures as time progresses. The first snapshot shows an apex achieved in the flight phase during steady running, and the last one shows the next apex. The sequence shows that the dynamical state of the robot at the first apex returns to the same state at the second apex so that the gait can be repeated indefinitely.

The description on each snapshot is as follows:

1. Flight apex: the COM is at the highest point in the flight phase. The leg is vertical. The vertical velocity of the COM is zero. Gravitational potential energy is at a maximum.
2. Before touchdown: the body approximately follows a ballistic trajectory. The leg is being protracted to the desired touchdown angle. The vertical downward velocity is increasing. Gravitational potential energy is decreasing.
3. Touchdown: the leg toe just reaches the ground. The spring has not yet started extending.
4. After touchdown: the leg is being retracted. The spring is being extended, which corresponds to a compression of the virtual leg spring. The body is sliding down along the leg shaft. Gravitational energy and kinetic energy is transferred to elastic potential energy of the spring.
5. Around stance bottom: the COM is approximately at the lowest point. The leg is vertical. The vertical velocity of the COM is approximately zero. The stored potential energy in the spring is near the maximum.

6. Before lift-off: the leg is being retracted to the desired lift-off angle. The spring is being shortened, which corresponds to an extension of the virtual leg spring. The body is sliding up along the leg shaft. The elastic potential energy is being transformed to kinetic energy and gravitational energy.
7. Lift-off: the leg toe is still on the ground but is about to take off. The white leg bushing just hits the upper travel stop. The stored elastic potential energy has now been completely released.
8. After lift-off: the body flies up together with the leg shaft, approximately along a ballistic trajectory. The vertical velocity of the COM is decreasing. Gravitational potential energy is increasing. The horizontal velocity of the COM is constant after lift-off.
9. Flight apex: the COM is at the highest point again. The apex height is the same as at the previous apex. The leg is vertical. The vertical velocity of the COM is zero. Gravitational potential energy is at its maximum. This is the initial condition of the next hopping cycle.

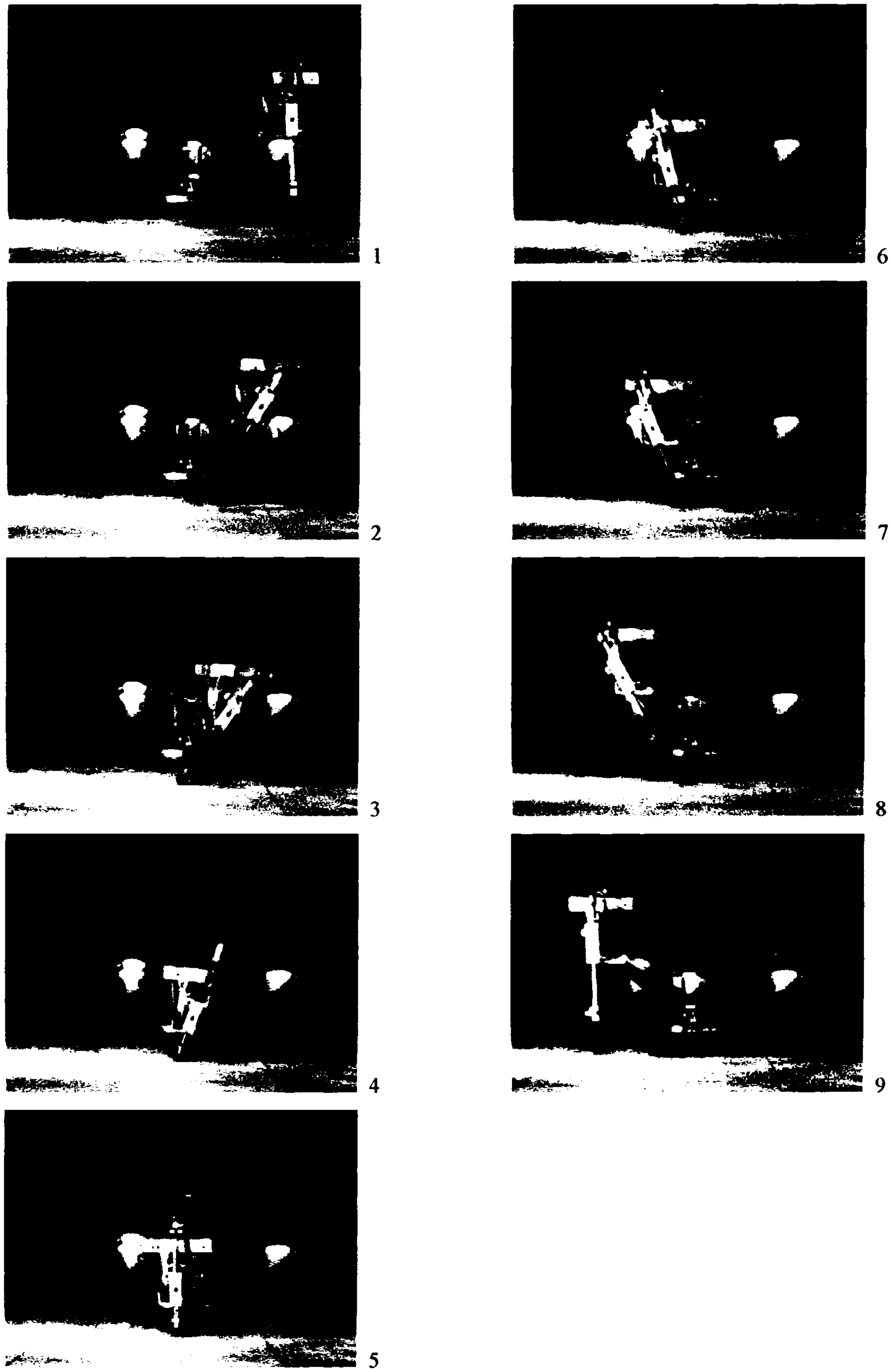

Figure 5.1 High frame-rate snapshots of hopping motion from one apex to the next

Vertical Motion

Figure 5.2 shows the locus of the conceptual COM of the robot body in the sagittal plane. The vertical and horizontal positions are obtained from the potentiometer outputs of the planarizer. The data set is from an experiment with an initial forward speed of –0.58 *m/s*, vertical position of 0.263 *m*, and vertical speed of 0 *m/s*. The path does not exhibit any discontinuities, which means that touchdown events are smooth and that the stance dynamics are smooth and are smoothly connected to the flight dynamics. Even with the initial negative forward speed, the robot converges to the desired height with steady forward motion. This implies that small disturbances would not hinder the robot's forward movement, which will be further demonstrated later in this chapter.

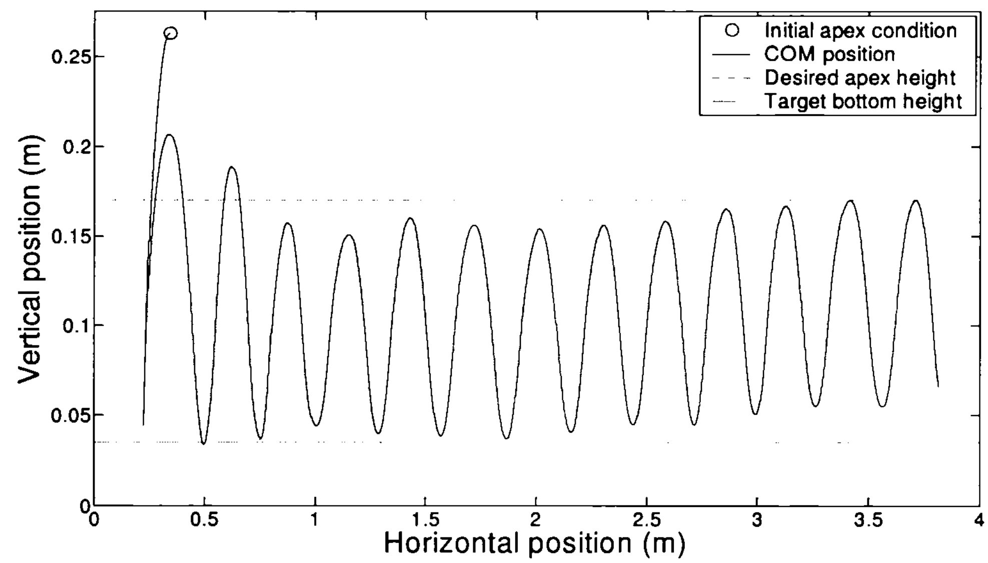

Figure 5.2 Experimental Data: Vertical position vs. horizontal position of the COM with a large initial error to the desired state

Figure 5.3 is a plot of the height of the COM over time. The detected touchdown points are indicated by downward triangles, and the detected lift-off points are denoted by upward triangles. The desired touchdown height z_{des}^{TD} can be calculated using the rest leg length r_0 and the desired touchdown leg angle γ_{des}^{TD}:

$$z_{des}^{TD} = r_0 \cos \gamma_{des}^{TD} = 0.120 \cos 40° = 0.092\, m, \tag{5.1}$$

and similarly, the desired lift-off height z_{des}^{LO} is:

$$z_{des}^{LO} = r_0 \cos \gamma_{des}^{LO} = 0.120 \cos(-25°) = 0.109\, m. \tag{5.2}$$

Following from Eqs. (5.1) and (5.2), it is desirable that the lift-off height is higher than the touchdown height. This is attributed to the appropriate energy distribution discussed in Chapter 2. The result shown in Figure 5.3 is that the lift-off height is always higher than the touchdown height, if the two values in the same cycle are compared. However, the measured values in the plot differ from the desired values, and the measured lift-off height even exceeds the rest leg length of 0.120 *m* at some points. The lead / delay of ground detection is the source of this measurement error, and the sensor hysteresis increases the lift-off sensing error. This error also exists in the plot of leg length presented later.

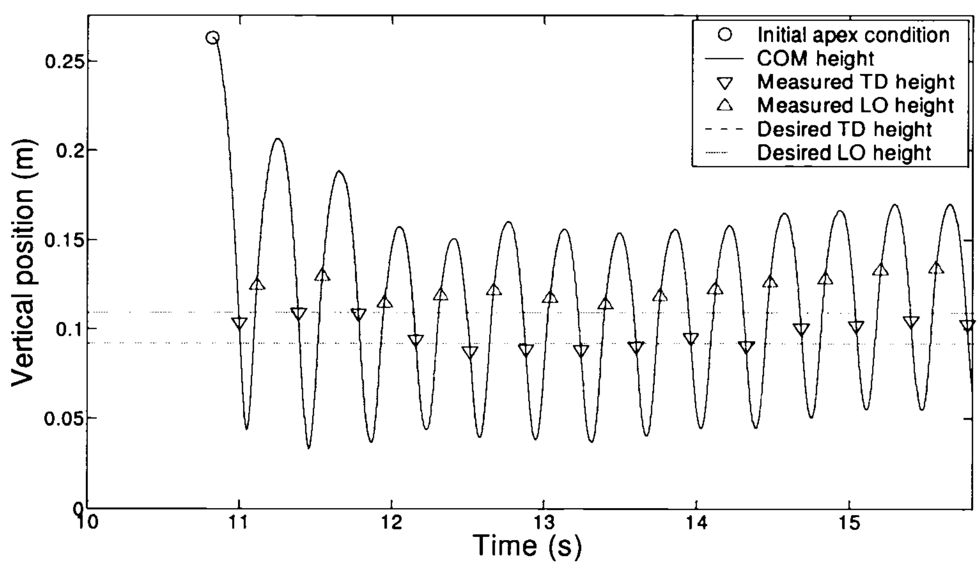

Figure 5.3 Experimental Data: Vertical position of the COM over time

In Figure 5.3 as well as in Figure 5.2, the apex height converges to 0.170 *m*. This value is as determined in Chapter 2. The bottom height (lowest point in stance phase) is approximately 0.055 *m*. This value is higher than the predicted value of 0.035 *m* and lower than the simulation value of 0.061 *m*.

The apex height is 142 % of the rest leg length of 0.120 *m* and the bottom height is 46 % of it. Hence, the total vertical distance that the COM travels over a hopping cycle is roughly twice the rest leg length r_0, since each cycle includes two travels between apex and bottom. The measured average stance duration T_s and flight duration T_f are 0.16 *s* and 0.20 *s*, respectively. The average speed of vertical motion can be calculated by the total vertical distance traveled divided by the time for one hopping cycle:

$$\frac{2\cdot(1.42-0.46)\cdot r_0}{(T_s+T_f)}=\frac{2\cdot(1.42-0.46)\cdot 0.120}{(0.16+0.20)}=0.65\ m/s. \qquad (5.3)$$

This is 81 % of forward speed. This vertical motion may be too large even considering that the leg spring absorbs impact to some degree [25] as mentioned in Chapter 3. The robot should avoid significant impact and vibration, or otherwise it will be prone to failure. In the future, it would be interesting to investigate the design of a hopping robot with less vertical travel.

Horizontal Motion

Figure 5.4 shows a plot of horizontal position versus time. It can be seen that the robot moves forwards smoothly and steadily. This plot becomes approximately linear 1/5 of a second after the start of the motion, which means the robot runs almost at a constant forward speed.

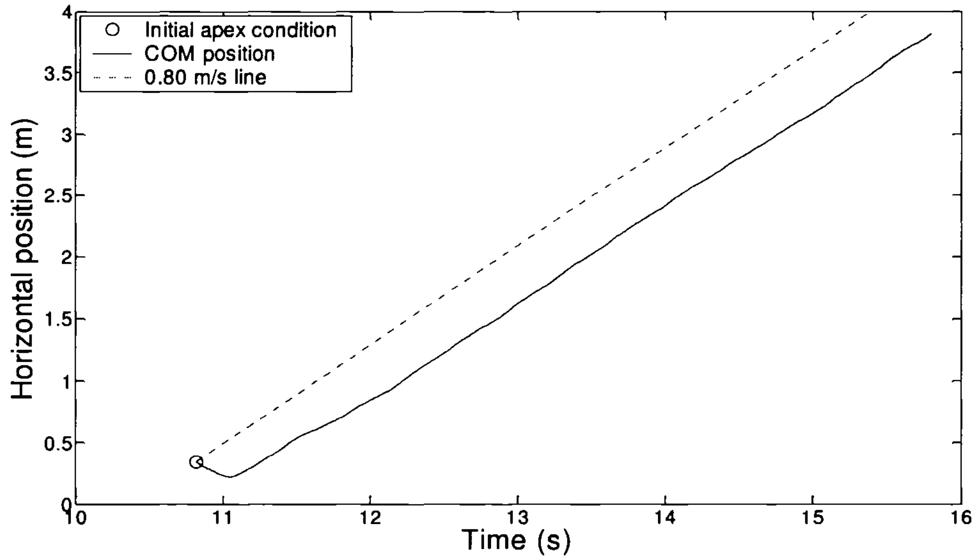

Figure 5.4 Experimental Data: Horizontal position over time

Next, the forward speed is obtained by finite differencing of the horizontal position data. Figure 5.5 is a plot of forward speed versus time. The value of the square wave denotes the measured phase: 0 for stance and 1 for flight. In the stance phase, forward speed first increases and then decreases after mid-stance. The increase in forward speed at the start of the stance phase occurs because the PD controller provides a large retracting torque when the leg angle is far from the final set point, i.e. the desired lift-off angle. As the leg angle approaches the lift-off angle, the PD controller provides a decelerating torque and then reduces the leg rotation rate, which reduces the body's forward speed. In flight, the forward speed curve is almost flat because the body approximately has a ballistic trajectory in the sagittal plane. The curve is not as flat as expected likely due to leg motion and measurement inaccuracy.

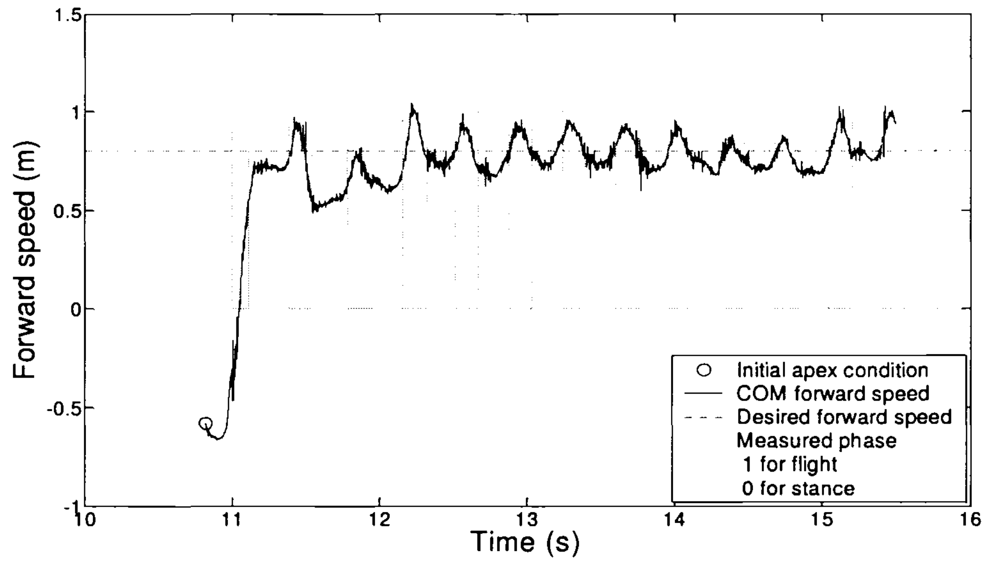

Figure 5.5 Experimental Data: Forward speed over time

Leg Length

The leg length r during the stance phase can be calculated using the leg angle γ and the body height z:

$$r = \frac{z}{\cos\gamma}. \tag{5.4}$$

The leg length in the flight phase is assumed to be constant at 0.120 *m*, neglecting small vibrations, such as spring chattering and impact with the upper travel stop. Therefore, as soon as the phase shifts into the flight phase, the leg length is set to 0.120 *m*.

Figure 5.6 shows the plot of the calculated leg length over time. This result shows that the designed rest leg length r_0 is adequately long since the leg length at each bottom retains a margin longer than 0.025 *m*. This is the physical dimension from the COM to the lowest part of the robot body.

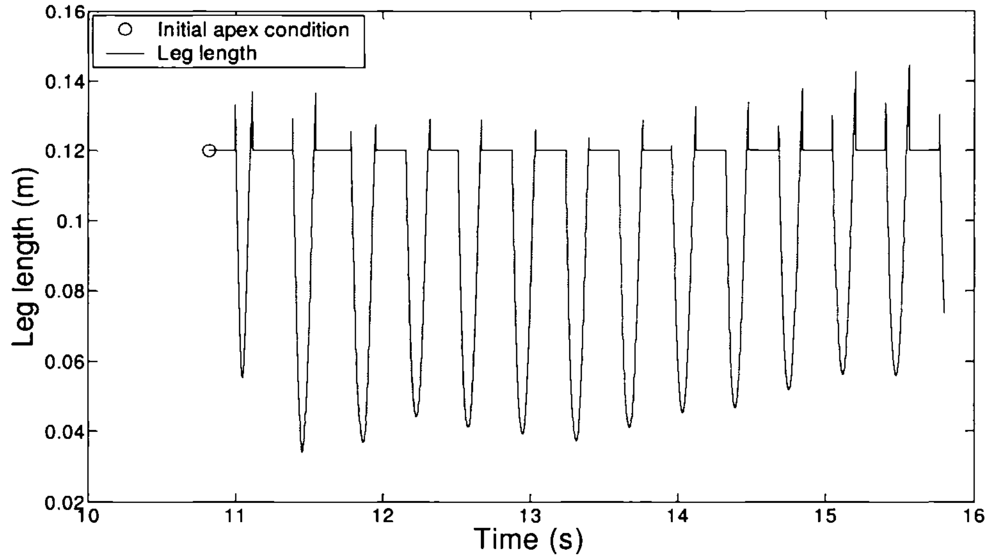

Figure 5.6 Experimental Data: Leg length with error over time

Clearly, the physical leg length between the toe tip and the hip joint can never be longer than 0.120 *m*. Nevertheless, vertical spikes that exceed this value can be seen at the beginning and end of the flight phase. These spikes occur because of the lead of touchdown detection and the delay of lift-off detection. During the time that the body is in flight but the sensor detects ground contact, the calculated value obtained from Eq. (5.4) overestimates the leg length. The width of the spikes indicates the time error of phase detection. Delay from the sensor exists in every cycle, but the robot continues hopping. Therefore, it can be inferred that these time delays are not sufficient to destabilize the motion.

If the spikes are neglected so as to focus on the behavior of the leg length, the shape looks similar to that in vertical hopping described in [16]. This supports the hypothesis used in Chapter 2 that vertical hopping can approximate the vertical motion of planar hopping.

Summary of Motion in Sagittal Plane

The plots of the experimental results related to the sagittal motion of the SLIP robot have been shown and discussed. The following are validated:

- It is observed that the robot runs continuously;
- Apex height is approximately 0.170 *m* as desired;
- Average forward speed is 0.80 *m/s* as desired;
- There are phase detection errors, but they are acceptable;
- Designed leg length is adequately long for this running gait to maintain a safety margin of the prismatic joint travel.

5-3. Motor Performance and Control

It is essential that the actuator behave as desired. Not only controller design flaws but also motor performance deficiencies can directly cause locomotion failure [27], [19], [59], [60]. For the SLIP robot, both aspects must perform satisfactorily in order to protract the leg to the desired touchdown angle and to inject energy into the system so that the SLIP can stabilize itself. In this section, the leg control and the motor performance are empirically validated. The data presented here are from the same experiment as for the preceding motion analysis.

Commanded and Actual Leg Angles

Figure 5.7 is a plot of commanded and actual leg angles. The commanded leg angles are 40 *deg* for the flight phase and –25 *deg* for the stance phase. These are the angles desired only at the end of each phase, but they are commanded throughout the phase. Following the leg control in Figure 2.9 in Chapter 2, it is desired that the actual trajectory forms a curve like a 3^{rd}-order spline from –25 *deg* to 40 *deg* during the flight phase and then an almost linear line back to –25 *deg* during the stance phase. The actual leg angle path here progresses smoothly even though the commanded angles are discontinuous. This is due to the PD control with low P gains, and it supports the use of PD control in both the stance and flight phases.

The touchdown angle of 40 *deg* results in a leg angle trajectory with repetitive cycles. This confirms that the touchdown angle is appropriate to maintain the repetitive motion of both the body and the leg. Thus, one of the two leg motion requirements for the self-stability is satisfied. The other requirement of angular speed at touchdown is also satisfied since the angular speed does not destabilize the following stance motion. The angle trajectory is inclined at touchdown and it smoothens the connection to the following stance trajectory.

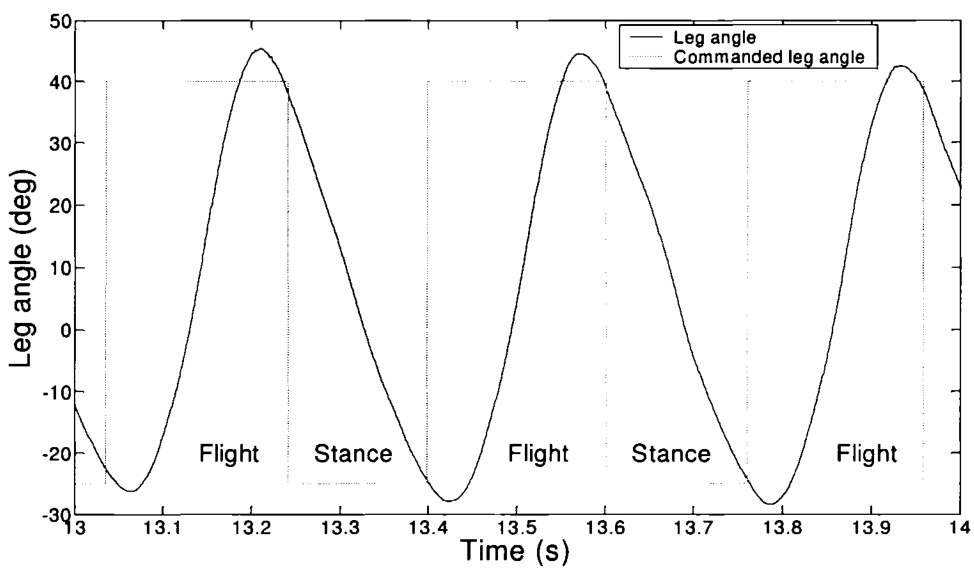

Figure 5.7 Experimental Data: Commanded and actual leg angles vs. time

Desired, Commanded, and Actual Current

The DC motor is controlled via current regulation of the motor amplifier. Current, which is proportional to the motor torque, is the desired output from PD control. The PD gains were tuned in such a way that the maximum desired current would be about 7 *A*, which is truncated to 5 *A* by the current limiter discussed previously. This results in a saturation of the desired current at large errors, but the errors are not accumulated since neither the stance- or flight-phase controllers include an integral term. Hence, limiting the desired current in such a way is acceptable.

In Figure 5.8, as a result of the current limit, the desired current is saturated and the commanded current is constant at the beginning of each phase. Throughout each phase, the actual current tracks the commanded current well.

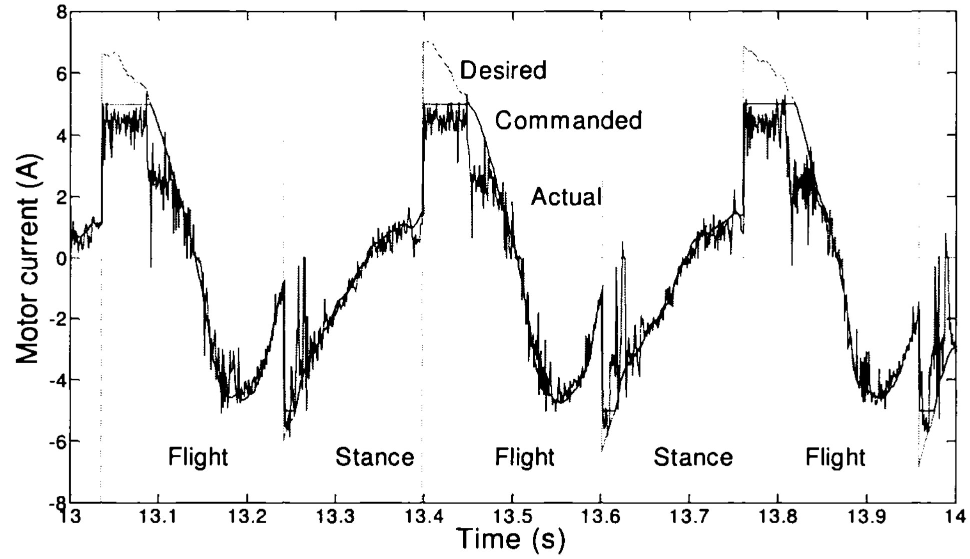

Figure 5.8 Experimental Data: Desired, commanded, and actual current vs. time. Positive current protracts the leg in flight and negative current retracts it in stance.

The required power in flight is higher than in stance. This is consistent with the result of the hip motor energy cost of Monopod I in Gregorio's *et al* work [77]. The dynamics of a Spring-loaded Inverted Pendulum (SLIP) with a passive hip joint results in a natural sweeping of the leg during stance if the leg has an appropriate angle at touchdown and if friction and impact are not severe. Therefore, it consumes more power to swing the leg forwards in the flight phase than it does to sweep the leg backwards in the stance phase.

Torque-speed Curve

The actual torque-speed curve can be compared to the maximum performance capabilities of the motor. The controller should not command any higher current than the motor can handle. Not only would it cause too much heating but also the controller will not work as desired due to saturation. For instance, model-based control will not work in some legged robot applications with low-performance servo systems [27], [19].

The actual motor torque is approximately estimated using the formula:

$$\tau_{estimatd}^{Motor} = K_\tau \cdot i_{actual}, \tag{5.5}$$

where $\tau_{estimated}^{Motor}$ is the estimated motor output torque, K_τ is the torque constant of the motor, and i_{actual} is the actual current provided to the motor from the motor amplifier.

The motor speed is obtained by multiplying the measured hip speed by the total gear ratio of the 4-stage gears from the motor axis to the hip axis:

$$\omega_{estimated} = \dot{\gamma} \cdot R, \tag{5.6}$$

where $\omega_{estimated}$ is the estimated motor speed, $\dot{\gamma}$ is the measured hip speed obtained by differentiating the measured potentiometer angle γ^{pot}, and R is the total gear ratio.

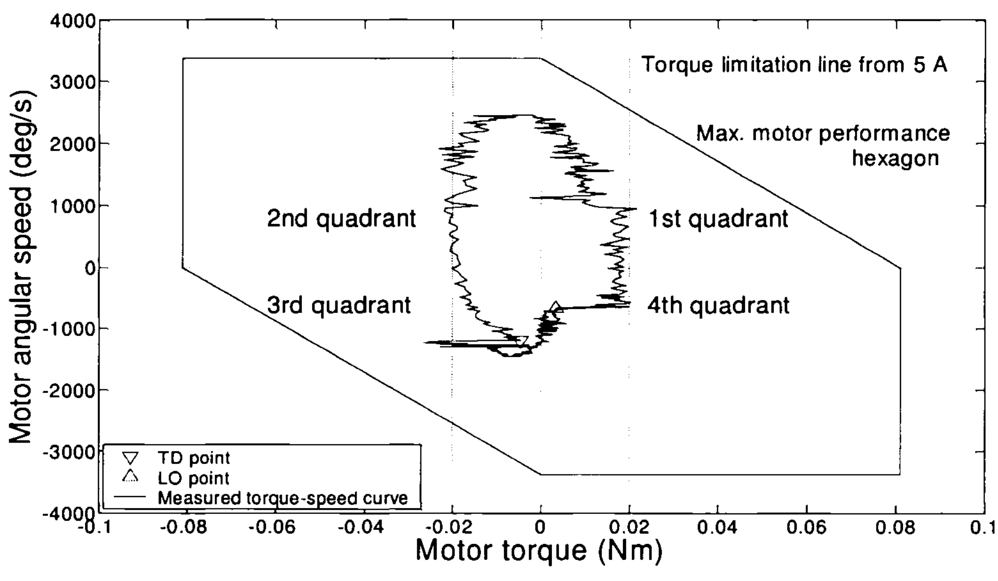

Figure 5.9 Experimental Data: Torque-speed curve of the motor

The hexagon in Figure 5.9 represents the maximum performance of the motor alone without gears [79]. The two vertical dashed lines at $\pm 0.021 Nm$ show the maximum possible torque with the 5-A limitation. The plotted curve shows the actual torque-speed curve of the motor for one hopping cycle between 13.0 s and 13.4 s. The motion proceeds counterclockwise on this curve. In the first quadrant, a positive torque protracts the leg and produces a positive speed. In the second quadrant, a negative torque is imposed to the leg, but the leg still has a positive speed. In the third quadrant, the negative torque draws down the leg and produces a negative speed. The leg touches down, and the negative torque retracts the leg. In the fourth quadrant, a positive torque decelerates the leg, but it still has a negative speed. The leg takes off and has the follow-through motion until the curve enters into the first quadrant when the positive torque produces a positive speed.

Figure 5.9 shows that the actual torque-speed curve stays within the maximum motor capabilities and mostly stays within the domain created by the hexagon and the vertical lines. Thus, the motor specifications accommodate the required performance to achieve the commanded leg angles at the end of each phase, and the current limit is high enough.

The actual curve protrudes beyond the current limit at the lower-left part in the third quadrant. This can be explained using Figure 5.8. The actual current in the flight phase does not much exceed 5 A. However, the current in the stance phase more frequently descends below $-5A$. This occurs right after touchdown because of the touchdown impact with an abrupt load torque from the ground force. Consequently, more current is drawn. Nonetheless, the impact is not so large that it can disturb the control of the motor and the smoothness of the leg angle trajectory in Figure 5.7.

Summary of motor performance and control

In this section, the data plots related to motor performance and motor control have been shown and discussed. The findings of the experiment are:

- Leg motion is well controlled as desired, since the simple controller is adequate exploiting the tracking characteristics of PD control with low P gains;
- Actual motor current tracks the commanded trajectory well;

- Servo system specifications accommodate the required performance, and the current limit is high enough.

5-4. Stability Analysis

The same methods as for the simulation are adopted in order to determine the stability of the robot's hopping behavior. The figures in this section show phase plots and transition plots. These plots can be used to examine a 2D cross-section of the state space of a dynamical system and to show convergence of dynamical behavior.

One simple criterion to assess the periodic stability of the running motion is the convergence to a limit cycle in the phase plot of the COM height z. Again, the data presented here are from the same experiment as for the preceding motion analysis and motor performance analysis. Since the produced IC is similar to the IC of the simulation, the simulation and experimental results can be compared. Phase plots of the leg angle γ and the leg length r are also constructed from the same set of experimental data, because the periodic and symmetric motion of the COM is associated with that of the leg.

A transition plot is also obtained from the same experiment to view the robustness to the IC. Nine IC's other than the IC used thus far are also tested in order to reveal how robust the system is. All of the convergence transitions of the 10 IC's are plotted in one figure to estimate the region of attraction for the experimental system and compare it to that for the simulation model. Unfortunately, the region of attraction obtained from the experiments is not complete since the IC's are produced by releasing the robot in the air by hand, and it is difficult to produce as diverse IC's as the 2115 IC's in the simulation results.

Phase Plot of Vertical Position

Figure 5.10 is the phase plot of the vertical position z of the COM. Time progresses along the curve as the state evolves clockwise. The left side of the curve represents the stance-phase motion. The right side of the curve represents the flight-phase ballistic motion. From the stance phase in the first cycle, the curve proceeds inwards. The combination of the two dynamical characteristics creates a closed orbit and results in a retracing of the same course over many cycles so that a limit cycle is generated. The shape of the limit cycle is symmetric with respect to the line for zero vertical speed as the ideal SLIP model has been shown to be [16], [47], [48], [49], [45]. This plot shows close correspondence to Figure 3.6 obtained with the simulation.

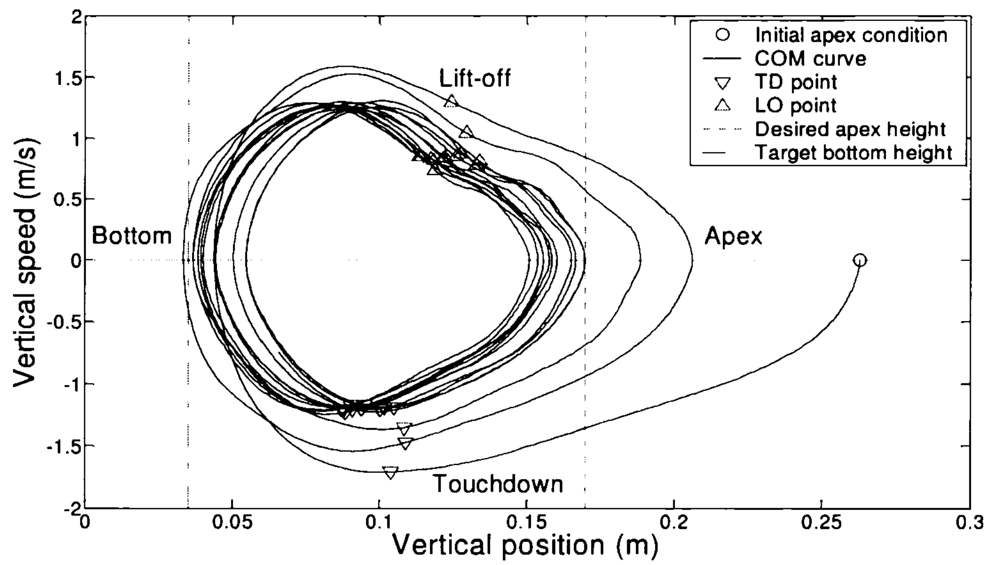

Figure 5.10 Experimental Data: Phase plot of the vertical position of the COM

For the flight phase, the plot exhibits the energy transfer in vertical motion between kinetic energy and gravitational potential energy. From apex to touchdown, gravitational potential energy is transferred to kinetic energy because the magnitude of the vertical speed increases as the height decreases. Similarly, from lift-off to apex, kinetic energy is transferred to gravitational potential energy. This is all the energy transfer in the flight phase since it is assumed that the forward speed in flight is constant and that the spring deflection in flight is kept at the pre-deflection length. On the other hand, this plot does not clearly describe the entire energy transfer in the stance phase, since it does not show information on forward motion or spring deflection.

The stance-phase curve is smooth as predicted from simulation. Sweeping the leg via a hip torque imparts an appropriate amount of mechanical energy to the robot, in order to compensate dissipation. Otherwise, the hopping cycle would not be maintained, i.e. the closed orbit would collapse.

The flight-phase curve has a deviation from the ideal ballistic curve as in the simulation. After lift-off, there is a slight notch. Since it does not occur right at lift-off, it is not due to the impact on which the upper leg bushing hits the end of travel as Koechling indicated [64]. It is presumably caused by swinging the mass / inertia of the leg, which is neglected in the simulation model, as McMordie proposed [65]. A more complicated model than the SLIP model would capture fine details.

In Appendix D, a plot of the vertical speed versus vertical position evolving with time is shown using the same data set. The convergence with respect to time is seen in the plot. An equivalent plot resulting from the simulation is also shown in the appendix.

Phase Plot of Leg Angle

Figure 5.11 is the phase plot of the leg angle γ, i.e. a plot of leg angular speed versus leg angle. The leg angular speed $\dot{\gamma}$ is obtained by differentiating the measured potentiometer leg angle γ^{pot}. Once again, time progresses clockwise around this curve. The upper part of the curve is associated with the flight phase, and the lower part of the curve represents the stance phase. The combination of the two converges to a closed orbit without discontinuity and eventually constitutes a limit cycle.

Touchdown occurs at the lower-right corner, and lift-off is at the lower-left corner. The measured states at touchdown and lift-off are shown as downward triangle markers (∇) and upward triangle markers (Δ), respectively. An inspection of the triangle marker locations reveals that the commanded leg angles ($\gamma_{com}^{Fl} = \gamma_{des}^{TD} = 40 deg$, $\gamma_{com}^{St} = \gamma_{des}^{LO} = -25 deg$) are achieved at the end of each phase but the commanded leg angular speeds ($\dot{\gamma}_{com}^{Fl} = \dot{\gamma}_{com}^{St} = 0$) are not. The measured angular speeds are roughly −300 *deg/s* at touchdown and −250 *deg/s* at lift-off. These negative values are the results of the drawdown motion and follow-through motion, respectively, and are truly desired to achieve using the hopping controller, as described in Chapter 2.

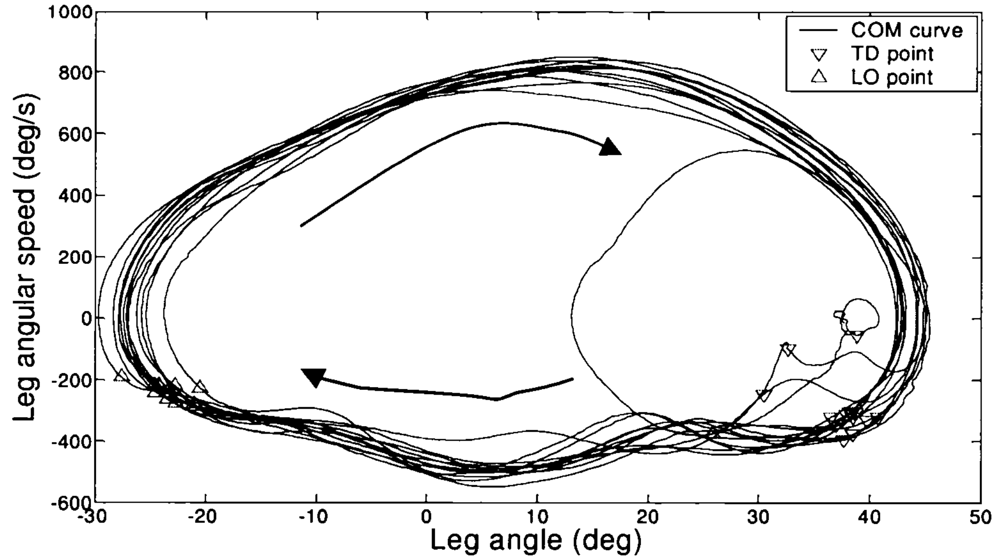

Figure 5.11 Experimental Data: Phase plot of the leg angle

The stance-phase curve is roughly symmetric with respect to a leg angle of approximately 8 *deg*. This angle corresponds to the shift amount of the sweep mid-angle ϕ_{mid} (7.5 *deg*) mentioned in Chapter 2. Thus, the angle shift is successful and does not destroy the symmetry property of the SLIP stance motion.

Phase Plot of Leg Length

Figure 5.12 shows the phase plot of the leg length r. In the stance phase, the leg length r is obtained from Eq. (5.4). In the flight phase, the leg length is assumed to be constant at 0.120 *m*. The time derivative $\dot{r}$ is obtained by differentiating the measured leg length. The leg length error shown in Figure 5.6, which exceeds the rest leg length of 0.120 m, is removed here before differentiating.

Throughout the flight phase, the state $(r, \dot{r})$ stays at the point $(0.120, 0)$, denoted by a cross marker ($\times$), since the leg length r remains constant at the rest length and its time derivative $\dot{r}$ is zero. The data shown in the figure, except the flight-phase point, corresponds to the stance phase. Time progresses clockwise along the curve.

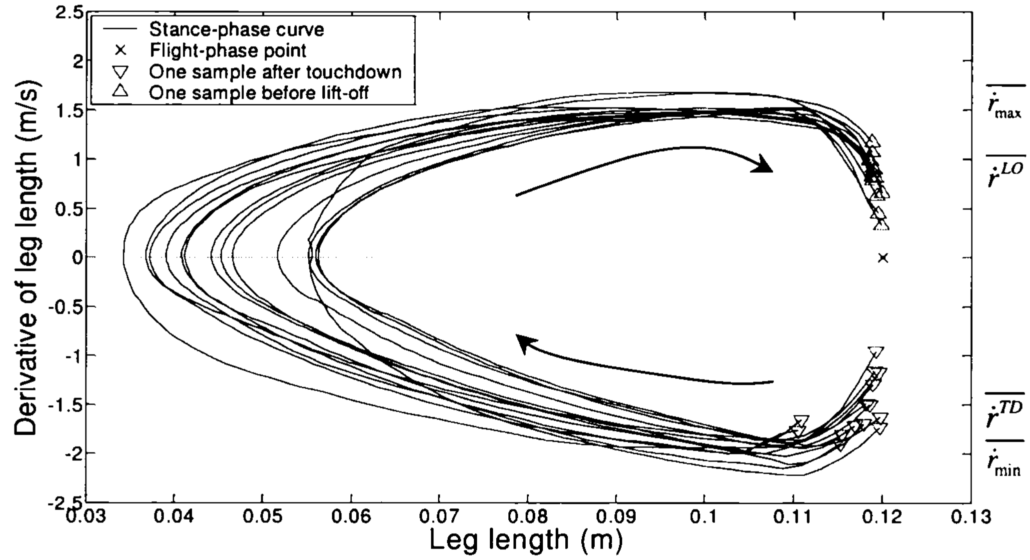

Figure 5.12 Experimental Data: Phase plot of the leg length

Triangle markers are placed at the initial and final points of the stance-phase curve, i.e. at the measured states one sample time after touchdown and one sample time before lift-off. In addition, these points and the flight-phase point are not connected. This is because the abrupt change of leg length motion (r, $\dot{r}$) can be highlighted by the jumps between the flight-phase point and the triangle markers.

From the flight-phase point to the downward triangle markers, the leg length r decreases slightly while the time derivative $\dot{r}$ abruptly decreases from the flight-phase point. The derivative starts with a large negative speed due to the impact speed at touchdown. As well, large jumps occur from the upward triangles to the flight-phase point. The reason of this jump is that, at lift-off, the upper leg bushing hits the mechanical stop of the prismatic joint travel so that the leg length r is instantly stopped at 0.120 m and the speed of the leg length extension jumps quickly to zero.

The shape of the stance-phase curve is roughly symmetric with respect to the line $\dot{r} = 0$, but not precisely so. The average of the time derivative at touchdown over 14 cycles, $\overline{\dot{r}^{TD}}$, is -1.54 *m/s* while the average of the time derivative at lift-off, $\overline{\dot{r}^{LO}}$, is 0.81 *m/s*. The lower part of the stance-phase curve is more dilated, and the average of the minimum derivative, $\overline{\dot{r}_{\min}}$, -1.99 *m/s*. On the other hand, the upper part of the stance-phase curve is flatter, and the average of the maximum derivative, $\overline{\dot{r}_{max}}$, is 1.52 *m/s*. As a result, the asymmetric and forced sweep slightly deforms the shape of the phase plot, although it does not completely ruin the symmetry of leg length motion.

Transition Plots

Figure 5.13 shows a transition plot of the forward speed $\dot{x}$ and the vertical position z at the apex, i.e. a sequence of the apex state vectors $\underline{x}_n^{Apex} = (z_n^{Apex}, \dot{x}_n^{Apex})$, for the same experimental data set. The IC in this experiment is a forward speed of –0.58 *m/s*, a vertical position of 0.263 *m*, and a vertical speed of 0 *m/s* while the IC in the simulation is a forward speed of –0.60 *m/s*, a vertical position of 0.260 *m*, and a vertical speed of 0 *m/s*. Considering this difference, it seems that the experimental result here matches well with the simulation result in Figure 3.7.

The IC point of the apex state, $\underline{x}_1^{Apex}$, is attracted to the neighborhood of the desired point of the average forward speed of 0.80 *m/s* and the apex vertical position of 0.170 *m* even though the IC is distant from it. Again, note that the apex forward speed $\dot{x}_n^{Apex}$ is expected to be lower than the target average speed of 0.80 *m/s* as explained in Chapter 3.

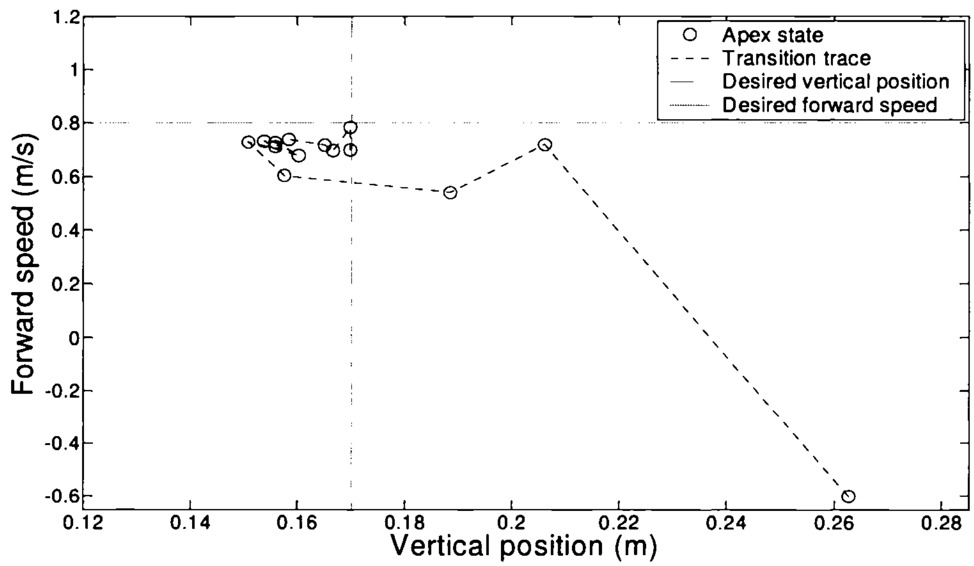

Figure 5.13 Experimental Data: Transition plot of the apex state for the IC of $\dot{x} = -0.58$ *m/s*, $z = 0.263$ *m* and $\dot{z} = 0$ *m/s*, considered as the state with a large error to the desired state

Figure 5.14 shows the plot of 10 convergence transitions obtained using the data set used thus far and nine additional data sets. Due to the small number of IC's tested, no boundary of the domain of all the converging IC's can be determined. In other words, the region of attraction for the experimental SLIP robot cannot be presented here.

All the 10 IC's are attracted to the area described for the simulation in Chapter 3, i.e. the area inside the apex height range from 0.169 *m* to 0.173 *m* and the apex forward speed range from 0.61 *m/s* to 0.65 *m/s*. This indicates a large region of attraction as in the simulation result of Figure 3.8. It demonstrates that a few of the IC points (IC's 1, 3 and 6) near the edge of the region of attraction found in the simulation also converge. Thus, these experiments to some degree verify the validity of the SLIP-based design and the robustness of the gait periodicity.

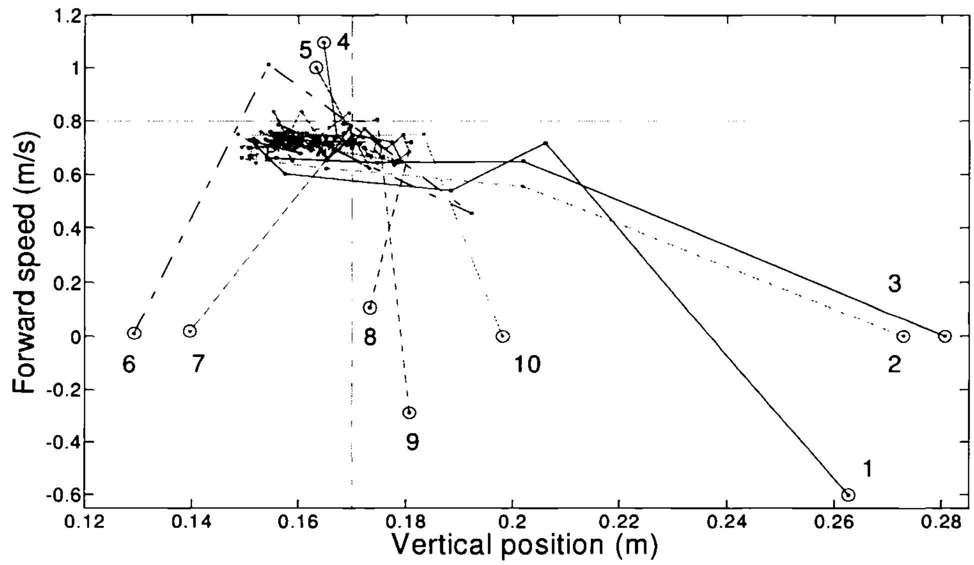

Figure 5.14 Experimental Data: Convergence transitions for 10 IC's. The transition plot for IC 1 is the same as in Figure 5.13.

If reasonably small disturbances are imposed to the robot, it will restore itself to a steady condition within several hopping cycles. The magnitude of disturbance must be small enough that the robot's condition stays within the region of attraction after the disturbance. If some object hits the robot during its flight or the leg toe lands on a stair step with a different height, the following apex condition can be regarded as its initial condition to restart its hopping. Since the SLIP robot without adaptive control has been found robust, the SLIP model might also be applicable to uneven surfaces even though it is originally intended for level surfaces.

Summary of Stability Analysis

Based on the results shown and discussed in this section, it can be concluded that:

- Phase plots show that steady periodic motion is achieved in terms of COM height, leg angle, and leg length;
- The symmetry property is preserved in terms of COM height, stance leg angle, and leg length even though an asymmetric gait is used; only the flight-phase curve of leg angle phase plot was not symmetric;
- Phase transitions in terms of COM height and leg angle are smooth, but not in terms of leg length;
- Hopping is robust within a certain range of apex conditions for height and forward speed.

Several aspects of the stability of the SLIP robot are demonstrated and analyzed, as seen in the simulation.

5-5. Chapter Summary

In this chapter, experimental data were presented and discussed. First, steady sagittal motion of the SLIP robot was observed. Next, it was confirmed that the servo performance fulfills the control requirements. Lastly, in stability analysis, steady periodicity and robustness of the hopping motion were confirmed. Despite the use of an asymmetric leg sweep, nearly symmetric motion was observed. The experimental results match well with the simulation results presented in Chapter 3.

Chapter 6. Conclusions

6-1. Conclusions

This thesis presented the development of a hopping robot, whose design is based on the SLIP (Spring-loaded Inverted Pendulum) model, and experimental validation of the SLIP model using the SLIP-model-based robot. For the last three decades, this model has been used as a reduced-order model of running animals and robots for the purpose of dynamical analysis and control [10], [11], [12], [13], [14], [16], [9], [45], but not directly used as a design of robots.

To the author's best knowledge, this thesis work is the first research demonstrating the design, simulation, mechanical implementation, and experimental results of a robot that mimics the features of the SLIP model. The research presented here proceeded in the following order. The essential three parameters (mass, leg spring stiffness, and rest leg length) of a SLIP-model-based robot were determined in Chapter 2. A simple controller for the robot was created in Chapter 2 and resulted in periodic and robust running in the simulation presented in Chapter 3. Next, in Chapter 4, the SLIP-model-based robot was constructed as a planar one-legged hopping robot with one actuator at the hip joint. Using a gait with one set of mechanical and control parameters, periodic and robust running was experimentally demonstrated in Chapter 5.

From these developments and experiments, the following objectives were achieved:

- Feasibility study of a robot based on the SLIP model
- Design and construction of a SLIP robot with one actuator
- Experimental implementation of a simple controller for one running gait
- Demonstration of a running speed of average 0.80 *m/s* (6.7 leg lengths per second)
- Experimental validation of the SLIP model for one running gait
- Demonstration of periodicity and robustness of one running gait.

From these developments and experiments, the following conclusions may be drawn:

- The SLIP model with three parameters (mass, leg spring stiffness, and rest leg length) and one actuator was validated in simulation and by experiment as a running model in the sagittal plane. No more complex mechanisms and dynamics model are required for dynamically stable running on level surfaces.
- A simple controller for the SLIP-model-based robot resulted in periodic running in simulation and experimentation. The only necessary energy input was to replace losses and the only balancing control necessary is to correct for the touchdown angle and angular speed of the leg. This is consistent with the self-stability property of the SLIP model [9], [22], [23], [24].
- Simulations and experiments indicated a large region of attraction for a robust running gait. This leads to a hypothesis that the SLIP model might be applicable to the running motion of animals and humans on uneven surfaces as well as on level surfaces.

These conclusions are new findings and are the contributions of the thesis.

6-2. Future Work

Although the results outlined in 6-1 above were intended accomplishments, the tested conditions in running speed and touchdown leg angle are not general. It would be valuable to accomplish similar results for different conditions in order to more generally confirm the validity of the SLIP model. Thus, future work such as speed control to accomplish different desired speeds and height control to accomplish different desired heights is suggested. For speed control, Raibert's forward speed controller [16] might directly be applied. If so, only the online measurement of stance duration would need to be added to the proposed hopping controller. For height control, a novel control method might be required if an additional prismatic actuator is not an option.

The implementation of a SLIP robot in 3D without the support of a constraint mechanism is also suggested. In order to achieve this, it would be imperative to consider the following two issues. First, a single-leg hopping in 3D requires another hip actuator, and the leg motion must be controlled in the lateral plane as well as in the sagittal plane. A control challenge is that controllers for the two planes must share a single prismatic joint, i.e. the control input from the controller for one plane will not only affect the leg motion in that plane but also in the other plane. The prismatic joint motion resulting from the two controllers is coupled, and the desired motions for the two planes will most likely conflict. This requires more than a simple superposition of another identical hopping controller for the lateral motion. Second, the center of mass (COM) of the body must actually be located at the hip joint in order to exploit the results presented in the thesis. Otherwise, a control method to deal with pitching dynamics must be realized. This would be involved since the actuators would need to control the body orientation in addition to the leg angles. These two matters would require a major refinement of the mechanical structure design and control scheme.

Lastly, in order to understand the nonlinear and hybrid characteristics of the SLIP robot, rigorous mathematical analysis is suggested. The differential equations for the COM dynamics in the stance phase are analytically non-integrable [83], and the solution remains an open problem [80]. In Chapter 3, thus, numerical integration was used to solve the differential equations, where there was no loss in rigor but also no expansion in the use of solutions. An analytical solution would allow not only extended stability analysis but also mechanical parameter and hopping controller designs using mathematical theories and physical principles without utilizing heuristic equations from biomechanical experimentation.

Bibliography

[1] D. Wettergreen, C. Thorpe, and W.L. Whittaker, "Exploring Mount Erebus by Walking Robot," Proceedings of the Conference on Intelligent Autonomous Systems, pp. 72-81, 1993.

[2] R. R. Murphy, "Rescue Robots at the World Trade Center," Journal of the Japan Society of Mechanical Engineers, special issue on Disaster Response Robotics, vol. 102, no. 1019, pp. 794-802, 2003.

[3] K. Tani, K. Ikeda, T. Yano, S. Kajita, and O. Matsumoto, "The Concept of Model Free Robotics for Robots to act in Uncertain Environments," Proceedings of the IEEE/Tsukuba International Workshop on Advanced Robotics, pp. 85-90, Tsukuba, Japan, 1993.

[4] S. Kajita and K. Tani, "Adaptive gait control of a biped robot based on realtime sensing of the ground," Proceedings of the IEEE International Conference on Robotics and Automation, pp. 570-577, 1996.

[5] J. Hodgins, "Legged Robots on Rough Terrain: Experiments in Adjusting Step Length," Ph.D dissertation, Department of Computer Science, Carnegie Mellon University, Pittsburgh, Pennsylvania, USA, 1989.

[6] S. Kajita and K. Tani, "Study of dynamic biped locomotion on rugged terrain - Derivation and application of the linear inverted pendulum mode -," Proceedings of the IEEE International Conference on Robotics and Automation, pp.1405-1411, 1991.

[7] P. V. Nagy, W. L. Whittaker, and S. Desa, "A Walking Prescription for Statically-Stable Walkers Based on Walker/Terrain Interaction," Proceedings of the IEEE International Conference on Robotics and Automation, pp. 149-156, 1992.

[8] Pearson Education, Inc., "Speed of Animals," Fact Monster, http://www.factmonster.com/ipka/A0004737.html , 2000.

[9] R. J. Full and D. E. Koditschek, "Templates and anchors: Neuromechanical hypotheses of legged locomotion on land," Journal of Experimental Biology, vol. 202, pp. 3325-3332, 1999.

[10] R. M. Alexander and A. Vernon, "Mechanics of hopping by kangaroos (Macropodidae)," Journal of Zoology, London, vol. 177, pp. 265-303, 1975.

[11] R. M. Alexander and A. S. Jayes. "Vertical movement in walking and running," Journal of Zoology, London, vol. 185, pp. 27-40, 1978.

[12] R. Blickhan, "The spring-mass model for running and hopping," Journal of Biomechanics, vol. 22, pp. 1217-1227, 1989.

[13] R. Blickhan and R. J. Full. "Similarity in multilegged locomotion: Bouncing like a monopode," Journal of Comparative Physiology, vol. 173, pp. 509-517, 1993.

[14] C. T. Farley, J. Glasheen, and T. A. McMahon, "Running springs: Speed and animal size," Journal of Experimental Biology, vol. 185, pp. 71-86, 1993.

[15] I. Poulakakis, "On the Passive Dynamics of Quadrupedal Running," M.Eng. thesis, Department of Mechanical Engineering, McGill University, Montreal, Canada, 2002.

[16] M. H. Raibert, "Legged Robots That Balance," MIT Press, Cambrige, MA, USA, 1986.

[17] H. B. Brown and G. Z. Zeglin, "The Bow Leg Hopping Robot," Proceedings of the IEEE International Conference on Robotics and Automation, pp. 781-786, Leuven, Belgium, 1998.

[18] U. Saranli, W. J. Schwind, and D. E. Koditschek, "Toward the Control of a Multi-Jointed Monoped Runner," Proceedings of the IEEE International Conference on Robotics and Automation, pp. 2676-2682, 1998.

[19] I. Poulakakis, J. A. Smith and M. Buehler, "Experimentally Validated Bounding Models for the Sout II Quadrupedal Robot," Proceedings of the IEEE International Conference on Robotics and Automation, vol. 3, pp. 2595- 2600, 2004.

[20] S. Kajita, T. Nagasaki, K. Yokoi, K. Kaneko, and K. Tanie, "Running pattern generation for a humanoid robot," Proceedings of IEEE International Conference on Robotics and Automation, vol. 3, pp. 2755 – 2761, 2002.

[21] K. Harbick and G. S. Sukhatme, "Controlling Hopping Height of a Pneumatic Monopod," Proceedings of the IEEE International Conference on Robotics and Automation, pp. 3998-4003, 2002.

[22] H. Geyer, A. Seyfarth and R. Blickhan, “Natural Dynamics of Spring-Like Running: Emergence of Selfstability,” Proceedings of the International Conference on Climbing and Walking Robots, pp. 87-92, Paris, France, 2002.

[23] R. P. Ringrose, “Self–stabilizing running,” Ph.D. dissertation, Massachusetts Institute of Technology, Cambridge, MA, USA, 1997.

[24] T. M. Kubow and R. J. Full, “The Role of the Mechanical System in Control: A Hypothesis of Self-stabilization in Hexapedal Runners,” Philosophical Transaction of the Royal Society of London Series B – Biological Sciences, vol. 354, no. 1385, pp. 854-862, 1999.

[25] T. McGeer, “Passive Bipedal Running”, Technical Report, CSS–IS TR 89-02, Centre For Systems Science, Simon Fraser University, Burnaby, BC, Canada, 1989.

[26] M. Ahmadi, “Stable Control of a One-Legged Robot Exploiting Passive Dynamics,” Ph.D. dissertation, Department of Mechanical Engineering, McGill University, Montreal, QC, Canada, 1998.

[27] S. Talebi, I. Poulakakis, E. Papadopoulos, and M. Buehler, "Quadruped Robot Running with a Bounding Gait," Experimental Robotics VII, Lecture Notes in Control and Information Sciences 271, Daniela Rus and Sanjiv Singh, editors, pp. 281-289, Springer-Verlag, 2001.

[28] U. Saranli, M. Buehler, and D. E. Koditschek, "RHex: A Simple and Highly Mobile Hexapod Robot," International Journal of Robotics Research, vol. 20, no. 7, pp. 616-631, July 2001.

[29] M. Buehler, U. Saranli, and D. E. Koditschek (McGill University, The Regents of the University of Michigan), Single Actuator Per Leg Robotic Hexapod, US Patent, No. 6,481,513 B2, USA, 2002.

[30] C. Steeves, “Design and Behavioural Control of a Dynamic Quadruped with Active Wheels,” M.Eng. thesis, Department of Mechanical Engineering, McGill University, Montreal, QC, Canada, 2003.

[31] T. A. McMahon and G. C. Cheng, “The mechanics of running: How does stiffness couple with speed?” Journal of Biomechanics, vol. 23, pp. 65-78, 1990.

[32] M. H. Raibert, H. B. Brown, Jr., M. Chepponis, J. Hodgins, J. Koechling, D. Dustman, W. K. Brennan, D. S. Barrett, C. M. Thompson, J. D. Hebert, W. Lee, and L. Borvansky, "Dynamically Stable Legged Locomotion (September 1985-September 1989)," AI Technical Report 1179, Massachusetts Institute of Technology, MA, USA, 1989.

[33] E. T. Whittaker and G. N. Watson, "A Course of Modern Analysis," Cambridge Unversity Press, London, UK, 1902, reprinted 1973.

[34] S. Kajita, "Dynamic control of a biped in linear inverted pendulum mode," Mechanical Engineering Laboratory Report No. 171, Mechanical Engineering Laboratory, Tsukuba, Japan, 1996, In Japanese.

[35] J. D. Weingarten, G. A. D. Lopes, M. Buehler, R. E. Groff, and D. E. Koditschek, "Automated Gait Adaptation for Legged Robots," Proceedings of the IEEE International Conference on Robotics and Automation, vol. 3, pp. 2153-2158, New Orleans, LA, USA, 2004.

[36] I. Poulakakis, J. A. Smith, and M. Buehler, "On the Dynamics of Bounding and Extensions Towards the Half-Bound and the Gallop Gaits", Online Proceedings of the International Symposium on Adaptive Motion of Animals and Machines, http://www.kimura.is.uec.ac.jp/amam2003/, Kyoto, Japan, 2003.

[37] D. Campbell and M. Buehler, "Preliminary Bounding Experiments in a Dynamic Hexapod," In Bruno Siciliano and Paolo Dario, editors, Experimental Robotics VIII, pp. 612-621, Springer-Verlag, 2003.

[38] M. H. Raibert, H. B. Brown, Jr., M. Chepponis, E. Hastings, S. S. Murthy, and F. C. Wimberly, "Dynamically Stable Legged Locomotion--Second Annual Report," CMU-RI-TR-83-1, Robotics Institute, Carnegie-Mellon University, 1983.

[39] P. Gregorio, M. Ahmadi, and M. Buehler, "Experiments with an Electrically Actuated Planar Hopping Robot," In T. Yoshikawa and F. Miyazaki, editors, Experimental Robotics III, Lecture Notes in Control and Information Sciences 200, pp. 269-281, Springer Verlag, 1994.

[40] M. Ahmadi and M. Buehler, "Stable Control of a Simulated One-Legged Running Robot with Hip and Leg Compliance," IEEE Transactions on Robotics and Automation, vol. 13, no. 1, pp. 96-104, 1997.

[41] H. B. Brown and G. Z. Zeglin, "The Bow Leg Hopping Robot," Proceedings of the IEEE International Conference on Robotics and Automation, pp. 781-786, Leuven, Belgium, 1998.

[42] K. Harbick and G. S. Sukhatme, "Speed Control of a Pneumatic Monopod using a Neural Network," Techical Report IRIS-02-413, Institute for Robotics and Intelligent Systems, University of Southern California, 2002.

[43] J. Koechling and M. H. Raibert, "How fast can a legged robot run?" In Symposium in Robotics, DSC-Vol.11, K. Youcef-Toumi, H. Kazerooni (eds.), American Society of Mechanical Engineers, New York, NY, USA, 1988.

[44] M. D. Berkemeier and K. V. Desai, "Control of hopping height in legged robots using a neural-mechanical approach," Proceedings of the IEEE International Conference on Robotics and Automation, pp. 1695-1701, 1998.

[45] R. Altendorfer, D. E. Koditschek, and P. Holmes, "Towards a Factored Analysis of Legged Locomotion Models," Proceedings of the IEEE International Conference on Robotics and Automation, pp. 37-44, 2003.

[46] E. D. Sontag, "A remark on the converging-input converging-state property," IEEE Transactions on Automatic Control, vol. 48, no. 2, pp. 313-314, 2003.

[47] J. P. Ostrowski and J. W. Burdick, "The Control of Mechanical Systems with Symmetries and Nonholonomic Constraints," Proceedings of the IEEE Conference on Decision and Control, 1995.

[48] J. P. Ostrowski and J. W. Burdick, "Controllability Tests for Mechanical Systems with Constraints and Symmetries," Journal of Applied Mathematics and Computer Science, vol. 17, no. 7, pp. 683-701, 1998.

[49] M. H. Raibert, "Running with symmetry," International Journal of Robotics Research, vol. 5, pp. 3-19, 1986.

[50] A. Ruina, "The symmetry of some of the simple non-holonomic examples precludes asymptotic stability," Talk slides

http://www.tam.cornell.edu/%7Eruina/hplab/nonholonomics_papers.html.

[51] A. van der Schaft and H. Schumacher, “An Introduction to Hybrid Dynamical Systems,” Lecture Notes in Control and Information Sciences 251, Springer-Verlag, 2000.

[52] A. V. Savkin and R. J. Evans, “Hybrid Dynamical Systems: Controller and Sensor Switching Problems,” Birkhauser, Boston, 2002

[53] H. Ye, A. N. Michel, and L. Hou, “Stability Theory for Hybrid Dynamical Systems,” IEEE Transactions on Automatic Control, vol. 43, no. 4, pp.461-474, 1998.

[54] M. Zefran and J. W. Burdick, "Design of switching controllers for systems with changing dynamics," Proceedings of the IEEE Conference on Decision and Control, pp. 2113-2118, 1998.

[55] M. Zefran and J. W. Burdick, “Stabilization of Systems with Changing Dynamics by Means of Switching,” Proceedings of the IEEE International Conference on Robotics and Automation, pp. 1090-1095, 1998.

[56] E. Klavins, H. Komsuoglu, R. J. Full, and D. E. Koditschek, "The Role of Reflexes Versus Central Pattern Generators in Dynamical Legged Locomotion", in J. Ayers and J. Davis editors, Neurotechnology for Biomimetic Robots, MIT Press, 2001.

[57] The MathWorks, Inc., “Matlab ver. 6.5 and Simulink ver. 4.0,” http://www.mathworks.com/, Natick, MA, 2003.

[58] T. W. B. Kibble and F. H. Berkshire, “Classical Mechanics,” 4^{th} ed., Addison Wesley, 1997.

[59] R. Suarez, J. Alvarez, and J. Alvarez, “Regions of Attraction of Closed-Loop Linear Systems with Saturated Linear Feedback,” Journal of Mathematical Systems, Estimation, and Control, vol. 5, no. 4, pp. 1-22, Birkhauser-Boston, 1995.

[60] J-Y. Favez, B. Srinivasan, Ph. Mullhaupt, and D. Bonvin, “Condition for Bifurcation of the Region of Attraction in Linear Planar Systems with Saturated Linear Feedback,” Proceedings of the IEEE Conference on Decision and Control, pp. 3918-3923, Las Vegas, Nevada, USA, 2002.

[61] H. Michalska, M. Ahmadi, and M. Buehler, "Vertical Motion Control of a Hopping Robot," Proceedings of the IEEE International Conference on Robotics and Automation, pp. 2712-2717, Minneapolis, MN, USA, 1996.

[62] W. J. Schwind and D. E. Koditschek, "Control of Forward Velocity for a Simplified Planar Hopping Robot," Proceedings of the IEEE International Conference on Robotics and Automation, Vol. 1, pp. 691-696, 1995.

[63] J. Guckenheimer and P. Holmes, "Nonlinear Oscillations, Dynamical Systems and Bifurcations of Vector Fields," Springer-Verlag, 1983.

[64] J. Koechling, "Gait as Mechanical Oscillation", chapter in Dynamically Stable Legged Locomotion, Robotics Institute Technical Report CMU-LL-4-1985, Carnegie Mellon University, Pittsburgh, 1985.

[65] D. McMordie, "Towards pronking with a hexapod robot," M. Eng. thesis, Department of Electrical and Computer Engineering, McGill University, Montreal, QC, Canada, 2002.

[66] Z. Li and J. He, "An Energy Perturbation Approach to Limit Cycle Analysis in Legged Locomotion Systems", Proceedings of the IEEE International Conference on Robotics and Automation, pp. 1989 - 1994, 1990.

[67] I. A. Hiskens, "Stability of hybrid system limit cycles: Application to the compass gait biped robot", Proceedings of the IEEE Conference on Decision and Control, pp. 774-779, Orlando, FL, 2001.

[68] T. S. Parker and L. O. Chua, "Practical Numerical Algorithms for Chaotic Systems," Springer-Verlag, New York, NY, 1989.

[69] R. Seydel, "Practical Bifurcation and Stability Analysis," Springer-Verlag, New York, 2nd ed., 1994.

[70] H. K. Khalil, "Nonlinear Systems," 2nd ed., Prentice Hall, 1996.

[71] Y. Kuznetsov, "Elements of Applied Bifurcation Theory," 2nd ed., Springer-Verlag, 1998.

[72] N. B. Tufillaro, J. Reilly, and T. Abbott, "An experimental approach to nonlinear dynamics and chaos," Addison-Wesley, 1992.

[73] D. E. Koditschek and M. Buehler, "Analysis of a Simplified Hopping Robot", The International Journal of Robotics Research, vol. 10, no. 6, pp.587 – 605, 1991.

[74] S. H. Hyon and T. Mita, "Development of a biologically inspired hopping robot - Kenken," Proceedings of the IEEE International Conference on Robotics and Automation, vol. 4 , pp. 3984 – 3991, 2002.

[75] G. F. Franklin, J. D. Powell, and A. Emami-Naeini, "Feedback Control of Dynamic Systems," 4th ed., Prentice Hall, 2002.

[76] C. M. Thompson and M. H. Raibert, "Passive dynamic running," International Symposium of Experimental Robotics V, Hayward and O. Khatib eds., Springer-Verlag, New York, 1989.

[77] P. Gregorio, M. Ahmadi, and M. Buehler, "Design, Control, and Energetics of an Electrically Actuated Legged Robot," IEEE Transactions on Systems, Man, and Cybernetics, vol. 27B, no. 4, pp. 626-634, 1997.

[78] T. Villa, T. Kam, R. K. Brayton, and A. L. Sangiovanni-Vincentelli, "Synthesis of Finite State Machine: Logic Optimization", Kluwer Academic Publishers, 1997.

[79] Mabuchi Motor Co., Ltd., Product Catalog, 2002.

[80] H. Geyer, A. Seyfarth, and R. Blickhan, "Spring-mass running: simple approximate solution and application to gait stability," Journal of Theoretical Biology, vol. 232, no. 3, pp. 315-328, 2004.

[81] W. J. Schwind and D. E. Koditschek, "Approximating the stance map of a 2-DOF monoped runner," Journal of Nonlinear Science, Vol. 10, pp. 533-568, 2000.

[82] R. M. Ghigliazza, R. Altendorfer, P. Holmes, D. E. Koditschek, "A simply stabilized running model," SIAM Journal of Applied Dynamical Systems, vol. 2, no. 2, pp. 187-218, Society for Industrial and Applied Mathematics, Philadelphia, PA, USA, 2003.

[83] E. T. Whittaker, "A treatise on the analytical dynamics of particles and rigid bodies," 4th ed., Cambridge University Press, London, UK, 1937.

Appendices

Appendix A. Dimension-less Forward Speed

The target forward speed of 0.80 *m/s* might not be the maximum value the robot could achieve. However, the target forward speed is kept at 0.80 *m/s* in this work, and other speeds could be investigated in future work. It would be necessary to use different PD control gains for different desired forward speeds, making the analysis more complicated.

For reference, Table A.1 shows approximate leg lengths, speeds, and dimension-less speeds of the machines that have been used to study the control of legged locomotion. Data is presented for the McGill RHex (tripod gait) [35], the McGill Scout II [36], the RHex (bounding gait) [37], the MIT Planar one-leg hopper [38], the MIT Monopod [32], the McGill Monopod I [39], the McGill Monopod II [40], the CMU Bow leg hopper [41], and the USC Pneumatic monopod [42]. The rest are from [43]. Note that only the MIT Planar Biped, the RHex with an optimized tripod gait and the Pneumatic monopod have been explicitly designed for high speed.

The speed of 0.80 *m/s* is itself relatively high compared to past robots. If *dimension-less speed* [44], [45], the speed divided by the leg length, is considered, the robot's dimension-less forward speed of 6.7 *leg length/s* is very high. It is the fastest in terms of dimension-less speed compared to well-known one-legged robots in Table A.1, and comparable to the fastest biped, the MIT Planar Biped of 7.0 $1/s$ [43]. A bipedal robot generally can be much faster than a one-legged robot with the same leg system because it can propel itself more frequently with the same motion of each leg.

Even compared to the values of animals in Table 2.3, the SLIP robot is fast. Interestingly, the same kind of leaping locomotion in red kangaroos gives similar dimension-less speeds.

Table A.1 Approximate leg lengths, speeds, and dimension-less speeds of legged robots

# of legs	**Machine**	**Researcher**	**Leg length**	**Forward speed**	**Dimension-less speed**
			m	*m/s*	*1/s*
6	OSU Hexapod	McGhee	0.8	0.3	0.4
	USSR Hexapod	Gurfinkle	0.35	0.1	0.3
	SSA Hexapod	Sutherland	1.0	0.14	0.14
	ODEX	Odetics	1.3	0.5	0.4
	ASV	Waldron	1.90	2.2	1.2
	RHex (tripod gait)	Buehler and Koditschek	0.17	2.7	15.9
4	PV II	Hirose	0.87	0.5	1.1
	Quadruped	Raibert	0.66	3.0	4.5
	Scout II	Poulakakis	0.31	1.3	4.2
	RHex (bounding gait)	Campbell	0.17	1.5	8.8
2	WL10-RD	Kato	0.96	0.23	0.2
	Biper-3	Miura	0.20	0.02	0.1
	Meg-2	Funabashi	0.48	0.5	1.0
	Kenkyaku	Furusho	0.72	0.8	1.1
	Planar Biped	Koechling	0.844	5.9	7.0
1	Planar one-leg hopper	Raibert	0.50	1.2	2.4
	Monopod	Raibert	0.74	2.3	3.1
	Monopod I	Gregorio	0.70	1.2	1.7
	Monopod II	Ahmadi	0.70	2.0	2.8
	Bow leg hopper	Brown	0.25	1.0	4.0
	Pneumatic monopod	Harbick	0.285	1.8	6.3
	SLIP robot	**Sato**	**0.120**	**0.80**	**6.7**

Appendix B. Derivation of Equations of Motion

Figure 3.1 shows the dynamics model for the two phases with mechanical parameters and state variables. Based on the model, the equations of motion for the SLIP model / robot are derived.

Flight Phase Model

The system in the flight phase is assumed to have no energy dissipation. The Lagrange equation for such a system is

$$\frac{d}{dt}\left(\frac{\partial L}{\partial \dot{q}_i}\right)-\frac{\partial L}{\partial q_i}=F_i, \tag{B.1}$$

where L is the Lagrangian, q is the general coordinate, and F is the sum of the applied external forces/torques in the coordinate. The general coordinates for the flight phase model are selected to be

$$q_i = x, z, \gamma \quad (i=1,2,3). \tag{B.2}$$

The moment of inertia of the body is not considered since the body is a point mass. The mass of the leg is assumed to be negligible. The kinetic energy T is

$$T=\frac{1}{2}m(\dot{x}^2+\dot{z}^2)+\frac{1}{2}J_{leg}\dot{\gamma}^2. \tag{B.3}$$

The elastic potential energy for the pretension is not considered. The potential energy U is

$$U = mgz. \tag{B.4}$$

Therefore, the Lagrangian L is

$$
\begin{aligned}
L &= T - U \\
&= \frac{1}{2} m(\dot{x}^2 + \dot{z}^2) + \frac{1}{2} J_{leg} \dot{\gamma}^2 - mgz.
\end{aligned}
\tag{B.5}
$$

For $q_1 = x$,

$$
\begin{aligned}
&\frac{\partial L}{\partial \dot{q}_1} = m\dot{x}, \\
&\frac{d}{dt}\left(\frac{\partial L}{\partial \dot{q}_1}\right) = m\ddot{x}, \\
&\frac{\partial L}{\partial q_1} = 0, \\
&F_1 = 0.
\end{aligned}
\tag{B.6}
$$

The Lagrange equation becomes

$$
m\ddot{x} = 0 \tag{B.7}
$$

or

$$
\ddot{x} = 0. \tag{B.8}
$$

For $q_2 = z$,

$$
\begin{aligned}
&\frac{\partial L}{\partial \dot{q}_2} = m\dot{z}, \\
&\frac{d}{dt}\left(\frac{\partial L}{\partial \dot{q}_2}\right) = m\ddot{z}, \\
&\frac{\partial L}{\partial q_2} = -mg, \\
&F_2 = 0.
\end{aligned}
\tag{B.9}
$$

The Lagrange equation becomes

$$
m\ddot{z} = -mg \tag{B.10}
$$

or

$$\ddot{z} = -g \, . \tag{B.11}$$

For $q_3 = \gamma$,

$$\begin{aligned} &\frac{\partial L}{\partial \dot{q}_3} = J_{leg}\dot{\gamma}, \\ &\frac{d}{dt}\left(\frac{\partial L}{\partial \dot{q}_3}\right) = J_{leg}\ddot{\gamma}, \\ &\frac{\partial L}{\partial q_3} = 0, \\ &F_3 = \tau^{Hip} . \end{aligned} \tag{B.12}$$

The Lagrange equation becomes

$$J_{leg}\ddot{\gamma} = \tau^{Hip} \tag{B.13}$$

or

$$\ddot{\gamma} = \frac{\tau^{Hip}}{J_{leg}} . \tag{B.14}$$

As in Eqs. (B.8), (B.11), and (B.14), thus, three equations of motion for the flight phase model are obtained:

$$\begin{aligned} &\ddot{x} = 0, \\ &\ddot{z} = -g, \\ &\ddot{\gamma} = \frac{\tau^{Hip}}{J_{leg}} . \end{aligned} \tag{B.15}$$

Stance Phase Model

Energy losses are taken into consideration for the stance phase. The Lagrange equation with the dissipation term is

$$\frac{d}{dt}\left(\frac{\partial L}{\partial \dot{q}_i}\right)-\frac{\partial L}{\partial q_i}+\frac{\partial D}{\partial \dot{q}_i}=F_i, \tag{B.16}$$

where L is the Lagrangian, q is the general coordinate, D is the dissipated energy, and F is the sum of the applied external forces/torques in the coordinate. The general coordinates for the stance phase model are selected to be

$$q_i = r, \gamma \quad (i=1,2). \tag{B.17}$$

It is assumed that the moment of inertia of the leg is negligible this time as well as the mass of the leg. The kinetic energy T is

$$T=\frac{1}{2}m(\dot{r}^2+(r\dot{\gamma})^2). \tag{B.18}$$

The potential energy U is

$$U = mgr\cos\gamma+\frac{1}{2}k(r_0+\delta_{pre}-r)^2. \tag{B.19}$$

The Lagrangian L is

$$\begin{aligned} L &= T-U \\ &= \frac{1}{2}m(\dot{r}^2+(r\dot{\gamma})^2)-mgr\cos\gamma-\frac{1}{2}k(r_0+\delta_{pre}-r)^2. \end{aligned} \tag{B.20}$$

It is assumed that the impact, dry frication, and viscous damping of the system are represented by one damping term of the prismatic joint. Then, the dissipation energy D is

$$D=\frac{1}{2}b\dot{r}^2. \tag{B.21}$$

For $q_1 = r$,

$$
\begin{aligned}
&\frac{\partial L}{\partial \dot{q}_1} = m\dot{r}, \\
&\frac{d}{dt}\left(\frac{\partial L}{\partial \dot{q}_1}\right) = m\ddot{r}, \\
&\frac{\partial L}{\partial q_1} = mr\dot{\gamma}^2 - mg\cos\gamma + k(r_0 + \delta_{pre} - r), \\
&\frac{\partial D}{\partial \dot{q}_1} = b\dot{r}, \\
&F_1 = 0.
\end{aligned} \tag{B.22}
$$

The Lagrange equation becomes

$$
m\ddot{r} - mr\dot{\gamma}^2 + mg\cos\gamma - k(r_0 + \delta_{pre} - r) + b\dot{r} = 0 \tag{B.23}
$$

or

$$
\ddot{r} = r\dot{\gamma}^2 - g\cos\gamma + \frac{k(r_0 + \delta_{pre} - r)}{m} - \frac{b\dot{r}}{m}. \tag{B.24}
$$

For $q_2 = \gamma$,

$$
\begin{aligned}
&\frac{\partial L}{\partial \dot{q}_2} = mr^2\dot{\gamma}, \\
&\frac{d}{dt}\left(\frac{\partial L}{\partial \dot{q}_2}\right) = mr^2\ddot{\gamma} + 2mr\dot{r}\dot{\gamma}, \\
&\frac{\partial L}{\partial q_2} = mgr\sin\gamma, \\
&\frac{\partial D}{\partial \dot{q}_2} = 0, \\
&F_2 = \tau^{Hip}.
\end{aligned} \tag{B.25}
$$

The Lagrange equation becomes

$$
mr^2\ddot{\gamma} + 2mr\dot{r}\dot{\gamma} - mgr\sin\gamma = \tau^{Hip} \tag{B.26}
$$

or

$$\ddot{\gamma} = -\frac{2\dot{r}\dot{\gamma}}{r} + \frac{g \sin \gamma}{r} + \frac{\tau^{Hip}}{mr^2}. \tag{B.27}$$

As in Eqs. (B.24) and (B.27), thus, two equations of motion for the stance phase model are obtained:

$$\begin{aligned} \ddot{r} &= r\dot{\gamma}^2 - g \cos \gamma + \frac{k(r_0 + \delta_{pre} - r)}{m} - \frac{b\dot{r}}{m}, \\ \ddot{\gamma} &= -\frac{2\dot{r}\dot{\gamma}}{r} + \frac{g \sin \gamma}{r} + \frac{\tau^{Hip}}{mr^2}. \end{aligned} \tag{B.28}$$

Appendix C. Poincaré map

As shown in Figure C.1(a), the Poincaré map can be defined as a vector function, P, mapping the state vector of the n-th cycle $\underline{x}_n$ on one cross-section (or *Poincaré section*) Σ of a state space to the state vector of the (n+1)-st cycle $\underline{x}_{n+1}$ on the same cross-section, through a periodic trajectory $\underline{x}(t)$ of a dynamical system:

$$\underline{x}_{n+1} = P(\underline{x}_n)\,. \tag{C.1}$$

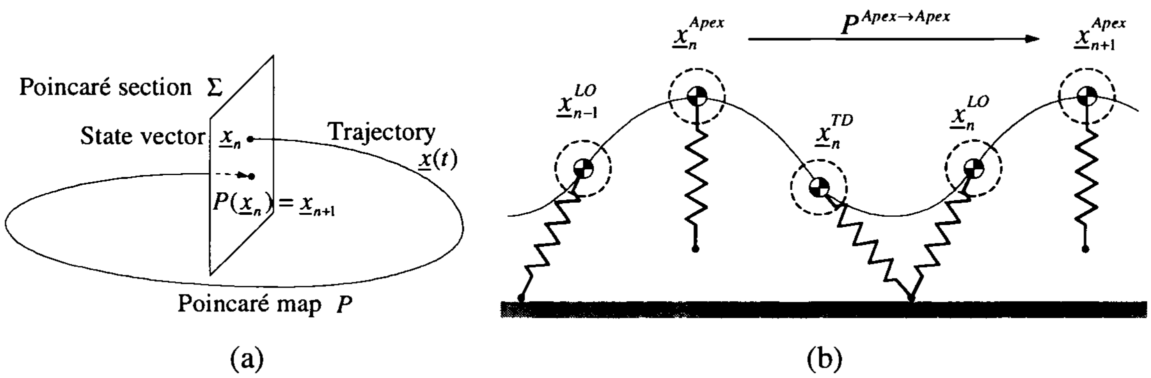

Figure C.1 (a) Poincaré map and (b) discrete state vectors of the hopping cycle

Studied in the thesis is the plot of the sequential apex states $\underline{x}_n^{Apex} = (z_n^{Apex}, \dot{x}_n^{Apex})$ generated by consecutive Poincaré map operations from one apex to the next $P^{Apex\rightarrow Apex}$. Here, z_n is the vertical position and $\dot{x}_n$ is the forward speed in the n-th hopping cycle. The Poincaré map operation $P^{Apex\rightarrow Apex}$ is done by numerically integrating the equations of motion from apex to touchdown, from touchdown to lift-off, and from lift-off to apex. Each piecewise part is a respective Poincaré map as shown in Figure C.2:

$$\begin{aligned} \underline{x}_{n+1}^{Apex} &= P^{Apex\rightarrow Apex}(\underline{x}_n^{Apex}) \\ &= P^{LO\rightarrow Apex} \circ P^{TD\rightarrow LO} \circ P^{Apex\rightarrow TD}(\underline{x}_n^{Apex})\,. \end{aligned} \tag{C.2}$$

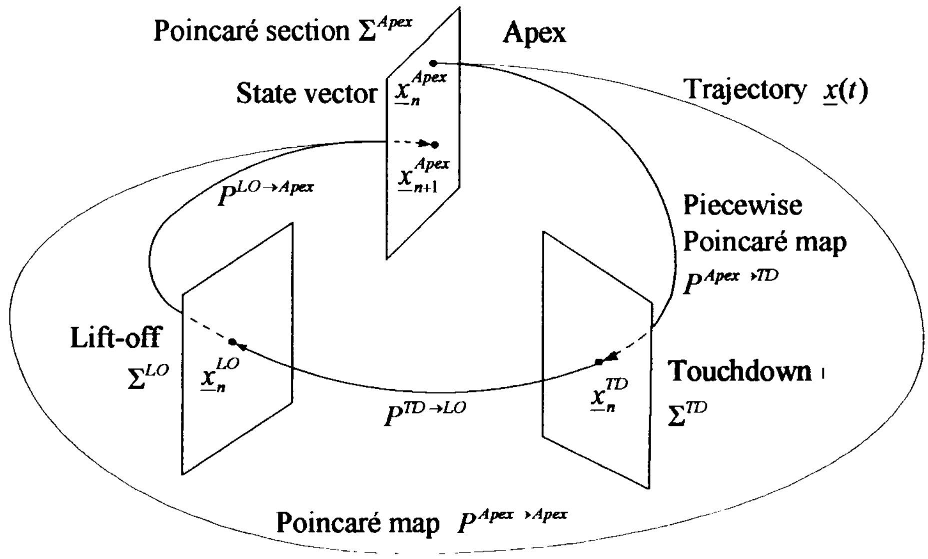

Figure C.2 Apex-to-apex Poincaré map and piecewise Poincaré maps

Plane $\Sigma = \{(z, \dot{x}) \in \mathbb{R}^2\}$ at apex is selected as the Poincaré section of the hopping cycle. Considering that the COM dynamics has the state space $\{(x, z, \dot{x}, \dot{z})\}$ and the horizontal position x is not of interest, hyperplane $\{(z, \dot{x}, \dot{z}) \in \mathbb{R}^3\}$ seems to be most appropriate. However, the dimension can be reduced by one since the vertical speed at apex is always zero, by definition:

$$\dot{z}_n^{Apex} = 0, \quad \forall n \in \mathbb{N}. \tag{C.3}$$

This reduction is consistent with an energy point of view. The total energy of the COM in flight is

$$E_{total} = mgz + \frac{1}{2}m(\dot{x}^2 + \dot{z}^2), \tag{C.4}$$

which includes $(z, \dot{x}, \dot{z}) \in \mathbb{R}^3$, but only $(z, \dot{x}) \in \mathbb{R}^2$ need be considered at apex since $\dot{z}_n^{Apex} = 0$. Thus, the convergence of the hopping motion and energy distribution can be simultaneously evaluated using the selected Poincaré section $\Sigma = \{(z, \dot{x}) \in \mathbb{R}^2\}$ and discrete state vector $\underline{x}_n^{Apex} = (z_n^{Apex}, \dot{x}_n^{Apex})$.

Appendix D. Phase Curve Time Evolution of Height

Simulation result

Figure D.1 shows phase-curve time evolution of height, i.e. a trajectory of vertical speed versus vertical position evolving with time. The data obtained from the simulation in Chapter 3 are used. The initial condition (IC) is at apex and is a forward speed of $-0.60 m/s$, a vertical position of 0.260 *m*, and a vertical speed of 0 *m/s*. It results in a helix-like spiral, and the circular shape is created by the 2D cross-section of the vertical position and vertical speed states. The time evolution of the cross-section appears as the progress in the direction of spiral axis. The convergence with respect to time is seen because the radius of the spiral becomes constant as the time progresses. One turn of the spiral designates one hopping cycle as in the case of the 2D phase plot, Figure 3.6. Therefore, the pitch length of the spiral indicates the period of one hopping cycle.

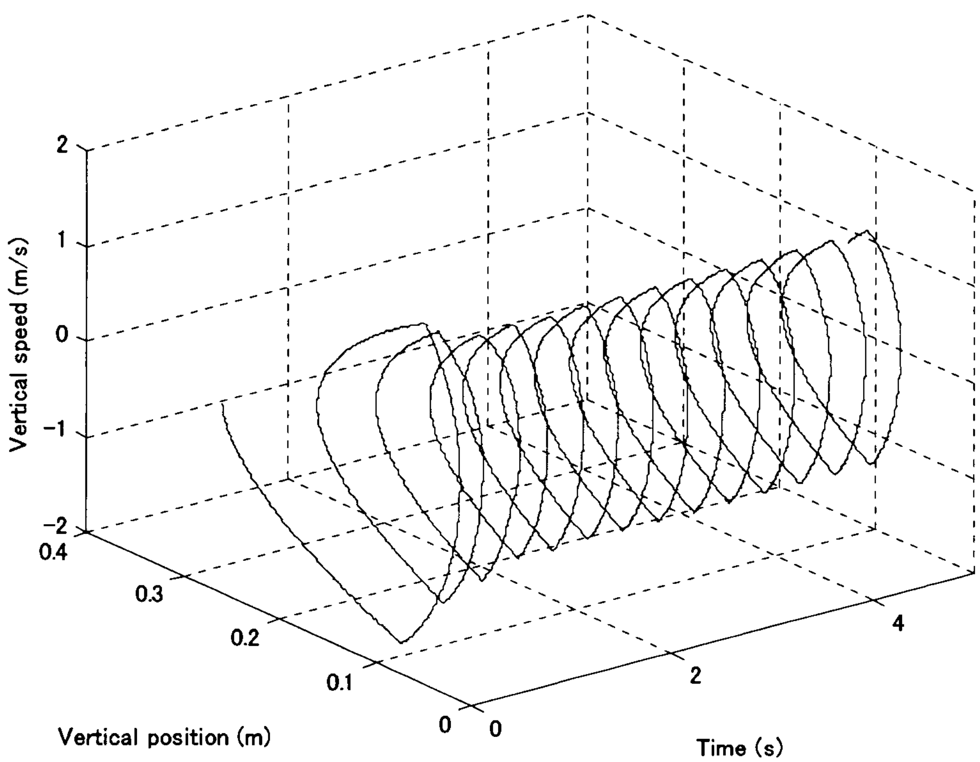

Figure D.1 Phase-curve time evolution of height in the simulation

Experimental result

Figure D.2 shows phase-curve time evolution of height for the SLIP robot. The data obtained from the experiment in Chapter 5 are used. The initial condition (IC) is at apex and is a forward speed of –0.58 *m/s*, a vertical position of 0.263 *m*, and a vertical speed of 0 *m/s*. This figure shows a close resemblance to Figure D.1 provided by the simulation. The convergence with respect to time is seen here, as well.

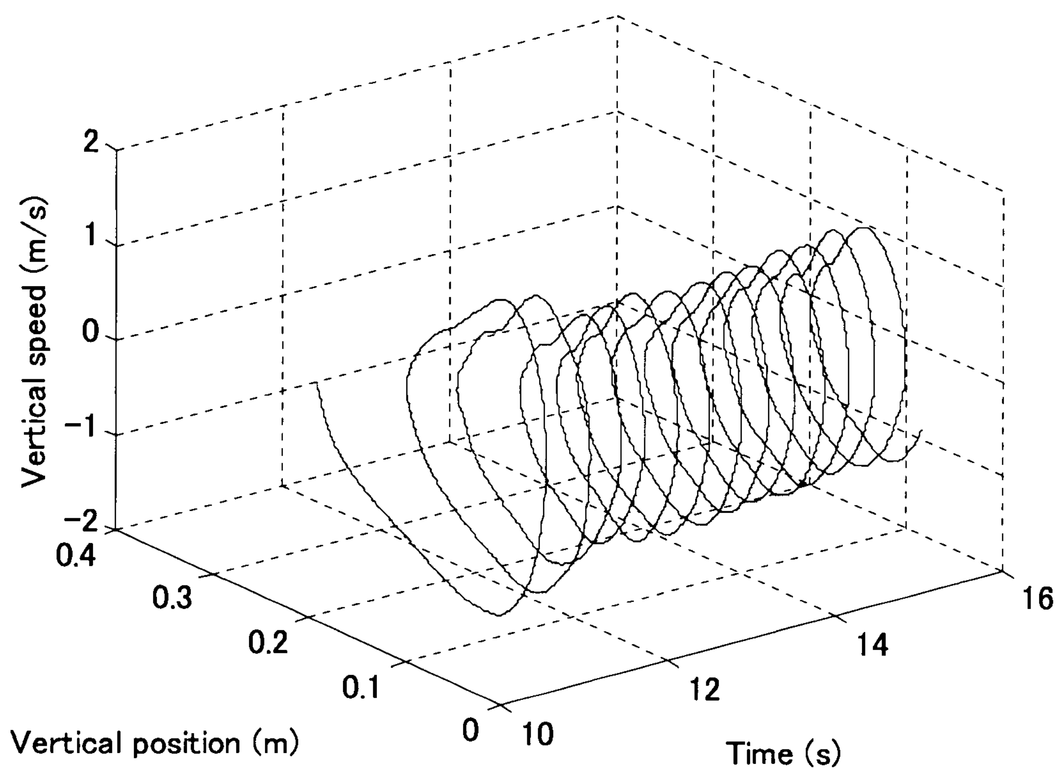

Figure D.2 Phase-curve time evolution of height in the experiment